2020

Development and Application of Novel Sound Absorbers

Weiyun Liu
University of Kentucky, weiyunuk@gmail.com
Digital Object Identifier: https://doi.org/10.13023/etd.2020.456

STUDENT AGREEMENT:

I represent that my thesis or dissertation and abstract are my original work. Proper attribution has been given to all outside sources. I understand that I am solely responsible for obtaining any needed copyright permissions. I have obtained needed written permission statement(s) from the owner(s) of each third-party copyrighted matter to be included in my work, allowing electronic distribution (if such use is not permitted by the fair use doctrine) which will be submitted to UKnowledge as Additional File.

I hereby grant to The University of Kentucky and its agents the irrevocable, non-exclusive, and royalty-free license to archive and make accessible my work in whole or in part in all forms of media, now or hereafter known. I agree that the document mentioned above may be made available immediately for worldwide access unless an embargo applies.

I retain all other ownership rights to the copyright of my work. I also retain the right to use in future works (such as articles or books) all or part of my work. I understand that I am free to register the copyright to my work.

REVIEW, APPROVAL AND ACCEPTANCE

The document mentioned above has been reviewed and accepted by the student's advisor, on behalf of the advisory committee, and by the Director of Graduate Studies (DGS), on behalf of the program; we verify that this is the final, approved version of the student's thesis including all changes required by the advisory committee. The undersigned agree to abide by the statements above.

Weiyun Liu, Student

Dr. David W. Herrin, Major Professor

Dr. Alexandre Martin, Director of Graduate Studies

DEVELOPMENT AND APPLICATION OF NOVEL SOUND ABSORBERS

DISSERTATION

A dissertation submitted in partial fulfillment of the
requirements for the degree of Doctor of Philosophy in the
College of Engineering
at the University of Kentucky

By

Weiyun Liu

Lexington, Kentucky

Director: Dr. David W. Herrin, Professor of Mechanical Engineering

Lexington, Kentucky

ABSTRACT OF DISSERTATION

DEVELOPMENT AND APPLICATION OF NOVEL SOUND ABSORBERS

The sound absorbers in most common use today are porous materials like fibers and foams. This work examines three alternatives to porous absorbers: microperforated panels, acoustic fabrics, and additively manufactured absorbers. The research is a combination of design, measurement and characterization of their properties, and analysis.

Microperforated panels are thin metallic or plastic panels with sub-millimeter size holes or perforations. Sound absorption can be tuned by adjusting the spacing between the panel and a cavity behind the panel. Several different configurations were considered where the geometry behind the panel was divided up into channels of varying length and cross-sectional area. Results showed that the sound absorption effectiveness could be improved at low frequencies and that the absorber was more effective over a broader range of frequencies. This was demonstrated using both impedance tube measurements and diffuse field sound absorption measurements in a small reverberant room.

Sound absorptive fabrics are similar to microperforated panel absorbers and function using the same principle. Acoustic resistance is high through the fabric due to small holes or the tight weave. If the particle velocity is high in the fabric, the fabric will effectively attenuate sound. The sound absorption is easily tuned by adjusting the distance between the fabric and a hard backing. It is demonstrated that the transfer impedance can be simulated using theory similar to that typically used for characterizing microperforated panel absorbers.

Recently, there has been a great interest in using additive manufacturing to develop sound absorbers. The design space was partially explored by designing absorbers using long perforations, lightweight panels, and Helmholtz resonators with long necks. The sound absorbers are shown to be very effective at low frequencies where conventional sound absorbers like fibers and foams are ineffective.

KEYWORDS: sound absorbers, microperforated panels, fabrics, 3D printed sound absorbers, sound absorption, transmission loss

Weiyun Liu
Student's Signature

November 03, 2020
Date

DEVELOPMENT AND APPLICATION OF NOVEL SOUND ABSORBERS

By

Weiyun Liu

Dr. David W. Herrin
Director of Dissertation

Dr. Alexandre Martin
Director of Graduate Studies

November 03, 2020
Date

To my family

ACKNOWLEDGEMENTS

I would like to foremost express my deepest gratitude to my advisor Prof. David W. Herrin for your invaluable guidance and continued support. I would also like to thank Professor John Baker, Professor Tim Wu and Professor Qiang Ye and Professor L E. Delong for being my committee members and providing valuable suggestions.

I would also like to thank all my former and current colleagues from the Vibration and Acoustics lab. Thank you all for your support and friendship. I will miss the days that we perform tests together in our lab and our happy lunch time at Fresh Food and Champion Kitchen.

Finally, and not the least, I would like to thank my parents, sister and husband for their support and love.

TABLE OF CONTENTS

LIST OF TABLES

LIST OF FIGURES

Chapter 1 INTRODUCTION

1.1 Background

Noise is defined as unwanted sound. Most of the unwanted noise that can be controlled is a result of machinery including but not limited to engines, transmissions, pumps, blowers and fans, and manufacturing equipment of various types. Sometimes noise is so intrusive that it must be reduced. It may lead to permanent hearing damage and has been associated with serious health issues including high blood pressure and mental health issues (Lercher, 1996, Stansfeld and Matheson, 2003). Not surprisingly, the Occupational Safety and Health Administration (OSHA) prescribes limits on noise exposure in the workplace and requires employers to implement hearing conservation programs when levels exceed 85 dB averaged over 8 hours (OSHA, 2020).

Noise must also be reduced for commercial reasons. Quiet machines, automobiles, climate control equipment, and appliances are more desirable than their noisier counterparts. In most cases, there is a trade-off between reducing noise and improving energy efficiency because machinery that is more powerful is often, though not always, noisier. In recent years, there has been an emphasis in reducing weight in automobiles and other equipment to reduce cost and increase energy efficiency. However, this necessarily results in higher vibration levels and correspondingly higher sound pressure levels.

Noise control is likely most easily understood by considering the source, path, and receiver separately. Sources include engines, compressors, and other prime movers that produce noise due to the high internal forces. Receivers

correspond to people or sensors in standardized tests (i.e., pass-by or sound power). Paths refer to structureborne or airborne transmission from source to receiver locations.

Noise can be controlled by active and passive means. Active systems use either acoustic or mechanical actuators to cancel out unwanted noise. Though an ideal approach at the receiver where it is used in headphones and some personal protective equipment, active approaches are not as effective in lowering source levels or adding path attenuation. Moreover, active treatments are generally more expensive to implement.

Passive systems use either reactive or resistive mechanisms to attenuate noise and are less expensive which explains their prevalence. Passive approaches are commonly used to attenuate noise along transmission paths from the source to receiver. They include adding barriers and enclosures to reflect sound back towards the source and away from a receiver. Other reactive approaches include adding resonators or mufflers to cancel or reflect sound back towards the source. Sound along transmission paths can also be reduced using resistive mechanisms. Damping can be added to structures using a number of approaches. Airborne paths are normally treated by adding sound absorptive linings or perforated panels to dissipate energy via viscous friction. Air moves against the porous material skeleton or inside of small holes, and energy is converted into heat.

One of the most common means of reducing noise is to enclose the source, receiver, or both. For example, automobiles incorporate both an engine enclosure and a passenger compartment, and both are commonly treated with sound

absorbing materials. Similar strategies are used for heavy construction and agricultural equipment. In building climate control systems, ventilation ducts and plenum are commonly treated with glass fiber. In each of the aforementioned applications, cost drives the treatment decisions, and fiber and foams are preferred for that reason.

However, fibers and foams degrade over time and are not appropriate in severe environments. Though fibers have a very good fire rating, they may become soaked with oil and become a potential hazard. For manufacturing and food processing equipment, it is highly desirable to clean and disinfect equipment regularly. Fibers and foams are inappropriate in those situations.

Fibers and foams also have performance limitations especially at low frequencies. Sound energy is attenuated by viscous friction, and this can only be accomplished if the particle velocity in the material is high. Particle velocity is minimal near a hard surface and so fiber or foam needs to be as a rule of thumb 1/10th the thickness of an acoustic wavelength which is equal to the speed of sound (343 m/s in air at room temperature) divided by frequency in Hz. Porous absorbers generally need to be in excess of 5 cm thick to effectively attenuate noise below 500 Hz.

For these reasons, researchers are interested in developing new sound absorptive materials that do not have the limitations of foams and fibers. The research in this thesis looks at three potential alternatives to foams and fibers. The sound absorbers investigated are 1) microperforated panel absorbers, 2) acoustic fabrics, and 3) additively manufactured sound absorbers.

Microperforated panels (MPP) are thin panels with sub-millimeter size holes and low perforation rates (normally less than 8%). They dissipate sound due to the viscous friction in the sub-millimeter size perforations. They are normally spaced from a hard surface and are most effective when the acoustic particle velocity is high in the perforations. They are sometimes likened to the more familiar Helmholtz resonators which utilize a small neck connected to a backing volume. This analogy is true in the sense that they are most effective at the resonances of the combined perforated plate and backing cavity. However, MPP are broadband absorbers due to the high viscous friction whereas Helmholtz resonators are narrow band. The cavity depth controls the frequency bands of high absorption. It is best if the panel can be positioned approximately one-fourth wavelength from a wall.

It is more difficult to integrate MPP into a design than porous absorbers because they are best considered as a system comprised of the panel and backing. In practice, MPP are spaced away from a hard wall. Sometimes honeycomb is placed behind the MPP so that the absorber functions more like a locally reacting absorber. In this research, several new backing cavity designs are modeled and tested. The sound absorption is then measured using a standard impedance tube test for normal incident sound. A larger absorber of each type was then fabricated and tested in a small reverberation room to determine the effectiveness for random incident noise.

Acoustic fabrics, the second novel sound absorber considered in this thesis, are gaining popularity due to their deployability, durability, aesthetically pleasing appearance, easy maintenance and good sound absorptive performance. Acoustic

fabrics dissipate sound as a result of their high acoustic resistance. Similar to MPP absorbers, they are effective when the particle velocity is high in the perforations. They are currently being used for home furnishings and vehicle interior decorations (Dias et al., 2006, Dias et al., 2007a, Dias et al., 2007b).

While the extant research on MPP absorbers is extensive, acoustic fabrics are a newer development and there is less literature. Most of the work to this juncture has focused on characterizing their sound absorptive performance (Pieren, 2012, 2015). In this thesis, the sound absorptive performance is investigated using approaches that have been used to characterize MPP absorbers. It is demonstrated that effective MPP absorber parameters can be used to characterize the fabric acoustic properties. However, it is shown that the characterization is dependent on the mass of the fabric whereas the mass of MPP absorbers can be neglected. The effective parameters are determined from measured data by producing a best fit prediction to the data using a least squares curve fit and may be used to predict the performance of layered fabrics as well as the transmission loss through the fabrics. The fabrics are also applied inside a small enclosure and their effectiveness is assessed.

An ancillary study is included which examines the sensitivity of the sound absorption to the parameters hole diameter, perforation rate, thickness, and mass using the equation for characterizing MPP absorbers first proposed by Maa (1975). The goal of this study is to demonstrate that the Maa's equation is mostly useful for designing and characterizing MPP absorbers when the geometric parameters hole size and perforation rate is in a certain range. For parameter levels outside

of this range, Maa's equation should be used with some caution when designing absorbers. These results make the case for instead measuring the sound absorber performance and determining effective parameters.

The final class of sound absorbers investigated are additively manufactured (i.e. 3D printed). The use of 3D printing to develop sound absorbers is a recent development. At this juncture, studies are exploratory because current technology cannot be used to develop commercially viable sound absorbers due to the cost. However, it is anticipated that these absorbers will be workable as 3D printing technology improves and gets cheaper. In recent developments, several acoustic metamaterials have been developed using 3D printing (Liu, 2017, Lepak et al., 2018, Leblanc and Lavie, 2017, Jonza et al., 2017). These materials have properties that are not found in "natural" materials including fibers and foams. The metamaterials are normally reactive and include sets of resonators tuned to the same frequency or to different frequencies to produce broadband sound absorption.

1.2 Objectives of Research

The objectives of the research detailed in this thesis are to:

(1) Design, fabricate and test microperforated panel (MPP) absorbers with designed backings to improve low frequency and broadband performance. Both normal incidence and diffuse sound field absorption are considered.

(2) Improve the characterization of acoustic fabrics by determining effective parameters using a least squares curve fit while also including mass.

(3) Demonstrate the effectiveness of acoustic fabrics in an enclosure.

(4) Perform an error analysis on the equation commonly used to characterize MPP absorbers and acoustic fabrics.

(5) Apply additive manufacturing to develop combination resistive and reactive sound absorbers.

1.3 Outline of Dissertation

The structure of this dissertation is as follows.

Chapter 1 introduces the importance of developing novel sound absorbers.

Chapter 2 reviews the theory that will be used in this research including discussions on transfer impedance, sound absorption, and transmission loss.

The focus of Chapter 3 is on microperforated panel absorbers, and designing different backing configurations to improve sound absorptive performance. Plane wave and acoustic finite element simulation was performed for each case and compared with normal incidence sound absorption measurement. In addition, the diffuse field sound absorption was measured in a small reverberation room.

Chapter 4 details research on acoustic fabrics. Specifically, the approach for characterizing their material properties is improved. This is followed by investigating their transmission loss and by demonstrating their performance in a small enclosure.

Chapter 5 details exploratory work on the development of sound absorbers using additive manufacturing. Resistive, reactive, and combination resistive-reactive sound absorbers are developed. Each absorber is simulated, fabricated, and then normal incidence sound absorption is measured.

Chapter 6 summarizes the research detailed in this thesis and provides recommendations for future work.

Chapter 2 BACKGROUND THEORY

This chapter will review some basics about resistive and reactive sound absorbers. Resistive sound absorbers are normally porous and are accordingly also referred to as porous absorbers. Reactive sound absorbers contain resonator elements. Some reactive sound absorbers are combinations of Helmholtz resonators and quarter wave tubes. Others include a thin panel or membrane and depend entirely or partly on structural resonances. More recently, designers have begun to develop sound absorbers which are a combination of resistive and reactive features. The most used of these combination sound absorbers is likely microperforated panel sound absorbers.

The second part of this chapter details standard measurements to determine both normal incidence impedance and sound absorption, diffuse field impedance, transmission loss, and transfer impedance. These properties and metrics are used to assess the effectiveness of the different sound absorptive treatments.

2.1 Dissipative Sound Absorbers

When sound waves impact a solid like a panel of glass, most of the sound is reflected though a small amount of energy is absorbed due to damping. Some energy is also transmitted through the panel. On the other hand, porous absorbers consist of a solid matrix and voids. Some sound is reflected from the absorber, but most of the energy will propagate through the absorber so long as the impedance of the absorber is on the order of air. As sound waves propagate through the absorber, sound energy is converted to heat via one of two mechanisms. At lower

frequencies, vibration of the material skeleton or damping is the primary attenuation mechanism. At middle to higher frequencies, viscous friction is dominant and is the more important mechanism since damping is minimal.

Scanning electron microscope images of four sound absorbers are shown in Figure 2.1 (Alba et al., 2015, Cox and D'Antonio, 2017). Porous absorbers are constructed in several different ways from many different base materials. Glass fiber and rock wool are commonly used fiber materials. Fibers (Figure 2.1c) are often used in heating, ventilation and air conditioning systems. More recently, natural materials from plants have been used to create fiber sound absorbers (Mohanty and Fatima, 2015, Zulkifli et al., 2010, Sezgin and Haluk, 2009).

Another common porous absorber type is foams. Foams (Figure 2.1a) are manufactured using large ovens. The process to manufacture foams is often compared to baking. This process can be tuned to adjust the makeup of the material. For acoustic purposes, open cell reticulated foams are preferred and perform much better acoustically than closed cell foams which are preferred when thermal purpose is more important.

Granular materials such as powders, sand (Figure 2.1 b), or ground up rubber are sometimes used though normally not in commercial applications. Activated carbon is especially advantageous as a sound absorber because of the voids between grains as well as micro-voids within the grains (Cox and D'Antonio, 2017). Figure 2.1d shows a double porosity material akin to activated carbon.

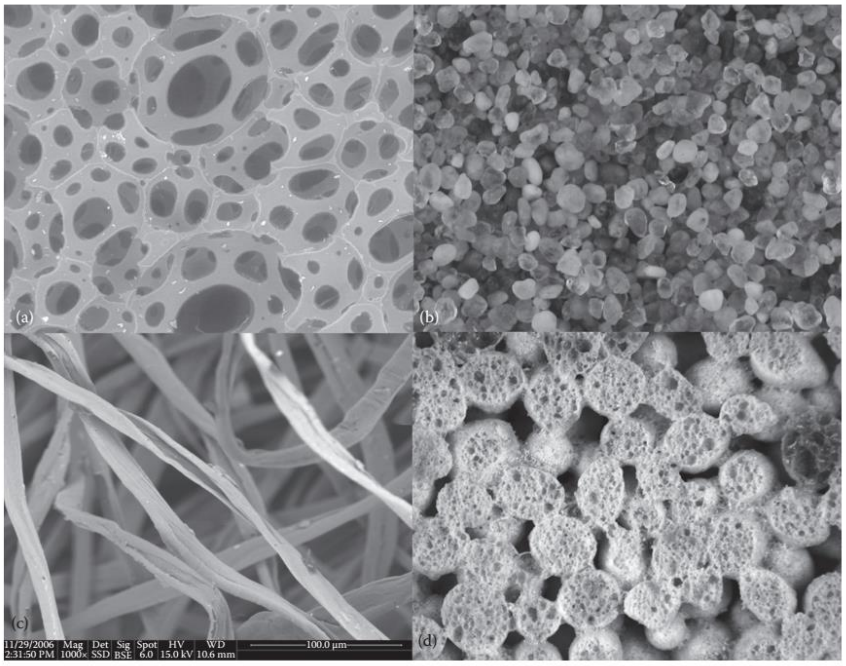

Figure 2.1 Different types of porous absorbers under scanning electron microscope. (a) white foam, (b) granular material, (c) cotton fibers, and (d) double porosity material (Cox and D'Antonio, 2017).

2.2 Reactive Sound Absorbers

Reactive sound absorbers are created from simple resonators. For example, a membrane or panel can be placed over an air cavity as shown in Figure 2.2. The membrane functions as a mass and the air in the backing cavity as a spring where the stiffness is related to the bulk modulus of air and the panel supporting structure. The bulk modulus of air can be expressed as ρc^2 where ρ is the mass density and c is the speed of sound of the fluid. Depending on the absorber, the acoustic or structural stiffness may be more dominant. Panel absorbers like that in Figure 2.2 are frequently used in reverberation rooms or studios and are sometime referred to as bass traps.

Assuming that the stiffness is only due to the air cavity, the resonance frequency (f_r) is expressed as

$$f_r = \frac{1}{2\pi}\sqrt{\frac{\rho c^2}{m_s d}} \tag{2.1}$$

where m_s is the surface mass density of the panel (mass per unit area) and d is the spacing from the wall (Cox and D'Antonio, 2017). The supporting structure nearly always plays a role in the stiffness, so the resonance frequencies are normally identified and tuned experimentally.

A Helmholtz resonator is analogous to the membrane case. This is achieved in practice by placing a perforated panel in front of an air cavity. The air in the perforations functions as the mass, and the stiffness arises from the encapsulated air volume behind the perforated panel. If the panel is considered as a collection of cells each containing one hole, the resonance frequency can be expressed as

$$f_r = \frac{c}{2\pi}\sqrt{\frac{S}{t'V}} \tag{2.2}$$

where is t' is the thickness of the perforated sheets plus end corrections, S is the area of a hole, and V is the air volume behind a particular cell (Cox and D'Antonio, 2017). Alternatively, the resonant frequency can be expressed as

$$f_r = \frac{c}{2\pi}\sqrt{\frac{\varepsilon}{t'd}} \tag{2.3}$$

where ε is the fraction of open area and d is the cavity depth. The thickness of the panel including end corrections can be expressed as

$$t' = t + 2\delta a + \sqrt{\frac{8\nu}{\omega}\left(1 + \frac{t}{2a}\right)} \tag{2.4}$$

where t is the panel thickness, δ is an end correction factor which is commonly approximated as 0.85, a is the radius of a hole, ω is the angular frequency, and ν is the kinematic viscosity of air which can be expressed as $15 \times 10^{-6}\ \mathrm{m}^2/s$. Cox and D'Antonio (2017) included a table of adjustments to the above equation that are dependent on the shape and arrangement of the perforations.

The sound absorptive band can be broadened by adding fiber behind the membrane or the panel as shown in Figure 2.2 (a). Figure 2.2 (b) shows the sound absorption for a fiber alone compared to that of fiber fronted by a perforated cover. Note the beneficial sound absorption at lower frequencies that could not be achieved with a porous absorber alone. A mylar or foil cover is sometimes used to front a porous absorber and it produces a similar effect.

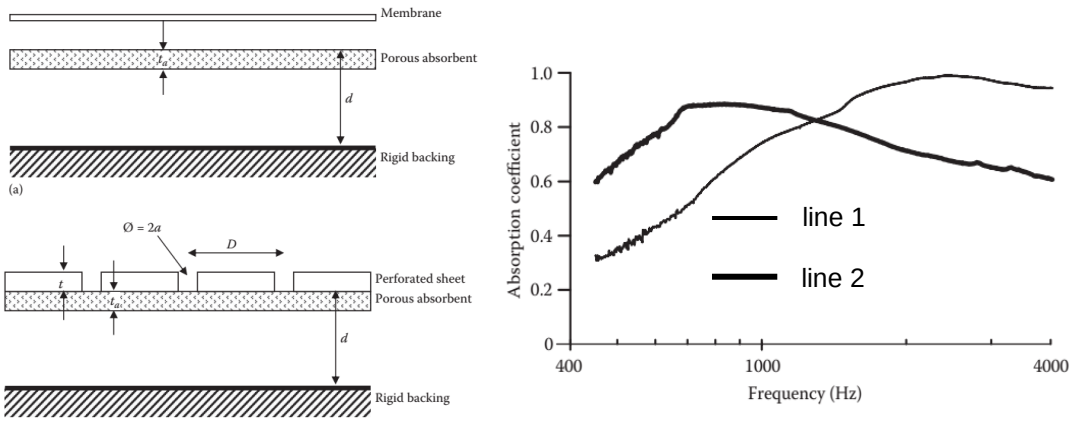

(a) (b)

Figure 2.2 (a) Constructions for membrane and Helmholtz absorbers supplemented with porous layers, (b) Normal incident sound absorption where line 1 indicates porous absorber and line 2 indicates Helmholtz resonator with porous absorber. (Cox and D'Antonio, 2017).

Microperforated panel absorbers (Maa, 1975) are a combination resistive and reactive sound absorber that perform similarly to the Helmholtz resonators with porous sound absorption added behind the panel. They may be thought of as a Helmholtz resonator with very small perforations. The small perforations will lead to high viscous losses and accordingly effective sound absorption if the particle velocity is high in the perforations. They are a tuned absorber with broadband absorption because of the high resistance. The advantages are that a porous absorber is avoided, the construction is durable, and the absorber is tunable.

2.3 Metrics for Sound Absorption

Several different metrics are used to describe sound absorbers. In analytical and numerical models, the surface impedance, defined as the ratio of

sound pressure to particle velocity, is frequently used as a boundary condition. The surface impedance is expressed as

$$Z_s = \frac{p}{u} \tag{2.5}$$

where p is the complex sound pressure and u is the particle velocity at the surface. Both sound pressure and particle velocity are complex quantities, so the surface impedance is as well. The real part of the impedance is called the resistance and the imaginary part the reactance. The surface impedance depends on the angle of incidence of the sound wave. However, the sound wave will diffract towards the normal direction as it enters the sound absorber. If this assumption is used, the sound absorber is considered to be locally reacting. Locally reacting means that the particle velocity at a location on the absorber surface is only a function of the sound pressure at that particular location.

When assessing sound absorbers, the metric most commonly used is the sound absorption. The sound absorption is the ratio of the transmitted or absorbed intensity to the incident intensity. Hence, it can be expressed as

$$\alpha = \frac{I_{tr}}{I_{inc}} \tag{2.6}$$

where I_{tr} is the transmitted and I_{inc} is the incident sound intensity. The transmitted intensity is assumed to be dissipated within the absorber. Sound absorption depends on the angle of incidence. Normal incidence is when the direction of wave propagation is perpendicular to the sound absorber. The sound absorption should always be between 0 and 1 where a sound absorption of 0

indicates that the wave is reflected from the surface and no energy is lost and a sound absorption of 1 indicates that the sound wave is completely absorbed. The sound absorption coefficient is plotted versus frequency for a fiber in Figure 2.3 (Horoshenkov, et al., 2007, Cox and D'Antonio, 2017). This curve is typical of many porous absorbers. The sound absorption increases with frequency before plateauing. The particular material shown in the figure was used for a round robin test and 95% confidence limits are shown. The nature of this test will be described later in the chapter.

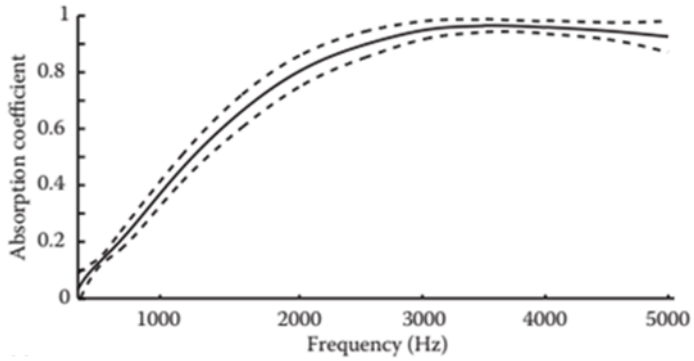

Figure 2.3 Comparison of impedance tube measurements of the absorption coefficient for fiber glass in up to seven laboratories. The mean absorption coefficient is shown, along with dotted lines indicating the 95% confidence limit in any one laboratory measurement. (Cox and D'Antonio, 2017, adapted from Horoshenkov, et al., 2007).

Alternatively, the diffuse field sound absorption is also commonly measured. This assumes that waves are impacting the sound absorber at all possible directions. Measurement is performed in a reverberation room where it is assumed that sound waves will be incident at all possible angles though this is not necessarily the case at low frequencies. The spatially averaged sound pressure

level is measured with a standard sample size of sound absorbing material positioned at the center of the floor of a reverberation room. The measurement procedure is described in more detail later.

The diffuse field sound absorption is plotted versus frequency for a 100 mm thick mineral wool in Figure 2.4 (Cox and D'Antonio, 2017, adapted from Jeong and Chang, 2015). The 95% confidence limits for a round robin test are also indicated. Observe that the diffuse field sound absorption may exceed 1. This is often the case at low frequencies where sound waves diffract or bend towards a sound absorbing sample. This diffraction is not accounted for in room acoustics theory. In addition, measurement variation in the round robin test is much greater than for normal incidence absorption. The reverberation room has a considerable effect on the measurement. Though the measurement is very repeatable in the same room, it is not as repeatable from one room to another.

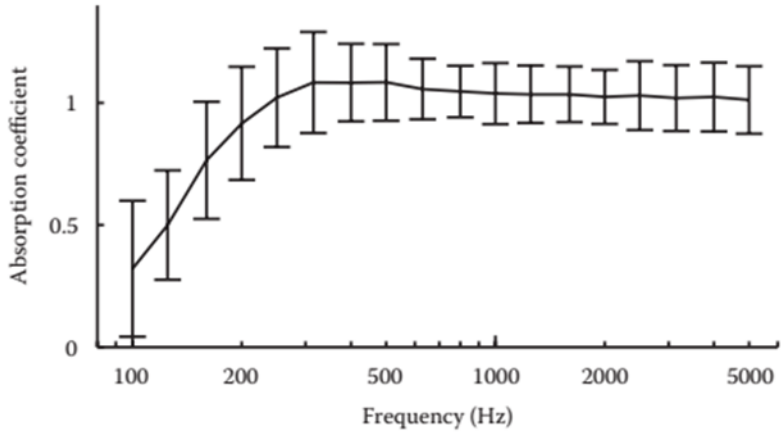

Figure 2.4 Comparison of absorption coefficients measured in 13 different laboratories for a 100 mm mineral wool absorber in a wooden casing covered with nonwoven fleece. (Cox and D'Antonio, 2017, adapted from Jeong and Chang, 2015).

2.4 Porous Sound Absorber Properties

Over a half century ago, Mechel et al. (1965) measured both the flow and acoustic resistance of thin samples. They discovered that the acoustic resistance could be approximated by the flow resistance for thin samples at low frequencies. This discovery has led to researchers developing empirical equations which relate the acoustic properties to the flow resistance. The flow resistance can be measured by forcing flow through a porous absorber and measuring both the flow rate and pressure drop. The flow resistance can be expressed as

$$R_f = \frac{u_f}{\Delta p} \tag{2.7}$$

and empirical equations can be written as a function of the flow resistivity (σ_f) which is just the flow resistance (R_f) per unit thickness.

Using Mechel et al. as a starting point, other researchers have developed empirical equations for different material classes relating the acoustic properties to the flow resistivity. Mechel and Ver (1992) demonstrated that sound absorption curves for different densities of the same material correlate well with each other when plotted versus X where

$$X = \frac{\rho f}{\sigma_f} \tag{2.8}$$

where ρ is the fluid density, f is the frequency in Hz, and σ_f is the flow resistivity. If the flow resistivity is known, both the characteristic impedance Z' and complex

wavenumber k' of the material can be determined using empirical equations. The characteristic impedance is defined as

$$Z' = \rho' c' \tag{2.9}$$

where ρ' and c' are the complex density and complex speed of sound of the sound absorber respectively. The complex wavenumber is defined as

$$k' = \frac{\omega}{c'} \tag{2.10}$$

where ω is the angular frequency in rad/s.

The empirical equation for the complex characteristic impedance and wavenumber can be written as

$$Z_m = \rho c(1 + C_1 X^{-C_2} - jC_3 X^{-C_4}) \tag{2.11}$$

and

$$k_m = \frac{\omega}{c}(1 + C_5 X^{-C_6} - jC_7 X^{-C_8}) \tag{2.12}$$

where C_1 through C_8 are constants determined experimentally for different material types. These constants are provided in Table 2.1. The material models are indicated on the left column of the table.

Table 2.1 Parameters for Empirical Model (Bies et al., 2017)

Material Type Reference	C_1	C_2	C_3	C_4	C_5	C_6	C_7	C_8
Rockwool/fiberglass Delaney and Bazley (1970)	0.0571	0.754	0.087	0.732	0.0978	0.700	0.189	0.595
Rockwool/fiberglass Miki (1989)	0.070	0.632	0.107	0.632	0.109	0.618	0.160	0.618
Polyester Garai and Pompoli (2005)	0.078	0.623	0.074	0.660	0.159	0.571	0.121	0.530
Polyurethane foam of low flow resistivity Dunn and Davern (1986)	0.114	0.369	0.0985	0.758	0.168	0.715	0.136	0.491
Porous plastic foams of medium flow resistivity Wu (1988)	0.209	0.548	0.105	0.607	0.188	0.554	0.163	0.592
Fiber Mechel (2002) (X <0.025)	0.081	0.699	0.191	0.556	0.136	0.641	0.322	0.502
(X >0.025)	0.0563	0.725	0.127	0.655	0.103	0.716	0.179	0.663

For a single layer absorber, the surface impedance can be expressed as

$$Z_s = -jZ' \cot(k'L) \tag{2.13}$$

where L is the thickness of the sound absorbing layer. The reflection coefficient (R) is defined as

$$R = \frac{Z_s - \rho c}{Z_s - \rho c} \tag{2.14}$$

from which the sound absorption can be expressed as

$$\alpha = 1 - |R|^2 \tag{2.15}$$

For modeling purposes, a transfer matrix relating the sound pressure and particle velocity on one surface of a sound absorber to that on another can be expressed as

$$\begin{Bmatrix} p_1 \\ Su_1 \end{Bmatrix} = \begin{bmatrix} \cos(k'L) & \frac{jZ'}{S}\sin(k'L) \\ \frac{jS}{Z'}\sin(k'L) & \frac{1}{S}\cos(k'L) \end{bmatrix} \begin{Bmatrix} p_2 \\ Su_2 \end{Bmatrix} \tag{2.16}$$

where L is the length and S is the cross-sectional area of the sample. This can be used to model layered sound absorbers by multiplying the transfer matrices for each layer together. Hence, the total transfer matrix $[T_{total}]$ for an N layer sample can be expressed as

$$[T_{total}] = [T_1][T_2][T_3] \dots [T_N] = \begin{bmatrix} T_{11} & T_{12} \\ T_{21} & T_{22} \end{bmatrix} \tag{2.17}$$

The surface impedance of a sample can then be expressed as

$$Z_s = \frac{ST_{11}}{T_{21}} \tag{2.18}$$

from which both the reflection coefficient R and normal incident sound absorption coefficient α can be determined using Equation (2.14) and Equation (2.15) respectively.

The transmission loss through a sound absorber is defined as the ratio of the transmitted to the incident sound intensity in dB or

$$TL = 10\log_{10}\left(\frac{I_{inc}}{I_{tr}}\right) \tag{2.19}$$

where I_{inc} and I_{tr} are the incident and transmitted sound intensities respectively (See Figure 2.8). The transmission loss for a layered sound absorber can then be expressed as

$$TL = 10\log_{10}\left\{\frac{1}{4}\left|T_{11} + \frac{ST_{12}}{\rho c} + \frac{\rho c T_{21}}{S} + T_{22}\right|^2\right\} \quad (2.20)$$

where T_{11}, T_{12}, T_{21}, and T_{22} are the transfer matrix terms.

2.5 Sound Absorption Measurement

The normal incident sound absorption coefficient is measured in an impedance tube using a wave decomposition method. The testing procedure has been standardized in ASTM E1050 (1998) and the similar ISO 10534-2 (1998). The instrumentation includes a loudspeaker source, and a tube with two microphones as shown in Figure 2.5. A sample of the sound absorber is placed at the opposite end of the tube.

The test result will be valid below the plane wave cutoff frequency of the tube. Two tubes are used in this work. The tube diameters are 34.9 mm and 98.4 mm which correspond to approximate cutoff frequencies of 5750 and 2000 Hz respectively. The cutoff frequency of an impedance tube can be determined using (Pierce, 1981)

$$f_{cut} = 1.84\frac{c}{\pi d} \quad (2.21)$$

The cutoff frequency corresponds to the frequency of the first cross-mode in the tube.

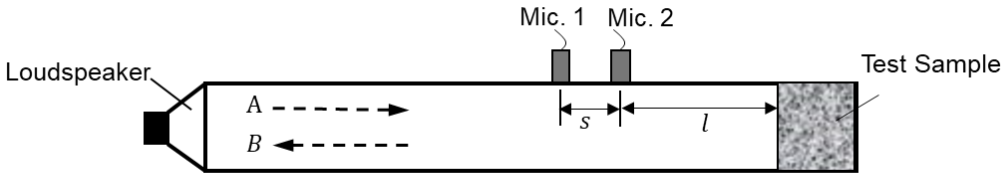

Figure 2.5 Schematic showing measurement setup for ASTM E1050.

The sound pressure $p(x)$ for plane waves in an impedance tube can be expressed as

$$p(x) = P^{+}e^{-jkx} + P^{-}e^{jkx} \tag{2.22}$$

where P^{+} and P^{-} are complex constants. k is the acoustic wavenumber defined as ω/c where ω is the angular frequency in rad/s and c is the speed of sound which is 343 m/s in air. x indicates the position. The first term on the right hand side represents the forward propagating wave and the second term the reflected wave. The particle velocity can be expressed as

$$u(x) = \frac{1}{\rho c}(P^{+}e^{-jkx} - P^{-}e^{jkx}) \tag{2.23}$$

where ρ is the mass density and c is the speed of sound.

The sound reflection coefficient is defined as

$$R = P^{-}/P^{+} \tag{2.24}$$

Notice that R will be a complex number and a function of frequency. Using Equation (2.22) and solving for the ratio defined by R, the sound reflection coefficient can then be expressed as

$$R = \frac{H_{12} - e^{-jks}}{e^{jks} - H_{12}} e^{j2k(l+s)} \tag{2.25}$$

where H_{12} is the transfer function between the sound pressure at microphone locations 1 and 2 or P_1/P_2.

The surface impedance can be determined from the reflection coefficient and is expressed as

$$Z = \frac{p}{u} = \frac{A + B}{(A - B)/\rho c} = \rho c \frac{1 + R}{1 - R} \tag{2.26}$$

Recall that the surface impedance is often used in simulation models. In addition, the sound absorption can then be expressed as

$$\alpha = 1 - |R|^2 \tag{2.27}$$

The normal incident sound absorption is the most commonly used metric to assess different sound absorbing materials.

A good quality measurement of the sound absorption depends a great deal on the instrumentation used. The microphones should be measurement grade and must be calibrated with respect to one another. The model number of the microphones used was PCB 426E01. This can be accomplished by making one measurement in an empty tube and then reversing the two microphones. In addition, the sample must be properly sized so that the sample fits snugly in the tube but is not compressed which would change the properties. A compression driver (JBL 2426H) loudspeaker was used as the source. A compression driver provides adequate power at higher frequencies.

2.6 Diffuse Field Sound Absorption Measurement

The diffuse field sound absorption (α_{diff}) is measured in a special reverberation room. Reverberation rooms are generally hard on all sides. Rotating diffusers are often added to the rooms to prevent low frequency modes from affecting the measurements. Room acoustics theory is assumed. In that case the sound pressure in the room can be expressed as

$$p_{rms}^2 = \frac{4\rho c W_{diss}}{\alpha_{diff} S} \tag{2.28}$$

where S is the surface area of the room and W_{diss} is the dissipated sound power. The input power to the room must be equivalent to the dissipated power. If the input power remains constant, then

$$p_{rms}^2 S \alpha_{diff} = \text{constant} \tag{2.29}$$

where p_{rms} is the spatially averaged root mean square sound pressure in the room.

If the diffuse field sound absorption is known for the empty room, the sound absorption of a sound absorptive sample placed on the floor of the room can be calculated. Using the same input source power, the spatially averaged sound pressure is measured before (p_{before}^2) and after (p_{after}^2) the sound absorber is placed on the floor of the room. The diffuse field sound absorption of the sample is then determined using

$$\frac{p_{before}^2}{p_{after}^2} = \frac{\alpha_{room} S_{room} + \alpha_{sample} S_{sample}}{\alpha_{room} S_{room}} \tag{2.30}$$

where α_{room} and α_{sample} are the diffuse field sound absorption of the room and sample respectively. The unknown to be solved for is α_{sample}. Normally, the sample size according to ASTM C423 (2007) is 2.44 m × 2.74 m.

The tests in this study were conducted in a 10.87 m^3 reverberation room with an approximately 2 m high ceiling. Based on past investigations, the reverberation room is suitable for tests above 150 Hz (Jackson, 2003). The sound source is a distributed field loudspeaker. The temperature of the room is approximately 25° C and the humidity is approximately 60%.

2.7 Transfer Impedance

The transfer impedance is a property that is frequently used to describe thin elements such as perforates, microperforated panels, acoustic fabrics, or thin sound absorbers. It is an acoustic series impedance. The transfer impedance is defined as the acoustic pressure difference (Δp) between both sides of an element and the particle velocity (v). The particle velocity is assumed to be the same on both sides of the element.

2.7.1 Transfer Impedance Modeling

The transfer impedance can be expressed as a transfer matrix as

$$\begin{pmatrix} p_1 \\ v_1 \end{pmatrix} = \begin{bmatrix} 1 & Z_{tr} \\ 0 & 1 \end{bmatrix} \begin{pmatrix} p_2 \\ v_2 \end{pmatrix} \tag{2.31}$$

where p_1, v_1 and p_2, v_2 are the respective acoustic pressures and velocities on both sides of the panel.

The above transfer matrix can also be converted to a transfer admittance matrix which is used in most finite element software packages. The transfer admittance is expressed as

$$\begin{pmatrix} v_1 \\ v_2 \end{pmatrix} = \begin{bmatrix} A_p & -A_p \\ -A_p & A_p \end{bmatrix} \begin{pmatrix} p_1 \\ p_2 \end{pmatrix} \tag{2.32}$$

where $A_{\mathrm{p}} = \frac{1}{Z_{tr}}$ is the reciprocal of the transfer impedance, and $v_1 = -v_2$. If a transfer admittance relationship is used, there will be no need to model the individual holes in a perforate.

When using numerical methods, it is easier to find a modified four-pole parameters (Munjal, 1987, Wu et al., 1998). The modified four-pole parameters are defined as:

$$\begin{aligned} A^* &= p_1|_{v_1=1, v_2=0} & B^* &= p_1|_{v_1=0, v_2=-1} \\ C^* &= p_2|_{v_1=1, v_2=0} & D^* &= p_2|_{v_1=0, v_2=-1} \end{aligned} \tag{2.33}$$

where p_1 and p_2 are the acoustic pressure at the inlet and outlet respectively. A^* and C^* can be found by applying a unit velocity on the left end, which is $v_1 = 1$. For a symmetric component, $A^* = D^*$, and $B = C^*$. The modified four-pole parameters can be expressed as (Herrin, et al., 2007)

$$\begin{aligned} A &= A^*/C^* & B &= B^* - A^*D^*/C^* \\ C &= 1/C^* & D &= -D^*/C^* \end{aligned} \tag{2.34}$$

2.7.2 Series Impedance and Parallel Impedance

Many acoustic elements can be categorized as either series or parallel impedances. Acoustic impedances are defined as the ratio of the sound pressure to the particle velocity. Sound pressure is an effort quantity which is analogous to electrical voltage whereas particle velocity is a flow quantity analogous to electrical current.

A series impedance assumes that the particle velocity is constant ($u_1 = u_2$ in Figure 2.6) whereas the sound pressure is discontinuous. This element is also referred to as a transfer impedance and is defined mathematically as

$$z_{tr} = \frac{p_1 - p_2}{u_1} \tag{2.35}$$

where p_1 and p_2 are the sound pressures on opposing sides of the element as shown in Figure 2.6. The analogous circuit is also indicated.

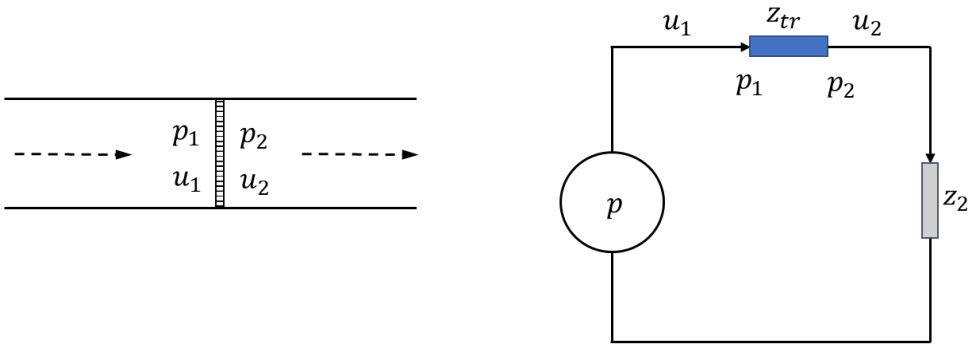

Figure 2.6 Schematic of perforated plate and equivalent electrical circuit.

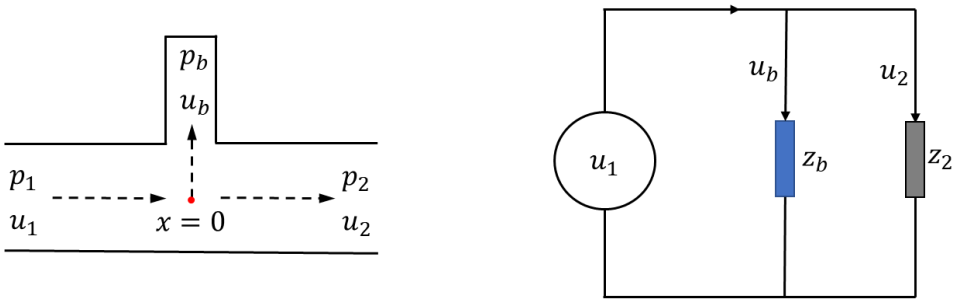

Figure 2.7 Schematic of quarter wave tube and its equivalent electrical circuit.

For a parallel acoustic impedance, the sound pressure is assumed to be constant at a junction between elements while the volume velocity is divided. A parallel impedance is commonly used to simulate side branch resonator elements such as quarter wave tubes and Helmholtz resonators. To insure mass continuity, the volume velocity at the junction can be defined as

$$S_1 u_1 = S_b u_b + S_2 u_2 \tag{2.36}$$

where S_1 and S_2 are surface areas, u_1 and u_2 are respective particle velocities as shown in Figure 2.7, and S_b and u_b are the surface area and particle velocity for the branch or parallel element. Since sound pressure is constant across the junction, Equation (2.36) can be expressed in terms of acoustic impedances as

$$\frac{1}{Z_1} = \frac{1}{Z_b} + \frac{1}{Z_2} \tag{2.37}$$

where Z_b is the branch or parallel specific impedance.

2.7.3 Transfer Impedance Measurement

Transfer impedance is most easily measured using the impedance subtraction approach (Wu et al., 2003). The impedance is measured at a given

location in the impedance tube using the approach detailed in Section 2.5. The impedance is measured without and with the thin sample in place. The transfer impedance is then

$$Z_{tr} = Z_1 - Z_2 \tag{2.38}$$

where Z_1 and Z_2 are the impedances after and before placement of the sample respectively.

2.8 Transmission Loss

The standard test method for determining acoustic transmission loss is described in ASTM E2611 (2009) based on research by Bolton and Song (2000). The instrumentation used in the method includes an impedance tube with two microphones on each side. A schematic of the test setup shown in Figure 2.8. A four-channel data acquisition is preferred though a two-channel system can be used. A loudspeaker is placed on the left side of the tube. Normally, white noise is selected as the excitation though swept or stepped sine excitation is sometimes used to improve accuracy. Transfer functions are measured between the microphones in order to identify the complex wave amplitudes for both the propagating and reflected waves.

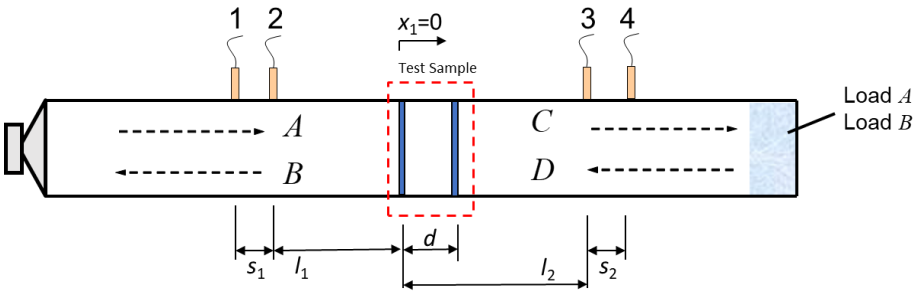

Figure 2.8 Schematic showing measurement setup for ASTM E2611.

The objective of the test is to first identify the transfer matrix of the acoustic element. After the transfer matrix is identified, the transmission loss can be determined. Additionally, the bulk properties of a sound absorber can be identified if the sound absorber is a porous absorber. Two different terminations are needed in order to obtain four equations that can be used to solve for the unknown transfer matrix elements. It is best that the terminations, also referred to as acoustic loads, be as different as possible. Hence, it is customary to use an open or closed end as one load and a sound absorbing terminations as the other. The transfer functions are normally measured instantaneously using a multi-channel data acquisition. The complex wave amplitudes can be expressed as

$$P_A = j\frac{e^{-jkl_1} - H_{2,1}e^{-jk(l_1+s_1)}}{2\sin ks_1} \tag{2.39}$$

$$P_B = j\frac{H_{2,1}e^{jk(l_1+s_1)} - e^{jkl_1}}{2\sin ks_1} \tag{2.40}$$

$$P_C = j\frac{H_{3,1}e^{jk(l_2+s_2)} - H_{4,1}e^{jkl_2}}{2\sin ks_2} \tag{2.41}$$

$$P_D = j\frac{H_{4,1}e^{-jkl_2} - H_{3,1}e^{-jk(l_2+s_2)}}{2\sin ks_2} \tag{2.42}$$

where $H_{2,1}, H_{3,1}$, and $H_{4,1}$ are the transfer functions assuming Mic 1 is the reference for phase. The sound pressure and particle velocity at $x = 0$ are defined as

$$P_0 = P_A + P_B \tag{2.43}$$

and

$$u_0 = (P_A - P_B)/\rho c \tag{2.44}$$

respectively. Likewise, the sound pressure and particle velocity at $x = d$ are defined as

$$P_d = P_C e^{-jkd} + P_D e^{jkd} \tag{2.45}$$

and

$$u_d = \left(P_C e^{-jkd} - P_D e^{jkd}\right)/\rho c \tag{2.46}$$

respectively.

The transfer matrix can be expressed as

$$\begin{Bmatrix} \widetilde{P_0} \\ \widetilde{Su_0} \end{Bmatrix} = \begin{bmatrix} \dfrac{P_{0a}u_{db} - P_{0b}u_{da}}{P_{da}u_{db} - P_{db}u_{da}} & \dfrac{P_{0b}P_{da} - P_{0a}P_{db}}{P_{da}u_{db} - P_{db}u_{da}} \\ \dfrac{u_{0a}u_{db} - u_{0b}u_{da}}{P_{da}u_{db} - P_{db}u_{da}} & \dfrac{P_{da}u_{0b} - P_{db}u_{0a}}{P_{da}u_{db} - P_{db}u_{da}} \end{bmatrix} \begin{Bmatrix} \widetilde{P_d} \\ \widetilde{Su_d} \end{Bmatrix} \tag{2.47}$$

where the subscripts a and b indicated different load cases. Transmission coefficient is defined as the ratio of the transmitted wave to the incident wave. It can be expressed as

$$t = \frac{2e^{ikd}}{T_{11} + (T_{12}/\rho c) + \rho c T_{21} + T_{22}} \tag{2.48}$$

and the normal incidence transmission loss as

$$TL_n = 20\log_{10}\left|\frac{1}{t}\right| \tag{2.49}$$

The matrix in Equation (2.47) can be related to the complex wavenumber and characteristic impedance as

$$\begin{bmatrix} A & B \\ C & D \end{bmatrix} = \begin{bmatrix} \cos(k_c d) & j\rho'c'/S\sin(k_c d) \\ jS\sin(k_c d)/(\rho'c') & \cos(k_c d) \end{bmatrix} \tag{2.50}$$

The characteristic impedance and complex wavenumber can be expressed as

$$z_c = \sqrt{\frac{B}{C}} \tag{2.51}$$

and

$$k_c = \frac{arc\tan(\frac{B}{jAz_c})}{d} \tag{2.52}$$

respectively.

The complex speed of sound and density can be expressed as

$$c' = \frac{\omega}{k_c} \tag{2.53}$$

and

$$\rho' = \frac{k_c z_c}{\omega} \tag{2.54}$$

Chapter 3 MICRO-PERFORATED PANEL ABSORBERS

(Note: Most of the research in this chapter has been previously documented in Liu et al., 2017)

3.1 Introduction

The microperforated panel (MPP) and backing cavity are best considered as a system for which the sound absorption can be tuned by varying the spacing between the panel and a wall. Due to the small hole size, sound energy is dissipated via viscous friction. The amount of energy dissipated is related to the particle velocity in the holes, and losses are greater when the velocity is high. The acoustic particle velocity is negligible near enclosure surfaces, therefore, the MPP is usually placed approximately 1/4, 3/4, 5/4 … wavelength away from a surface to maximize the particle velocity in the holes. Hence, the depth of the backing cavity plays an important role in the MPP absorber function.

In practice, the volume of the backing airspace is limited. In the 1970s, Wirt (1975) proposed several novel sound-absorbing structures behind single-layer absorbers. These included variable length channels, cones, and Helmholtz resonators. Recently, Hua et al. (2013) implemented three-channel, two-channel, and conical backing cavities. Park (2013) placed a tuned Helmholtz resonator behind the MPP to target low-frequency noise; a concept that is functionally equivalent to the conical backed cavity of Hua et al. (2013).

Alternatively, Sakagami et al. (2006) and Zhang (1998) examined the use of double leaf MPP configurations to improve the broadband absorption of the MPP absorber. Sakagami et al. (2010) inserted honeycomb partitioning between the two

layers to force plane wave behavior in between the perforate layers. This proved to be advantageous.

In prior work, Liu and Herrin (2010) demonstrated that MPP absorbers perform better when the backing cavity is partitioned. Partitioning forces the MPP absorber to perform like a locally reacting absorber by insuring plane wave propagation behind the MPP. Simulation and measurement results indicated that the grazing wave attenuation was significantly supplemented by the addition of partitioning.

In most prior MPP absorber studies, the normal incidence absorption has been measured using ASTM E1050 (1998). Though results are useful, the diffuse field absorption coefficient is also of interest and is perhaps more indicative of the performance of the MPP absorber in an enclosure.

In the current work, several MPP configurations are measured using the small reverberation room developed by Jackson (2003). The room has a volume of 10.87 m^3 and is suitable above roughly 150 Hz. The test is based on the ASTM C423 standard (2009). Several backing configurations are considered which include multi-channels, Helmholtz resonators, tapered partitions (i.e. cones), and double leaf configurations. Measurements were performed using a square impedance tube.

3.2 Transfer Impedance Model

Perforates and covers are usually modeled as a transfer impedance and used in numerical simulation (i.e., finite or boundary element models). A transfer or series impedance is defined as the difference in acoustic pressure divided by

the particle velocity which is assumed to be the same on both sides of the perforate or cover due to the small thickness. Hence the transfer impedance can be expressed as

$$z_{tr} = \frac{p_1 - p_2}{u} \tag{3.1}$$

where p_1 and p_2 are the respective acoustic pressures on both sides of the panel, and u is the particle velocity.

A schematic of a MPP and backing cavity are shown in Figure 3.1. Maa's (1975) well known equation as recast by Allam and Åbom (2013) can be expressed as

$$r_c = \mathrm{Re}\left(\frac{j\omega t}{\sigma c}\left(1 - \frac{2}{\kappa\sqrt{-j}}\frac{J_1\left(\kappa\sqrt{-j}\right)}{J_0\left(\kappa\sqrt{-j}\right)}\right)^{-1}\right) + \frac{2\beta R_s}{\sigma\rho c} \tag{3.2}$$

and

$$x_c = \mathrm{Im}\left(\frac{j\omega t}{\sigma c}\left(1 - \frac{2}{\kappa\sqrt{-j}}\frac{J_1\left(\kappa\sqrt{-j}\right)}{J_0\left(\kappa\sqrt{-j}\right)}\right)^{-1}\right) + \frac{0.85d\omega}{\sigma c} \tag{3.3}$$

where r_c and x_c are the real and imaginary parts of the normalized transfer impedance respectively. Geometric parameters include hole diameter (d), porosity (σ) and thickness (t). J_0 and J_1 are the Bessel function of the first kind of zeroth and first order respectively. κ is the dimensionless shear wave number which relates the hole diameter to the viscous boundary layer thickness and is expressed as

$$\kappa = d\sqrt{\omega/4\nu} \tag{3.4}$$

where ν is the kinematic viscosity. R_s is the surface resistance and is defined as

$$R_s = \frac{\sqrt{2}}{2}\sqrt{\eta\rho\omega} \tag{3.5}$$

where η is dynamic viscosity. In the above equations, ω is the angular frequency, ρ is the density of the fluid, and c is the speed of sound. β is equal to 2 for holes with rounded edges and 4 for holes with sharp edges.

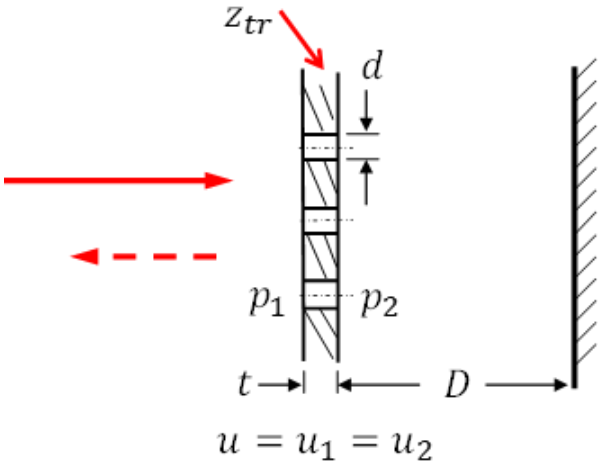

Figure 3.1 Schematic of microperforated panel and backing cavity.

The normalized impedance of the perforate and backing cavity can be expressed as

$$\mathrm{Z} = r_c + x_c - \mathrm{j}\cot(\omega D/c) \tag{3.6}$$

where D is the backing cavity depth. Once the normalized surface impedance (Z) is determined, the normal incident absorption coefficient can be expressed as

$$\alpha = \frac{4Z_R}{(1+Z_R)^2 + Z_I^2} \tag{3.7}$$

where Z_R and Z_I are the real and imaginary parts of the normalized impedance respectively.

Figure 3.2 illustrates the effect of varying the cavity depth on the absorption coefficient. Increasing the cavity depth, improves the low frequency sound absorption. Note that the sound absorption is low at frequencies below and above the frequency band of high sound absorption.

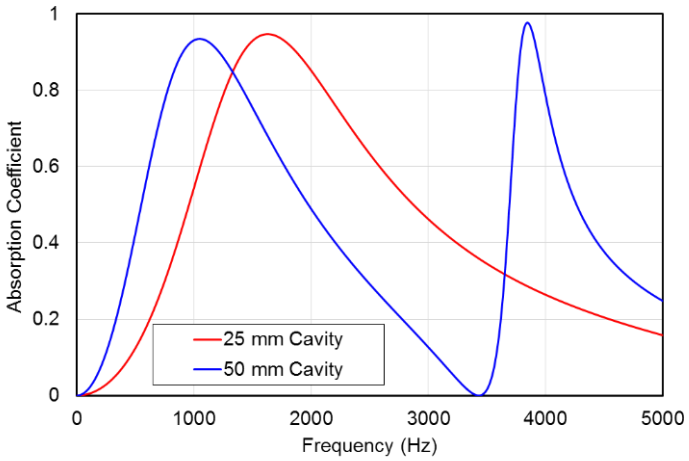

Figure 3.2 Absorption coefficient of a MPP panel with different cavity depth.

3.3 Plane Wave Model

Assuming plane wave sound propagation through the MPP and backing cavity, the backing is most easily modeled using transfer matrix theory (Zhang, 2005). A transfer matrix relates the sound pressure and particle velocity from one (p_1 and u_1) to the other side (p_2 and u_2) of an acoustic element. Hence,

$$\begin{Bmatrix} p_1 \\ S_1 u_1 \end{Bmatrix} = \begin{bmatrix} T_{11} & T_{12} \\ T_{21} & T_{22} \end{bmatrix} \begin{Bmatrix} p_2 \\ S_2 u_2 \end{Bmatrix} \tag{3.8}$$

where T_{11}, T_{12}, T_{21}, and T_{22} are the transfer matrix elements. S_1 and S_2 are the cross-sectional area at different points in the channel. The transfer matrix for a MPP is given by

$$[T_{tr}] = \begin{bmatrix} 1 & z_{tr}/S \\ 0 & 1 \end{bmatrix}. \tag{3.9}$$

where z_{tr} is the transfer impedance. The transfer matrix for a straight duct can be expressed as

$$[T_{sd}] = \begin{bmatrix} \cos(kL) & jz/S\sin(kL) \\ jS\sin(kL)/\mathrm{z} & \cos(kL) \end{bmatrix} \tag{3.10}$$

where k is the acoustic wavenumber and L is the length of the duct. A cone or tapered duct can be modeled as a series of straight ducts of decreasing or increasing cross-section using Equation (3.9). Alternatively, Munjal (2014) provides an equation for the transfer matrix of a cone in his text.

The transfer matrix for a side branch can be expressed as

$$[T_{br}] = \begin{bmatrix} 1 & 0 \\ S/z_{br} & 1 \end{bmatrix} \tag{3.11}$$

where z_{br} is the side branch impedance. The impedance for a side branch can be determined by using the above equations as well. A transfer matrix is developed from the start to the termination of the side branch. Assuming that the termination of the side branch is rigid, the side branch impedance (z_{br}) can be expressed as

$$z_{br} = \frac{T_{11}}{T_{21}} \tag{3.12}$$

Each of the designs considered consist of the aforementioned basic elements.

3.4 Double Layer MPP

A popular approach has been to use multi-leaf configurations to improve performance. Sakagami et al. (2010) and Zhang and Gu (1998) used double-leaf MPP configurations to improve broadband sound absorption. A double-leaf MPP is usually made of two single layer MPPs with honeycomb glued between them.

The configuration can be modeled using plane wave analysis. Each MPP layer is treated as a transfer impedance. The cavity between the panels is simulated as a straight duct. Dimensions of channels of the honeycomb are small, therefore, the thermo-viscous effect in the honeycomb should be included. Keefe (1984) developed equations to calculate complex density (ρ') and complex sound speed (c') in cylindrical ducts

$$\rho' = \frac{\rho}{1 - F(s)} \tag{3.13}$$

and

$$c' = \frac{(1 - F(s))^{1/2}}{(1 + (\gamma - 1)F(\sqrt{\nu}s))^{1/2}} \tag{3.14}$$

where γ is the specific heat ratio and ν is the Prandtl number. s is the ratio of hydraulic channel radius to the viscous boundary layer thickness,

$$s = \frac{a}{(\eta/\rho\omega)^{1/2}} \tag{3.15}$$

where η is the shear viscosity coefficient and a is the hydraulic channel radius. $F(s)$ is defined in terms of Bessel functions of the first kind as

$$F(s) = \frac{2}{\sqrt{-j}s}\frac{J_1(\sqrt{-j}s)}{J_0(\sqrt{-j}s)} \tag{3.16}$$

Based on Equation (3.13) through Equation (3.16), the transfer matrix for the honeycomb is expressed as

$$[T_1] = \begin{bmatrix} \cos(k'L) & j\rho'c'/S\sin(k'L) \\ jS\sin(k'L)/(\rho'c') & \cos(k'L) \end{bmatrix} \tag{3.17}$$

where L is the distance between two MPP and S is the sample area. The transfer matrix of a single layer MPP is given by Equation (3.9). Accordingly, the transfer matrix of the configuration shown in Figure 3.3 can be expressed as

$$[T] = [Z_{tr}][T_1][Z_{tr}] \tag{3.18}$$

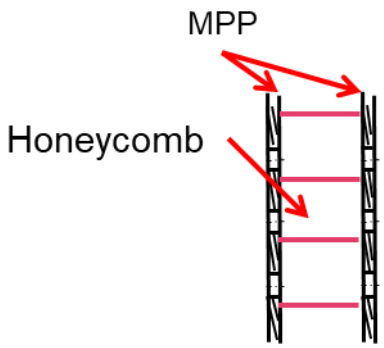

Figure 3.3 Schematic showing double leaf MPP with honeycomb.

3.5 MPP Backing Designs

In this chapter, five different backing configurations are considered. Concepts include a) empty airspace, b) three-channel, c) Helmholtz resonator, d) tapered partition, and e) double leaf (with honeycomb) configurations. The configurations are illustrated in Figure 3.4.

The aim of this work is to improve sound absorptive performance a) by varying the depth of the backing cavity or b) by adding resonators behind the MPP. There are two features of the MPP which drive the rationale. First, the MPP is a

viscous sound absorber and is most effective when the particle velocity is high in the MPP pores. This roughly corresponds to a backing cavity depth on the order of one-quarter wavelength. By varying or having multiple cavity depths, the MPP sound absorber will exhibit broadband sound absorptive performance. Secondly, the MPP is acoustically transparent when the particle velocity is low in the pores. Hence, reactive sound absorbers can be placed behind the MPP and can supplement MPP performance.

The three-channel configuration shown in Figure 3.4 (b) has 3 separate cavity depths and hence should absorb well in 3 different frequency bands. Notice that the lower channel wraps around the middle channel and terminates behind the upper channel. Hence, the lower channel is effectively longer than the spacing between the MPP and wall. This should improve the lower frequency attenuation. The Helmholtz resonator configuration shown in Figure 3.4 (c) offers a shorter cavity depth coupled with a Helmholtz resonator. The MPP should only slightly impact the performance of the Helmholtz resonator since the particle velocity is low in the pores at the frequency where the resonator is effective. However, the particle velocity will be high in the perforations at high frequencies. This permits the designer to incorporate reactive lower frequency and resistive higher frequency attenuation into the same space. The tapered configuration shown in Figure 3.4 (d) is functionally equivalent to the Helmholtz resonator of Figure 3.4 (c). The upper channel functions as a variable depth cavity providing broadband attenuation. The lower chamber functions as a Helmholtz resonator whose neck is the opening connecting the upper and lower chambers. Figure 3.4 (e) shows the double leaf

configuration which provides broader band attenuation than that of a single leaf. Staggering MPP sound absorbers permits high sound absorption in different frequency bands.

Figure 3.5 shows the plane wave representations of each. Dashed lines indicate perforates, rectangles indicate straight ducts, and triangles and tapered rectangles indicate tapered ducts. Tapered ducts are modeled as a cone or as a series of straight ducts.

Figure 3.6 compares the plane wave simulation to the measured normal incident sound absorption. From Figure 3.6, it is evident that the three-channel, Helmholtz resonator, and tapered channel concepts improve the performance below 400 Hz. The Helmholtz resonator concept exhibits higher absorption but in a narrower frequency range below 400 Hz. In addition, the sound absorption is greatly improved above 800 Hz. However, the performance is degraded between 400 and 800 Hz. The double leaf configuration improves the sound absorption below 400 Hz and above 1200 Hz.

There is some discrepancy in the results for the Helmholtz resonator and tapered partition (Figure 3.6 (c) and (d)). This is typical of results when the sound absorption is theoretically low. In the authors' opinion, the most likely reason for the discrepancy is that vibration of the MPP or the backing structure adds damping and hence some appreciable additional sound absorption.

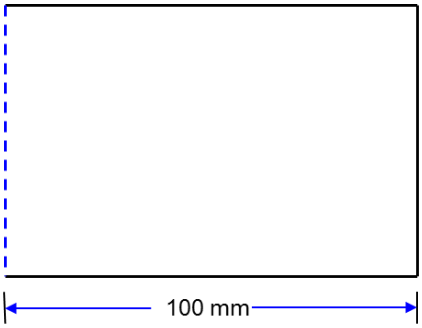

(a) Empty airspace

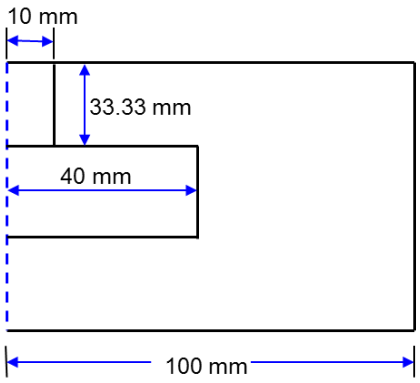

(b) Three-channel

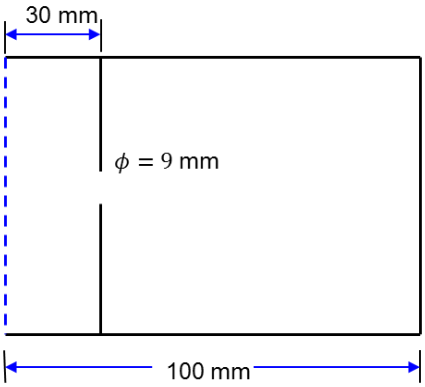

(c) Helmholtz resonator

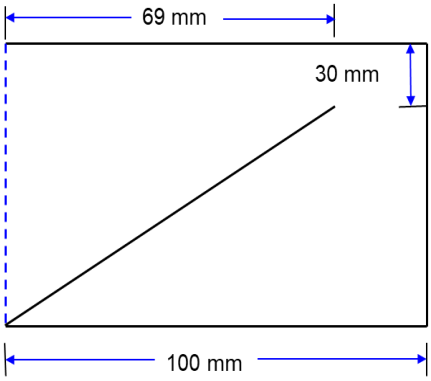

(d) Tapered partition

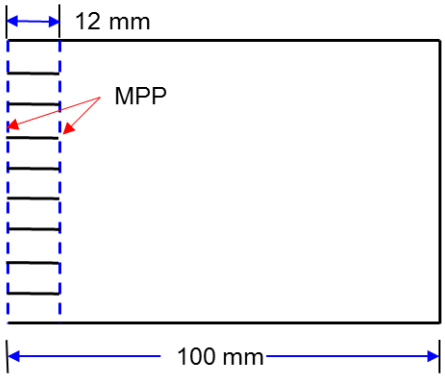

(e) Double leaf MPP

Figure 3.4 Schematics of different backing cavity design.

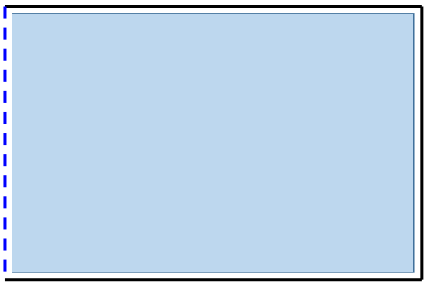

(a) Empty airspace

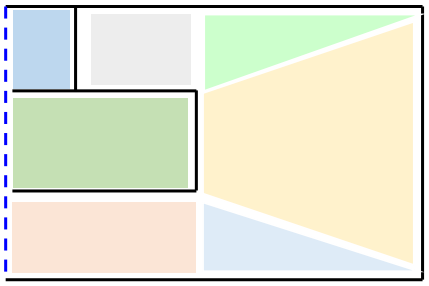

(b) Three-channel

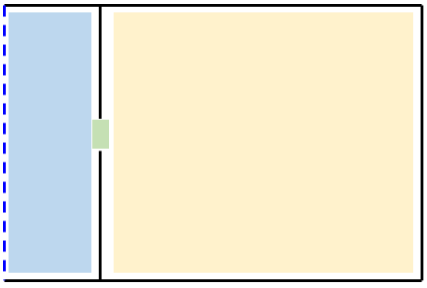

(c) Helmholtz resonator

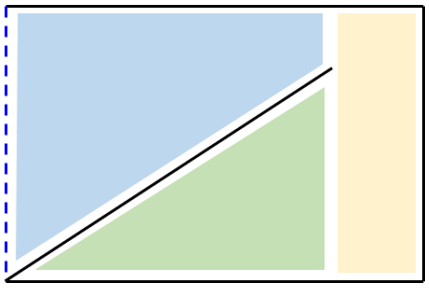

(d) Tapered partition

(e) Double leaf MPP

Figure 3.5 Plane wave modeling strategies.

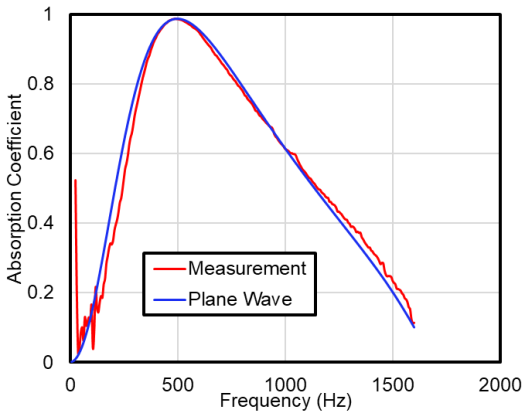

(a) Empty airspace

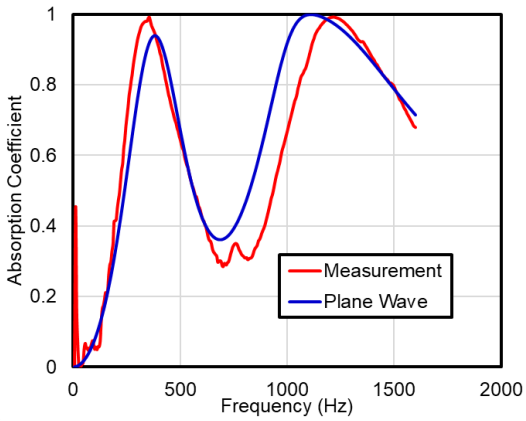

(b) Three-channel

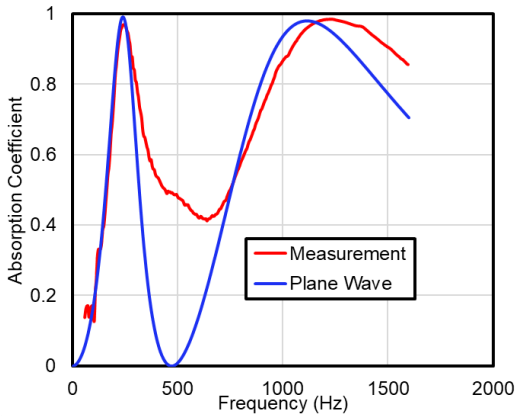

(c) Helmholtz resonator

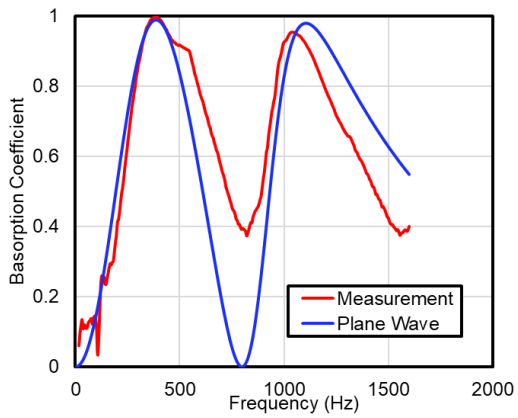

(d) Tapered partition

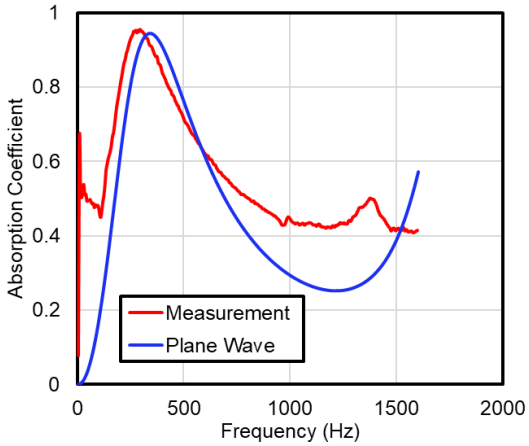

(e) Double leaf MPP

Figure 3.6 Comparison of measured and plane wave simulated sound absorption.

3.6 Small Enclosure Results

The different MPP backing concepts were positioned at the end of a small enclosure to assess their performance with three-dimensional wave propagation. A schematic of the enclosure is shown in Figure 3.7. A loudspeaker was connected to the 970 × 580 × 410 mm^3 enclosure on one side via a short tube. Measurements were made on a plane 50 mm from the treatment at 12 positions. For each design concept, the spatially averaged sound pressure was determined on the plane and compared with the spatially averaged sound pressure for the untreated (no MPP present) enclosure. Since the enclosure is highly resonant, the insertion loss was first computed narrowband and then a 200 Hz running average was used to smooth the data for comparison sake.

Five different cases were considered. They are labelled accordingly:

A. No partitioning – The airspace behind the MPP is empty.

B. Partitioned – The airspace behind the MPP is partitioned.

C. Partitioned with alternating Helmholtz resonators – The airspace behind the MPP is partitioned. Helmholtz resonators and empty channels are alternated.

D. Partitioned with alternating tapered ducts - The airspace behind the MPP is partitioned. Tapered partitions and empty channels are alternated.

E. Double leaf MPP – A double leaf MPP with separation distance of 12 mm between layers is used. Honeycomb partitioning is epoxied between the two MPP layers. The cavity is empty behind the MPP.

For cases B, C, and D, partitions were 99×95 mm^2.

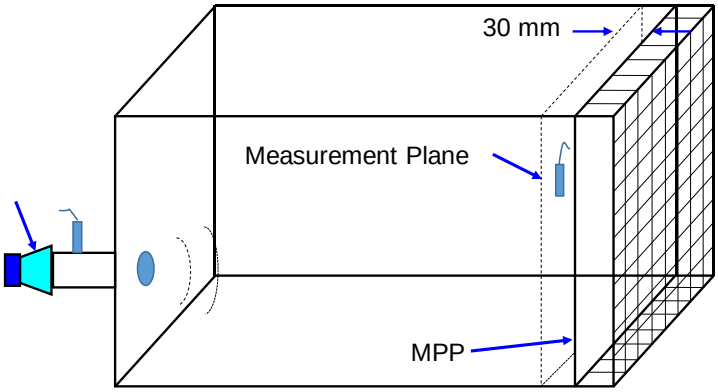

Figure 3.7 Schematic showing small enclosure and MPP placement.

Figure 3. 8 shows the insertion loss comparisons. By comparing the *no partitioning* and *partitioned* cases, it can be observed that partitioning improves the attenuation at frequencies below 500 Hz. This is anticipated since the first cross modes occur at approximately 295 Hz and 420 Hz. Partitioning will especially improve the attenuation at these frequencies since sound waves will be grazing in the unpartitioned case. The *partitioned with alternating Helmholtz resonator* case also improves upon the baseline (*no partitioning*) at low frequencies. However, the effect due to the Helmholtz resonators at low frequencies is minimal. Also, note that the reduced cavity depth of 30 mm due to the added plate greatly improves the high frequency performance of the sound absorber. The *partitioned with alternating tapered ducts* case has a performance similar to the *partitioned with alternating Helmholtz resonator* case. However, the attenuation above 1000 Hz is roughly 2 dB lower. The double leaf MPP performs similar to the baseline case at low frequencies, but the attenuation is improved between 2 and 5 dB at higher frequencies.

Both the MPP and the partitions themselves likely have lower frequency structural resonances that may improve or degrade the performance. The double leaf MPP construction is much sturdier than the other case and so structural resonances are less likely in that case. Also, note that the insertion loss is negative between 450 and 700 Hz. This is likely due to the size of box cavity changing with the added treatments.

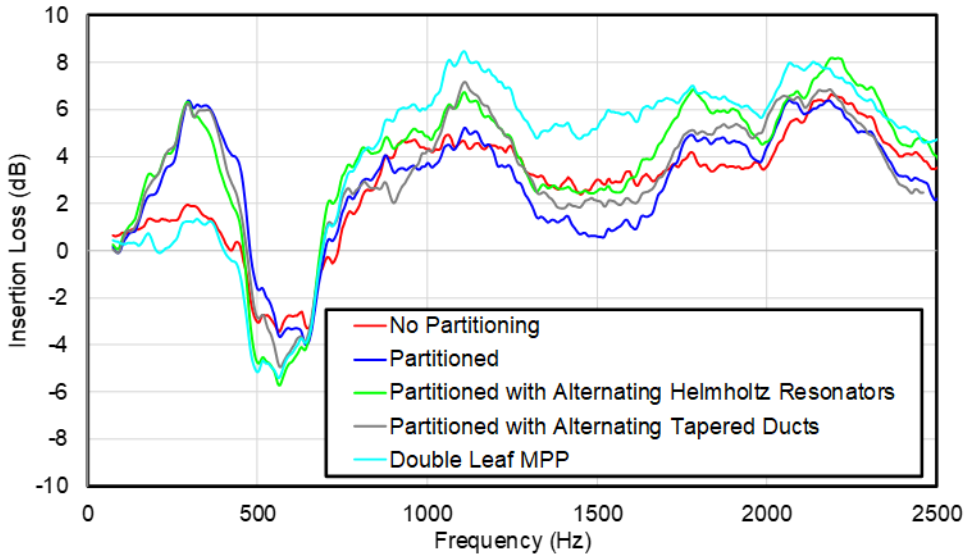

Figure 3. 8 Schematic showing small enclosure and MPP placement.

3.7 Reverberation Room Test

Diffuse field sound absorption measurements were performed in a 10.87 m^3 reverberation room with an approximately 2 m high ceiling and no parallel walls. Based on past investigations, the reverberation room is suitable for tests above 150 Hz (Jackson, 2003). The sound source is a distributed field loudspeaker. The test samples are prepared and fit into a 0.6 m × 0.4 m metal box with wood frame. Figure (3.9 shows one of the samples positioned on the floor of the small reverberation room. The test temperature is approximately 20°C and the humidity

is about 58% ~ 62%. The test requirements are detailed in ASTM C423 (2009). The metal box contains 24 cells each with a 0.1 m x 0.1 m size. This size is similar to the square impedance tube cross-section discussed in Section 3.5. Samples were placed at the center of the reverberation room in the same position for all tests.

Nine different cases were tested and are listed below.

A. Unpartitioned

B. Partitioned with empty cavities

C. Three-channel

D. Three-channel and empty cavities are alternated

E. Helmholtz resonators

F. Helmholtz resonators and empty cavities are alternated

G. Tapered ducts

H. Tapered ducts and empty cavities are alternated

I. Double leaf MPP

Photographs of the manufactured backings are shown in Figure 3.10.

Figure 3.9 Test setup in reverberation room.

(a) Partition

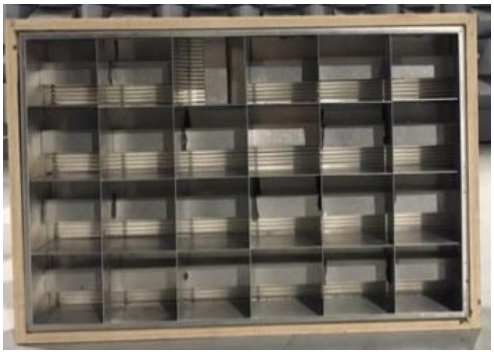

(b) Three-channel

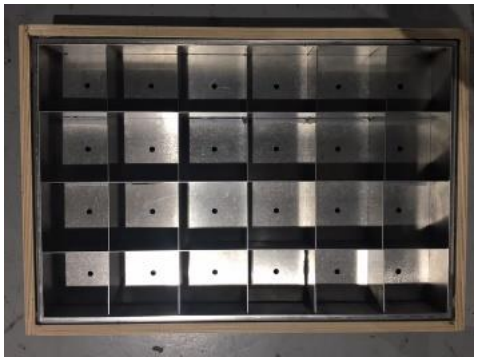

(c) Helmholtz resonator

(d) Tapered duct

(e) Double leaf MPP

Figure 3.10 Configurations of different concepts.

Figure 3.11 shows the diffuse field sound absorption results. In Figure 3.11 (a), it can be seen that partitioning the backing cavity improves the broadband sound absorption. There is a notable improvement between 400 and 1000 Hz. Figure 3.11 (b) compares the performance for the three-channel and alternating three-channel. Notice that the performance at higher frequencies is improved and there is some improvement at lower frequencies. The low frequency performance

appears to be primarily a result of the partitioning. Figure 3.11 (c) compares the performance of the Helmholtz resonator and alternating Helmholtz resonator configurations. It can be seen that the performance at 200 Hz is greatly improved when Helmholtz resonators are placed in each cell. Both the Helmholtz resonator and alternating cases improved the sound absorption above 800 Hz. Similar results are noted for the tapered and alternating tapered configurations as shown in Figure 3.11 (d). Diffuse field sound absorption is slightly improved at the lower frequencies but is greatly improved above 1000 Hz.

The double leaf MPP is compared to the baseline case in Figure 3.11 (e). It can be seen that the double leaf MPP marginally improves the sound absorption throughout the entire frequency range. The double leaf MPP does have the advantage of being especially durable and stiff.

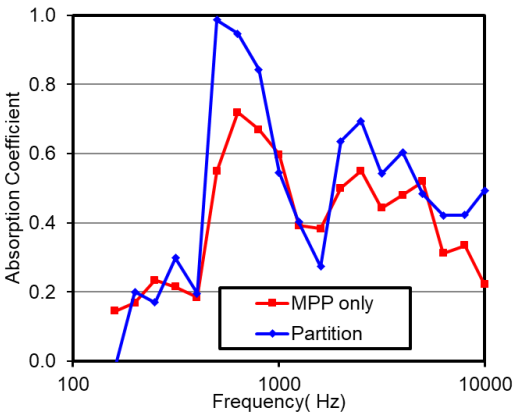

(a) Partitioned

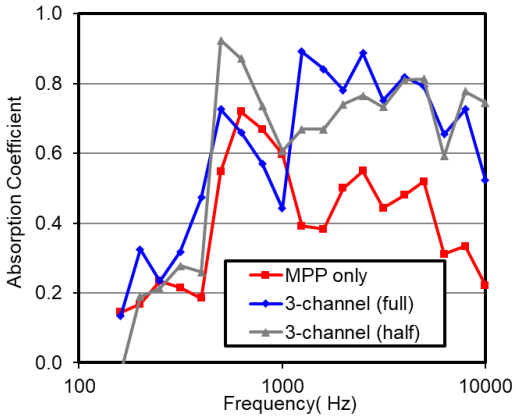

(b) Three channel

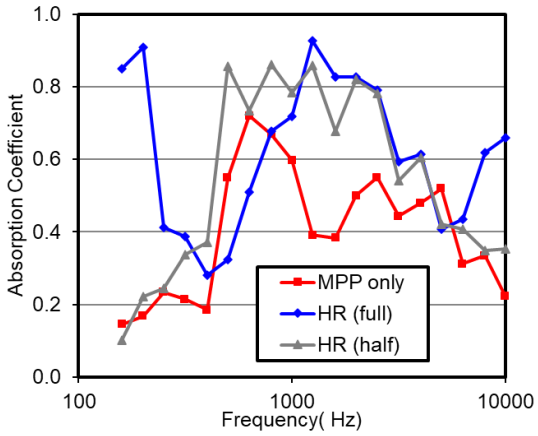

(c) Helmholtz resonator

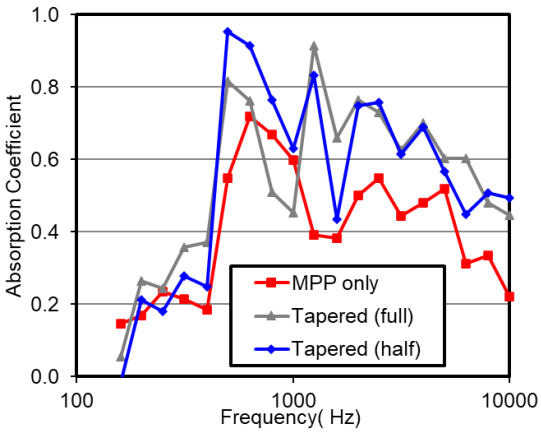

(d) Tapered partition

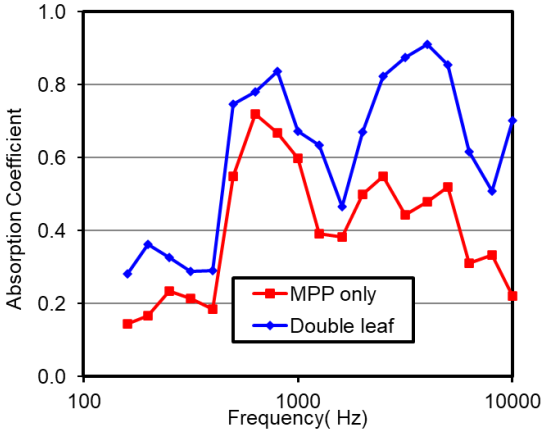

(e) Double leaf MPP

Figure 3.11 Comparison of measured absorption coefficient with baseline.

In Figure 3.12, the normal incidence and diffuse field sound absorption are compared. Though the peaks have a small shift, the trend in the plots is similar. The results seem to demonstrate that the normal incidence sound absorption can be used as a metric to compare trends in the diffuse field sound absorption.

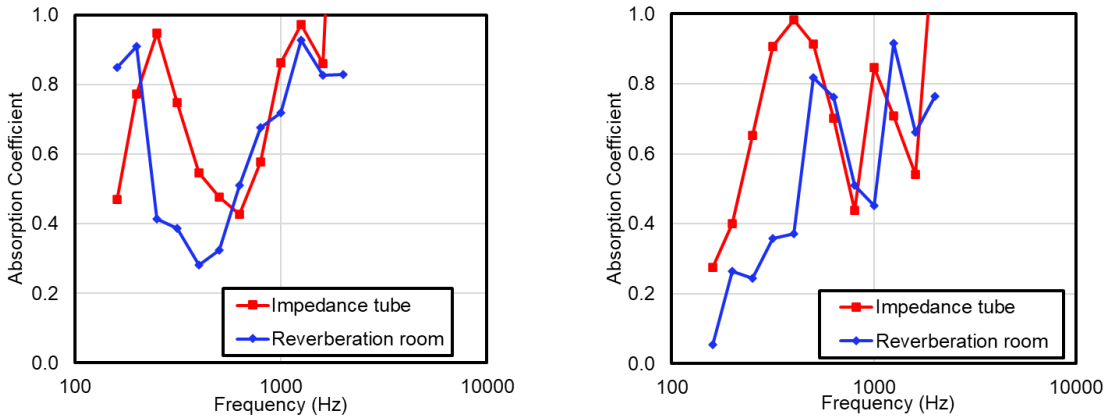

(a) Helmholtz resonator (b) Tapered partition

Figure 3.12 Comparison of test results in impedance tube and reverberation room.

3.8 Ultra-Thin Microperforated Panel Absorbers with Applications to Mufflers

The thickness of most traditional MPP is on the order of 1 mm. There have been recent MPP that are on the order of 0.25 mm thick. They are desirable for their lightweight and their usability as a cover for porous absorbers. For example, the ultra-thin MPP can be rolled and used to hold fiber in place in mufflers. If normal perforates are used, the muffler weight will be higher. Moreover, glass fiber is prone to get dislodged, blown through the perforate, and ejected out the outlet.

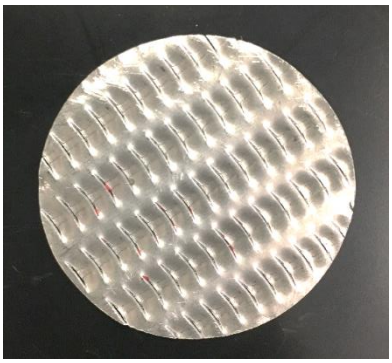

Figure 3.13 Photo of thin MPP.

A sample of the ultra-thin MPP (thickness of 0.25 mm) was cut and placed in the 34.9 mm diameter impedance tube. The sound absorption was measured and a least squares curve fit was used to determine effective parameters. The effective hole diameter was 0.23 mm and the effective perforation rate was 8%. Measured and fitted results are shown in Figure 3.14.

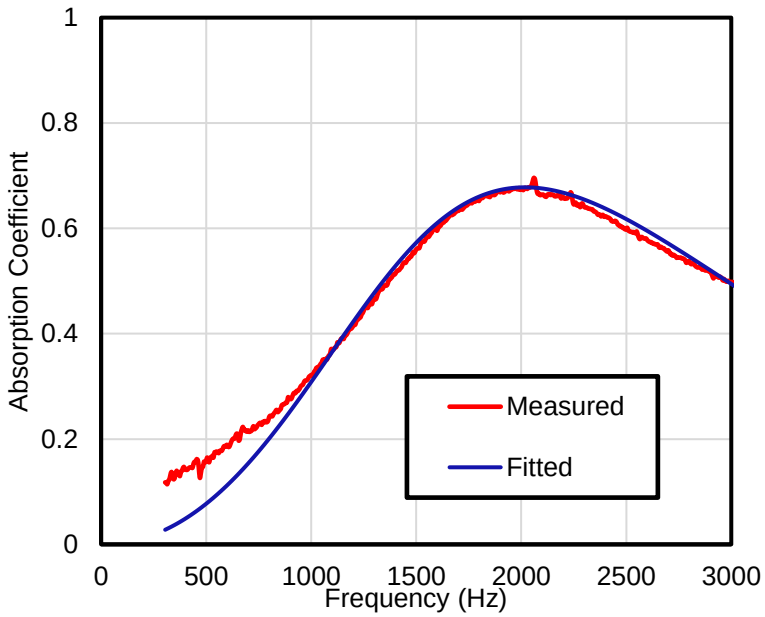

Figure 3.14 Comparison of measured and least squares curve fitted sound absorption.

Using the effective parameters, the transfer impedance of the MPP is predicted and compared with direct measurement in Figure 3.15. It can be seen that correlation is good between the two.

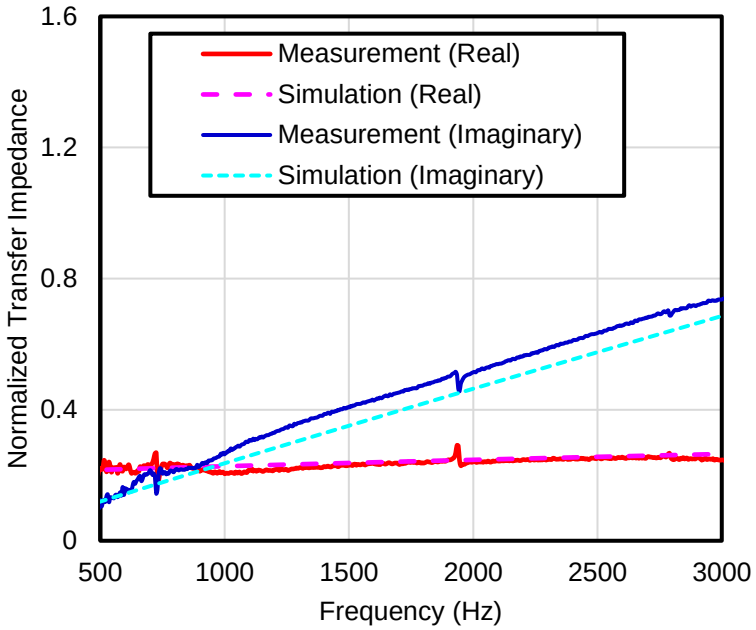

Figure 3.15 Comparison of measured and simulated normalized transfer impedance.

The ultra-thin MPP was rolled to a diameter of 5 cm and placed inside a larger cylinder with inner diameter of 15 cm as shown in Figure 3.16. The muffler was positioned in between 34.9 mm diameter impedance tubes on both sides and the transmission loss was measured. The length of the muffler is 1.22 m. Additionally, a thin pipe was inserted inside the muffler to reduce the length in 0.3 m increments.

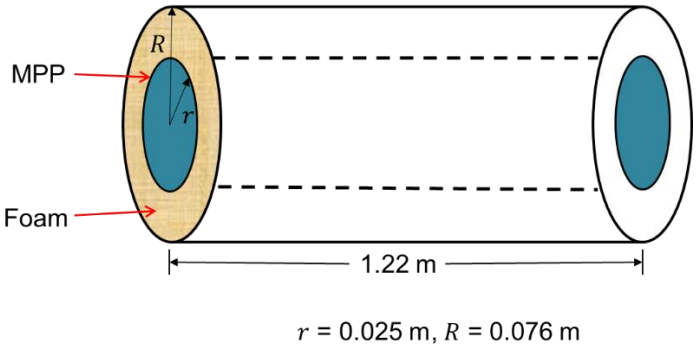

Figure 3.16 Schematic showing application of MPP in muffler.

The muffler was also simulated using the MSC Actran software (2014). The MPP was simulated using the transfer impedance and effective parameters. The model consisted of 21167 nodes and 93982 elements.

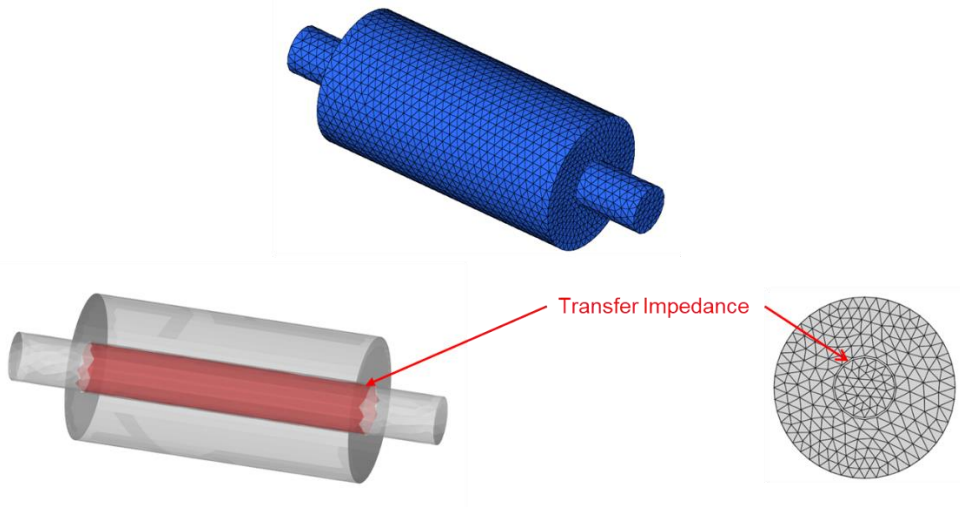

Figure 3.17 FEM simulation model.

The transmission loss results are shown in Figure 3.17. Observe that there is good agreement between measurement and simulation. A transmission loss exceeding 30 dB is considered very high for most applications. Notice that a 0.6 m length muffler performs very well.

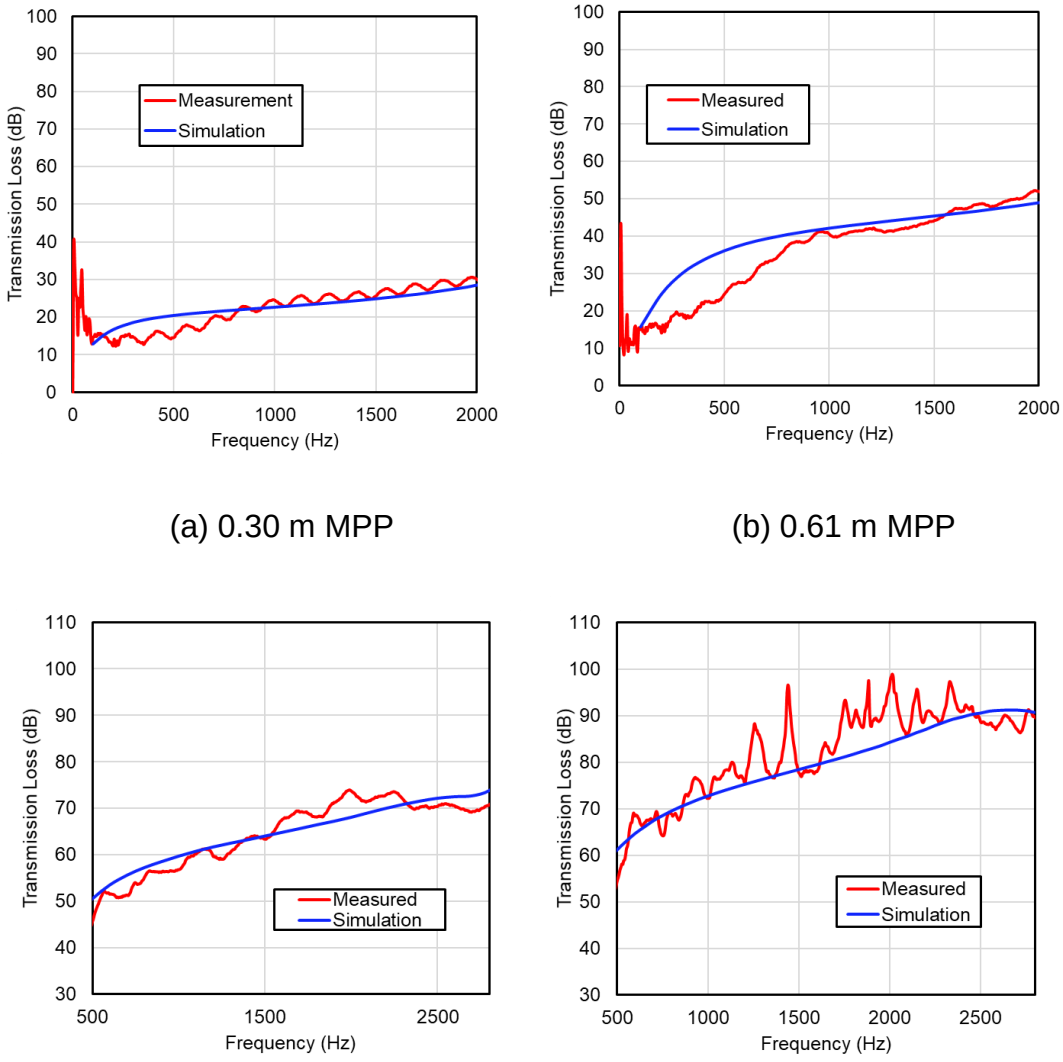

(a) 0.30 m MPP

(b) 0.61 m MPP

(c) 0.91 m MPP

(d) 1.22 m MPP

Figure 3.18 Comparison of measured and simulated transmission loss.

3.9 Summary

In this chapter, different MPP backings were utilized to improve the performance of the MPP absorber. The backing configurations included multiple channels, and Helmholtz resonators. The results demonstrated that the MPP sound absorptive performance could be improved significantly at lower

frequencies. Moreover, the broadband attenuation of the absorbers was also improved by introducing a three-channel or tapered partition.

Another variation considered was double leaf MPP absorber. In this case, a honeycomb partitioning is sandwiched between MPP on either side. The honeycomb serves to stiffen the panel and to insure that the sound absorber is locally reacting. It was demonstrated that the sound absorption was significantly improved at lower frequencies. Moreover, the sound absorption was broadband in frequency.

For both the special backing and double leaf cases, both the normal incident and diffuse field sound absorption was assessed. The normal incident sound absorption was measured in the impedance tube and measured results correlated well with simulation. The diffuse field sound absorption was measured in a small reverberation room. For each of the designed backings and for the double leaf MPP, the diffuse field sound absorption performance was demonstrated to be superior to that of a single leaf MPP with no backing.

The final MPP considered was an ultra-thin MPP. It was shown that the ultra-thin MPP could be used as a cover for sound absorptive material in mufflers and partial enclosures.

Chapter 4 ACOUSTICAL FABRICS

4.1 Introduction

In this chapter, the effective properties of acoustic fabrics are determined. Acoustic fabrics function similarly to microperforated panels. The research on microperforated panels is briefly reviewed and then the work on acoustic fabrics is considered in more depth. Similarities and differences between the characterization of microperforated panels and acoustic fabrics are noted.

Microperforated panel (MPP) absorbers are increasingly being used in the transportation industry in applications varying from aircraft, passenger trains, sea-going vessels, and luxury buses. They are durable, non-flammable, and do not disintegrate with time, but cost and installation effort are deterrents to more widespread usage. Nonetheless, second generation MPP absorbers are less expensive because they are manufactured by cutting or shearing slits into the panels instead of using lasers or drilling. The primary disadvantage of these absorbers is that sound absorptive properties are not easy to predict since perforations are no longer circular, differ in cross-section through the material, and often vary from perforation to perforation. In addition, the perforation rate is generally higher and hole diameter or size lower than first generation MPP absorbers. It will be shown in this paper that the equations to predict the sound absorption of MPP absorbers are especially prone to errors if the hole diameter is less than 0.5 mm.

The equations used to characterize MPP absorbers were developed by Maa (1975) several decades ago. Allam et al. (2009) formulated a more exact

expression that included the effect of grazing flow and high sound pressure level, but the equations are similar. In Maa's work, perforations were assumed to be uniform and circular. Allam et al. developed similar expressions for elliptical shaped slits (2009). In either case, the MPP is simulated as a transfer or series impedance where it is assumed that the particle velocity is the same on both sides of the panel. It is sufficient at this stage to note that transfer impedance has both real and imaginary components. In early research, Mechel (1988) had shown that the acoustic transfer impedance through a fibrous screen could be approximated as the flow resistance at low frequencies. This same assumption has been used in modeling acoustic fabrics.

Though the expressions developed cannot be directly applied to many commercial second-generation absorbers, Liu et al. (2014) showed that the models are still valid provided that an effective perforation rate and hole diameter are determined using a nonlinear least squares curve fit. They assumed that the thickness of the material was constant. It was shown that these effective parameters could be used for designing MPP absorbers as cavity depth was varied (2014). Moreover, the effect of dust contamination was considered, and it was determined that contamination mainly functioned to reduce the effective perforation rate.

There are many commercially available acoustic fabrics that behave similarly to MPP sound absorbers capitalizing on high acoustic resistance. The applications are different. Fabrics are normally used in architectural acoustics applications including lobbies, auditoria, and sports facilities. They are

aesthetically pleasing since they can be produced in many different colors and designs. Moreover, they are readily deployable, easily stowable, and ideal for non-permanent installations.

Introductory work on woven fabric sound absorption was performed by Shoshani and Rosenhouse (1990). Sound absorption was determined using the now antiquated standing wave method described in ASTM C384 (2016). Though the frequency resolution was limited, the authors performed valuable work noting that sound absorption was highest when the cavity depth was approximately $n\lambda/4$ where $n = 1,3,5,\ldots$ where λ is the acoustic wavelength. At these frequencies, particle velocity is high along with the accompanying energy dissipation in the material.

Kang and Fuchs (1999) recognized that the performance of a fabric is similar to an MPP sound absorber and used Maa's theory (1975, 1998) to characterize the fabric. They also understood that the low mass of the fabric may affect the performance. For most MPP sound absorbers, the panel is massive enough that panel motion can be neglected. Kang and Fuchs modeled the fabric as perforated holes that are in parallel with a limp mass. Using the electrical analogy, both the perforations and the mass were modeled as series or transfer impedances that are in parallel with one another. Measured sound absorption results compared reasonably well with predictions. Sound absorption was determined using a single microphone transfer function approach and results were presented in one-third octave bands.

Pieren (2012) also modeled fabrics with the impedances of perforations and limp mass in parallel with one another. Pieren (2012) assumed that the imaginary or reactive part of the transfer impedance for the perforations was negligible. Rather than predicting the perforation impedance, Pieren determined the fabric resistance by first measuring sound absorption and then using a curve fit so that predictions match the measurement. This approach is very similar to that used by Liu et al. (2014) for MPP absorbers with a few important differences. First, Liu et al. did not include the panel mass since the mass of typical MPP absorbers is much higher. Second, Pieren lumped the perforation impedance so that it was purely resistive whereas Liu et al. determined the effective hole diameter and perforation rate including the imaginary part of the transfer impedance from Maa's work. Pieren (2012) also predicted this lumped resistance using the inter-yarn porosity and approximate dimensions of the open pores. The estimated pore diameters were between 0.072 and 0.137 mm. Perforation rates ranged from 1.4% to 38 %. It will be shown later in the paper that Maa's equation is highly sensitive to pore diameter when then pore diameter is less than 0.5 mm.

Pieren et al. (2015) used a similar fabric characterization approach to predict the diffuse field sound absorption for folded textile curtains. The results obtained were usable for architectural acoustics applications. Pieren and Heutschi (2015) developed an improved model which considered both the intra-yarn and inter-yarn airflow resistance of lightweight resistive curtains as well as the vibration of the fabric itself. Geometric parameters of the fabric were extracted from photographs and the acoustic transfer impedance of fabric determined. Acoustic

and mechanical transfer impedances were again considered to be in parallel with one another. The normal incident and diffuse field sound absorption was predicted for single- and double-layer arrangements. Predictions agreed well with measurements.

Tang et al. (2018) used Pieren's original approach (2012) to predict the sound absorption of corduroy fabrics. There was acceptable correlation with measurement at higher frequencies though there were discrepancies at low frequencies. This may be a result of the complexity of the textile. Tang et al. (2018) also investigated dipping the fabric to make it more massive. Li et al. (2016) simulated similar microperforated membranes and improved the method by enforcing continuity between the velocity of the membrane and acoustic velocity on the hole periphery.

In perhaps the most sophisticated approach, Ruiz et al. (2012) used a simplified form of Johnson-Champoux-Allard (JCA) theory to model a woven mesh where the thermal and viscous characteristic lengths were calculated based on an elementary cell of the fabric mesh. In this work, the fabric was fronted with a perforated plate and the combined impedance of the plate and mesh was determined. Wave propagation through the fabric itself was considered, so the fabric was no longer modeled as a transfer impedance.

Prasetiyo et al. (2018) similarly used JCA theory to determine the sound absorption. Interestingly, they also used a Delaney and Bazley (1970) type empirical model and used empirically determined constants for three different fabrics. Predictions were better using the empirical model but that is not surprising

since measurements are used to resolve the constants. Though not quite as accurate, the JCA model sans empirical constants are still acceptable and may be used to assess how varying fabric properties affects impedance and sound absorption. It is worthy of note that the authors recognized that varying pore size is unavoidable in fabrics and this would seem to be the main weakness. Hence, absorptive properties can be developed very accurately for a single cell of material, but that cell may not be representative of the material as a whole. Prasetiyo et al. (2018) then determined the sound absorption of double layer fabric sound absorbers. There was some deviation between the predicted and measured sound absorption, but results were quite satisfactory for engineering purposes. Cai et al. (2019) used a similar approach but determined JCA parameters using a finite element method.

In summary, many different modeling approaches have been used to characterize fabrics though JCA theory has been used in the more recent studies. The current research characterizes fabrics by using a curve fitting procedure similar to Pieren's (2012) original work to determine the transfer impedance of the perforations. However, the procedure suggested by Liu et al. (2014) is used so that both the perforation rate and hole diameter are determined rather than using a lumped resistance. The reactive component of the transfer impedance is now included. Moreover, the real and imaginary parts of the transfer impedance are compared to measurement which was not performed in the prior work by Pieren (2012), and the predicted transfer impedance is then used to determine the sound

absorption of multi-layer sound absorbers and the transmission loss through the fabric.

There are some important differences between the current work and the earlier work by Pieren (2012) and Pieren and Heutschi (2015). These include:

1. The reactive part of Maa's equation is included.
2. The curve fit is used to determine an effective porosity and effective hole diameter for the fabric rather than assuming the acoustic resistance is roughly equivalent to the airflow resistance or an effective resistance.
3. The real and imaginary parts of the transfer impedance are predicted using the effective parameters and are compared to direct measurement. This check was not performed in previous work.
4. Transfer matrix theory is then used to predict the sound absorption of the fabric for different cavity depths and the transmission loss for multiple layers.
5. The fabric is utilized in a partial enclosure to demonstrate its effectiveness.

A sensitivity analysis is performed first to better understand the effect of hole diameter, perforation rate, thickness, and fabric (or panel) mass variations on predictions. The sensitivity analysis will prove integral to many of the later conclusions in the paper.

4.2 Determination of Transfer Impedance

In most prior work, acoustic fabrics were modeled as a transfer impedance which is defined as the acoustic pressure difference divided by the particle velocity.

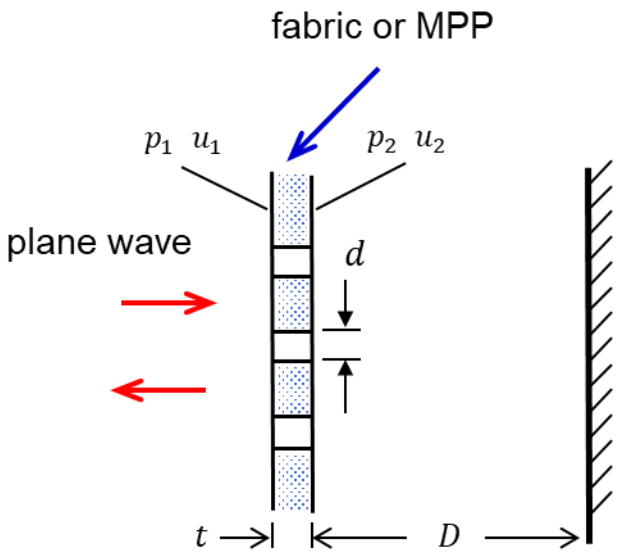

Figure 4.1 Schematic of a fabric layer.

Figure 4.1 shows a schematic of a fabric layer. If the fabric layer is thin, particle velocity is assumed to be the same on both sides of the fabric ($u = u_1 = u_2$). The normalized transfer impedance can be expressed as

$$z_{tr} = \frac{p_1 - p_2}{\rho c u} \tag{4.1}$$

where p_1 and p_2 are the respective acoustic pressures on opposing sides of the fabric, u is the particle velocity, and ρc is the characteristic impedance of air. The transfer impedance can be measured by using an impedance difference method (Wu, 2003). Impedance is measured in an impedance tube at the sample position without and with the sample in place. The difference between the two measurements corresponds to the transfer impedance. From the University of Kentucky acoustic lab's experience, it is preferable to use a sound absorbing termination when making the measurements to mitigate deleterious effects due to tube resonances.

A schematic of a fabric or perforate sample is shown in Figure 4.1 and important variables are identified. Maa's (1975, 1998) foundational work on MPP sound absorbers is well-known and will only be briefly reviewed here. The normalized transfer impedance for circular perforations (z_{perf}), can be expressed as

$$z_{perf} = \frac{32\eta t}{\sigma \rho c d^2}\left(\sqrt{1+\frac{\beta^2}{32}}+\frac{\sqrt{2}}{32}\frac{\beta d}{t}\right) + \frac{j\omega t}{\sigma c}\left(1+\frac{1}{\sqrt{9+\frac{\beta^2}{2}}}+\frac{0.85d}{t}\right) \tag{4.2}$$

where t is the thickness of the MPP, σ is the porosity (typically under 5%), ρ is the density of air, c is the speed of sound, d is the perforated hole diameter, ω is the angular frequency, and

$$\beta = d\sqrt{\rho\omega/4\eta} \tag{4.3}$$

is the perforate constant. η is the dynamic viscosity. In the case of noncircular perforations, Maa (2006) provided a correction to the above equation.

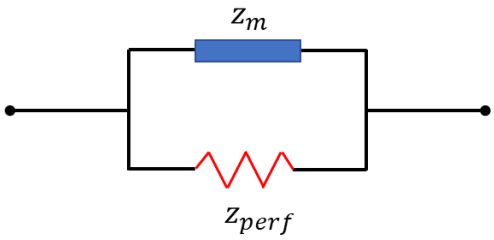

Figure 4.2 Equivalent electrical circuit.

If the mass of fabric is considered, the series impedances of the perforations given in Equation (4.2) and the mass reactance are in parallel (Mechel, 1998, Sakagami et al., 1998). Hence, the normalized transfer impedance for the fabric can be expressed as

$$z_{tr} = \frac{z_{perf} z_m}{z_{perf} + z_m} \tag{4.4}$$

where $z_m = j\omega m_s/(\rho c)$ (Pieren, 2012, Allard, 2009, Atalla, 2007) is the normalized mass reactance and m_s is the mass per unit area. For MPP, $z_m \gg z_{perf}$ and so the transfer impedance reduces to $z_{tr} = z_{perf}$. However, this assumption would appear invalid for a fabric.

The fabric and back cavity may be considered as an absorbing system, and the normalized surface impedance of the combination fabric-cavity absorber system may be expressed as

$$\mathrm{Z} = z_{tr} - j \cot\left(\frac{\omega D}{c}\right) \tag{4.5}$$

where D is the empty cavity depth behind the MPP. Once the surface impedance (Z) is determined, the normal incident absorption coefficient can be expressed as

$$\alpha = \frac{4Z_R}{(1 + Z_R)^2 + Z_I^2} \tag{4.6}$$

where Z_R and Z_I are the real and imaginary parts of the normalized surface impedance (Z) in Equation (4.5).

Liu et al. (2014) measured the sound absorption of a microperforated panel with backing cavity in an impedance tube. They then applied Eqns. (4.2) to (4.5) and used a least squares curve fit to determine an effective hole diameter and

porosity that best compared with measurement. The same procedure is applied in this paper to determine effective parameters.

Once a sound absorptive layer is characterized via z_{tr}, the sound absorption of multiple layers is easily determined using the transfer matrix theory of Munjal (2014). The transfer matrix for a fabric can be expressed as

$$[T] = \begin{bmatrix} 1 & \rho c/S z_{tr} \\ 0 & 1 \end{bmatrix} \tag{4.7}$$

Likewise, the transfer matrix for an air cavity of length D is expressed as

$$[T] = \begin{bmatrix} \cos(kD) & j\rho c/S \sin(kD) \\ jS \sin(kD)/\rho c & \cos(kD) \end{bmatrix} \tag{4.8}$$

where k is the acoustic wavenumber, and S is the cross-sectional area. The transfer matrix for a cascade of fabric layers and cavities in series can be expressed as

$$\begin{bmatrix} T_{11} & T_{12} \\ T_{21} & T_{22} \end{bmatrix} = [T_1][T_2] \dots [T_N] \tag{4.9}$$

The transfer matrix can then be used to identify both the sound absorption and the transmission loss. The surface impedance of the absorptive system can be expressed as

$$z = \frac{T_{11}}{T_{21}} \tag{4.10}$$

where T_{11} and T_{21} are elements of the transfer matrix product from Equation (4.9). The sound absorption can then be determined using Equation (4.6), and the transmission loss (TL) can be determined via

$$TL = 10 \log_{10} \left(\frac{1}{4} \left| T_{11} + \frac{T_{12}}{\rho c} S + \rho c/S \, T_{21} + T_{22} \right|^2 \right) \tag{4.11}$$

4.3 Sensitivity Analysis for Sound Absorption

The sound absorptive properties of an acoustic fabric depend on the hole diameter d, perforation rate σ, thickness t and the mass m. The sensitivity of the sound absorption to each of these variables is studied.

There has been little prior research on performing sensitivity analyses on acoustic fabrics or for that matter MPP. In helpful work, Laly et al. (2019) performed a global sensitivity analysis (Sobol, 2001) investigating the sensitivity of impedance and sound absorption to variations in MPP parameters. Parameters investigated included the perforation rate, hole diameter, thickness, cavity depth D, and sound pressure level. The resulting sensitivities depended greatly on the assumed minimum and maximum values for the input parameters. Laly et al. (2019) was especially interested in MPP absorbers for aerospace applications. Hence, the need to also include the effect of high sound pressure levels. Accordingly, Laly et al. considered parameter ranges in line with aerospace applications. The percent open area was centered at 5% and the hole diameter at 1 mm. Parameter ranges were relatively narrow for the first two sensitivity studies. The ranges were extended later to 1-8% for the open area and 0.2 to 2 mm for hole diameter. Laly et al. demonstrated that the perforation rate drove the performance at high sound pressure levels.

A similar investigation for fabric and MPP absorbers is performed in this paper. The resulting study complements the work performed by Laly et al. (2019), but there are several important differences since the intent of this study is different.

The current study is focused on MPP absorbers for standard industrial applications. Hence, sound pressure levels are assumed to be under 100 dB so there is no need to include nonlinear effects. Moreover, commercial fabrics and inexpensive MPP absorbers often have slits or perforations that are less than 0.5 mm in diameter and so this investigation focuses on smaller hole diameters. Finally, the reported sensitivity results serve to better explain the later findings in the paper. Since the purpose of the analysis is limited, a much simpler local sensitivity analysis is performed.

The normalized local sensitivity (Saltelli et al., 2008) of the sound absorption to a parameter x is defined as

$$S_x = \frac{x}{\alpha}\frac{D(\alpha)}{D(x)} \tag{4.12}$$

where S_x is the sensitivity. The normalized sensitivity can be considered as the instantaneous ratio of relative change in sound absorption ($\Delta\alpha/\alpha$) to the relative change in the parameter ($\Delta x/x$). Hence, x/α serves as a normalization factor in Equation (4.12). Though there are many different options for sensitivity analyses, the simple approach adopted here is used for ease of understanding.

The baseline parameters used in the analysis are a hole diameter (d) of 0.40 mm, perforation rate (σ) of 4%, thickness (t) of 1 mm, and surface mass density (m_s) of 3.2 kg/m^2. Cavity depth is held constant at 0.10 m. The MPP used in this test has 50 holes. These parameters approximate the effective parameters for industrial use MPP absorbers and acoustic fabrics. Table 4.1 shows the sets of parameters used for local sensitivity calculations.

Table 4.1 Parameters for sensitivity analyses

	Hole diameter (mm)	Thickness (mm)	Porosity (%)	Surface Mass Density (kg/m^2)
Group 1	0.20	1.00	4.00	3.20
Group 2	0.40	1.00	4.00	3.20
Group 3	0.80	1.00	4.00	3.20
Group 4	1.00	1.00	4.00	3.20
Group 5	0.40	1.00	1.00	3.20
Group 6	0.40	1.00	2.00	3.20
Group 7	0.40	1.00	8.00	3.20
Group 8	0.40	0.50	4.00	3.20
Group 9	0.40	1.00	4.00	0.20
Group 10	0.40	1.00	4.00	0.40

Hole diameters are varied between 0.2 mm to 1.0 mm. A perforation rate of 0.04, thickness of 1 mm, is assumed. These parameters remain constant as the other parameters are varied.

Figure 4.3 (a) and Figure 4.3 (b) show the normalized local sensitivity to the hole diameter (S_d) and the sound absorption, respectively, for different values of the hole diameter. The sound absorption is plotted on a logarithmic scale to

facilitate understanding of the normalized local sensitivities. Observe that the expected amount of change in sound absorption is generally on the same order as the relative change in hole diameter except between 400 and 1000 Hz if the hole diameter is small (for example at 0.20 mm).

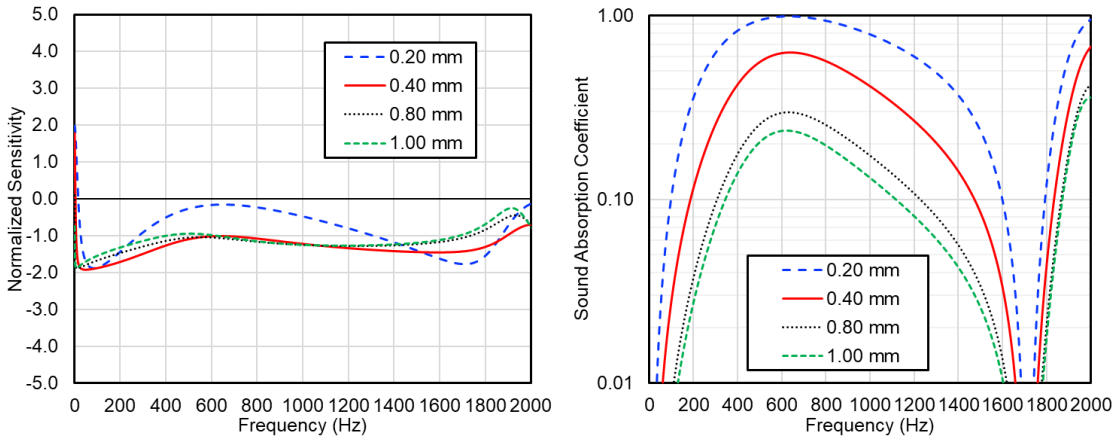

(a) (b)

Figure 4.3 (a) Normalized local sensitivity to hole diameter (S_d), (b) sound absorption coefficient.

In most acoustic fabrics and second generation MPP absorbers, the openings in the material are neither perfectly circular nor smooth edged. Moreover, the hole diameter often varies over the parameter itself. If hole diameters are between 0.20 mm and 0.40 mm, it is anticipated that estimates of the hole diameter based on visual methods may be in error up to 50% or greater. Consequently, estimates of the sound absorption using Maa's methods are likely to have large errors as well. Such errors may have little practical consequence at frequencies where the sound absorption is low, but such errors will have impact in frequency ranges where the sound absorption is changing rapidly. As an aside, it is not uncommon to see comparisons between measurement and analysis that exhibit

noticeable discrepancies. The large sensitivity to hole diameter is one likely reason.

Figure 4.4 (a) shows the normalized local sensitivity to the perforation rate (S_σ). Figure 4.4 (b) shows the corresponding sound absorption for perforation rates of 1%, 2%, 4%, and 8%. The hole diameter is assumed to be 0.4 mm with a thickness of 1 mm and surface mass density of 3.2 kg/m^2. At most frequencies, the normalized local sensitivity is less than for hole diameter, but the sensitivity level is still significant. Percentage errors are anticipated to be higher if the perforation rate is low, and normalized local sensitivity is on the order of 0.5 from 600 to 1200 Hz.

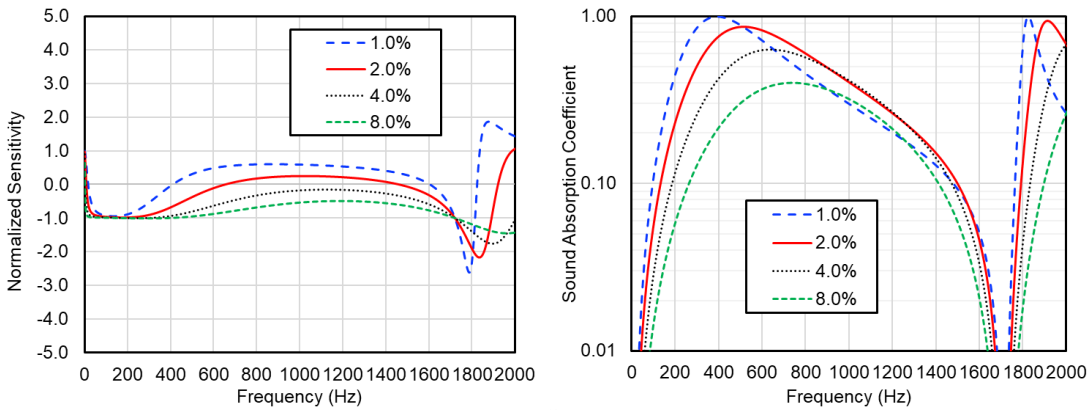

(a) (b)

Figure 4.4 (a) Normalized local sensitivity to the perforation rate (S_σ), (b) sound absorption coefficient.

However, it is important to recognize that perforation rate is frequently estimated by multiplying the number of holes by the surface area of each hole and then dividing by the total area of the perforated plate. It follows that the perforation rate estimate is also dependent on the hole diameter. Assuming this to be the

case, the normalized local sensitivity can be calculated based on the hole diameter with perforation rate also a function of the hole diameter. The thickness is assumed to be 1 mm and surface mass density of 3.2 kg/m^2. The number of holes is assumed to be 51995 per square meter.

The normalized local sensitivity is shown in Figure 4.5 (a) with the corresponding sound absorption in Figure 4.5 (b). It can be concluded that errors in the calculated sound absorption are anticipated to be on the order of 1 or 2 times the corresponding errors in hole diameter for small hole diameters (i.e., 0.20 mm). For larger hole diameters, errors are anticipated to be from 2 to 4 times the error in hole diameter. The variation in sound absorption in Figure 4.5 (b) also lends credence to these results. The results suggest that a determination of effective parameters through measurement of the sound absorption is justifiable since estimates of the hole diameter on a manufactured panel are prone to error.

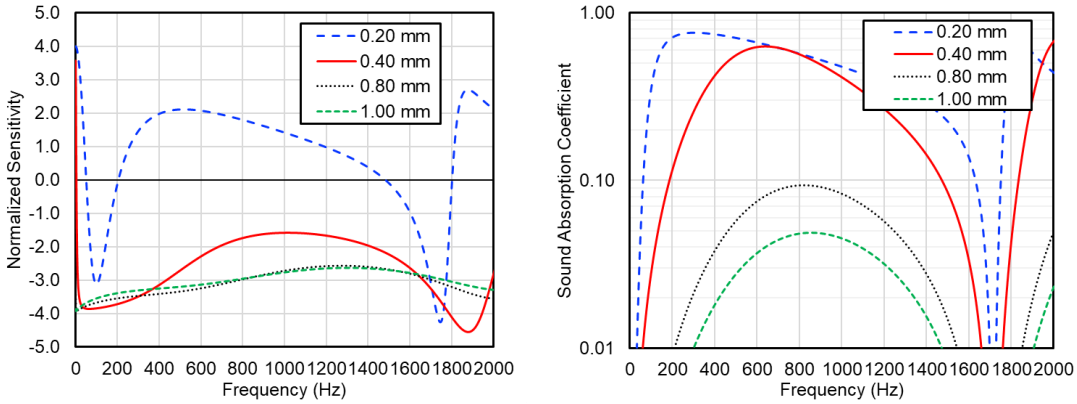

(a) (b)

Figure 4.5 (a) Normalized local sensitivity to (S_d), (b) sound absorption coefficient.

Figure 4.6 (a) shows the normalized local sensitivity to the thickness (S_t). The corresponding curves for the sound absorption are shown in Figure 4.6 (b).

The hole diameter is 0.40 mm, perforation rate is 4%, and mass density is 3.2 kg/m^2. The relative error resulting from discrepancies in panel thickness is lower than for hole diameter and perforation rate. Errors are higher at frequency ranges where the sound absorption is low, but this is likely less of a concern for designers.

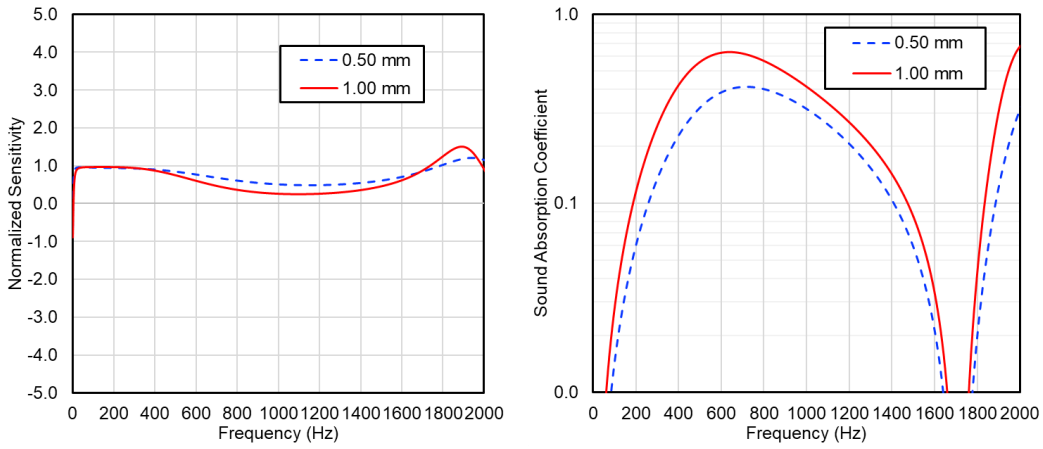

(a) (b)

Figure 4.6 (a) Normalized local sensitivity to the thickness (S_t), (b) sound absorption coefficient.

Figure 4.7 (a) shows the normalized local sensitivity (S_{m_s}) to the surface mass density (m_s) of the panel. The hole diameter is 0.4 mm, perforation rate is 4% and thickness is 1 mm. Surface mass densities of 0.2 kg/m^2, 0.4 kg/m^2, and 3.2 kg/m^2 are considered. The higher surface mass density (3.2 kg/m^2) is typical of most microperforated panel absorbers. It can be observed that the surface mass density is unimportant if it is sufficiently high. At lower surface mass densities of 0.2 kg/m^2 and 0.4 kg/m^2, errors in the surface mass density will have some effect but these are not nearly as significant as those for hole diameter.

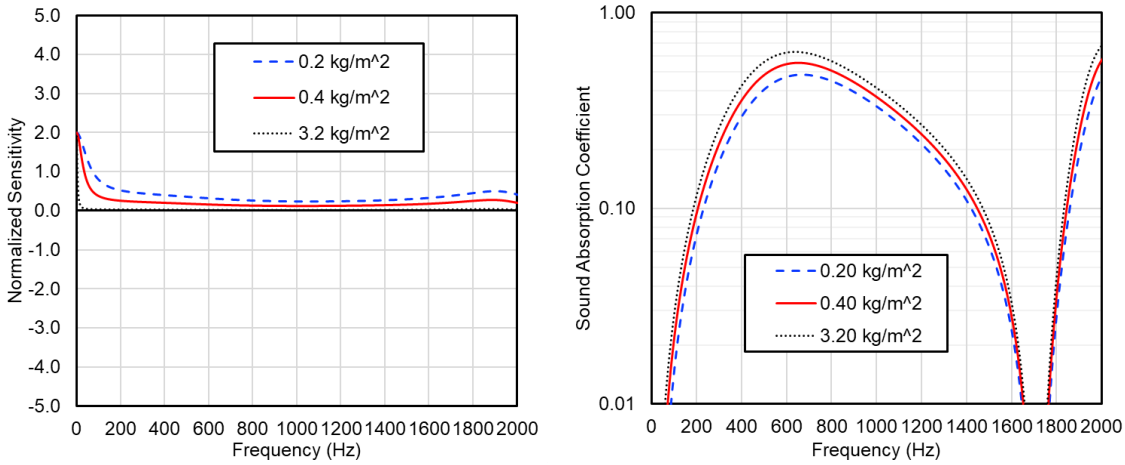

(a) (b)

Figure 4.7 (a) Normalized local sensitivity to the thickness (S_t), (b) sound absorption coefficient.

4.4 Sensitivity Analysis for Transmission Loss

A similar study was performed to investigate the effect of the input parameters on transmission loss. The geometric parameters considered were the same: hole diameter, perforation rate, thickness, and mass density. The geometric and material parameter values are summarized in Table 4.1.

Figure 4.8 (a) shows the normalized local sensitivity due to changing hole diameter for hole diameters of 0.20 mm, 0.40 mm, 0.80 mm, and 1.00 mm. The perforation rate is assumed to be 4%, thickness is 1 mm, and the surface mass density is 3.2 kg/m^2. Figure 4.8 (b) shows the transmission loss for the corresponding hole diameters considered. The transmission loss is sensitive to hole diameter variations if the hole diameter is small. Moreover, the sensitivity is relatively constant with frequency.

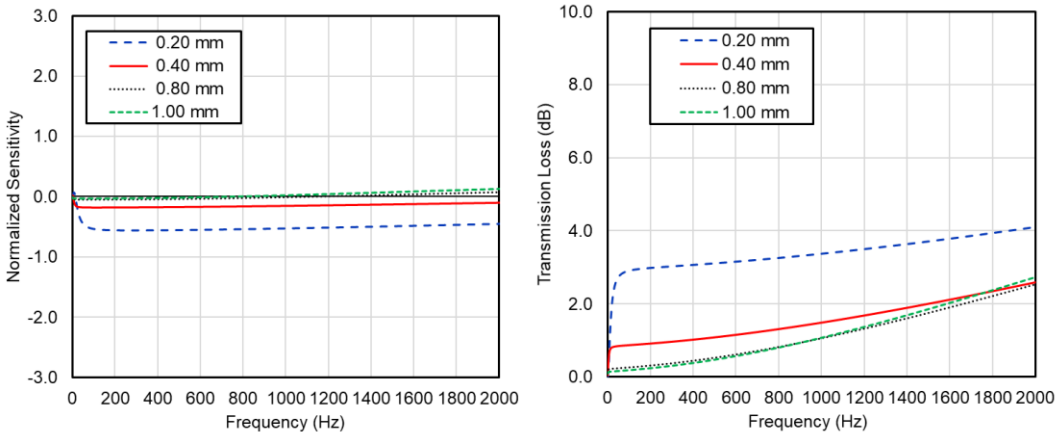

(a) (b)

Figure 4.8 (a) Normalized local sensitivity to diameter, (b) transmission loss.

Figure 4.9 (a) shows normalized local sensitivity due to varying the perforation rate for perforation rates of 1%, 2%, 4%, and 8%. The hole diameter is assumed to be 0.40 mm, and thickness and surface mass density are 1.0 mm and 3.2 kg/m^2. Observe that the sensitivity to perforation rate increases with frequency. The normalized sensitivity is higher for lower perforation rates. The transmission loss is plotted in Figure 4.9 (b) where the transmission loss is significantly higher at low perforation rates of 1% and 2%.

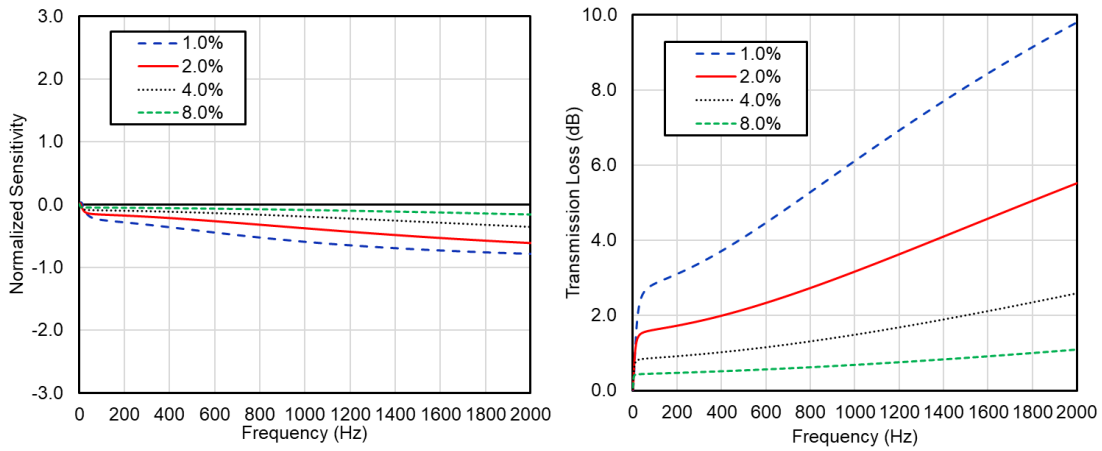

(a) (b)

Figure 4.9 (a) Normalized local sensitivity to perforation, (b) transmission loss.

As noted in the prior section, the perforation rate is often estimated from the assumed hole diameter and the number of perforations over a given area. If the perforation rate is assumed to be a function of the hole diameter, the normalized local sensitivity due to varying the hole diameter is shown in Figure 4.10 (a). The corresponding values of transmission loss are indicated in Figure 4.10 (b). Results are shown assuming that the thickness is 1.0 mm and the surface mass density is 3.2 kg/m^2. The amplitude of the normalized sensitivity is high for hole diameters of 0.20 mm and 0.40 mm. The sensitivity is low if the hole diameter is or exceeds 0.8 mm.

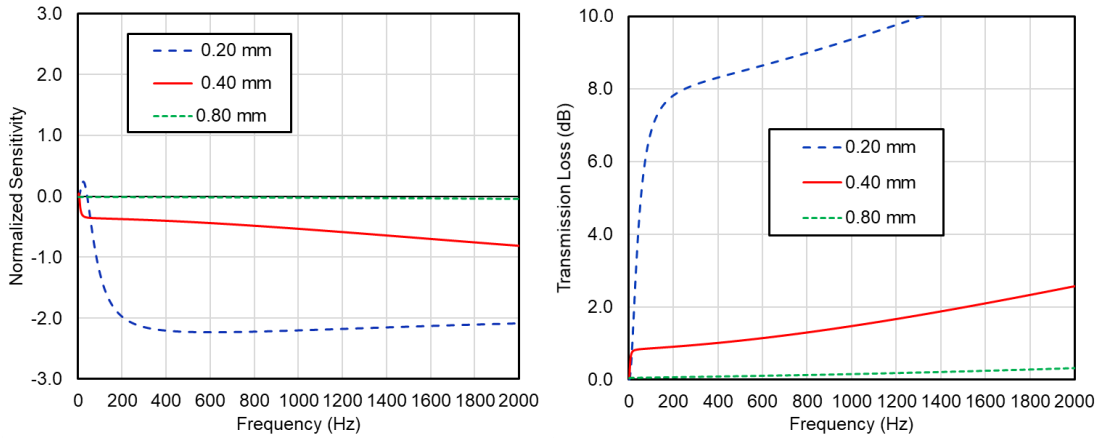

(a) (b)

Figure 4.10 (a) Normalized local sensitivity to perforation, (b) transmission loss.

Figure 4.11 (a) shows the normalized local sensitivity of transmission loss to variations in thickness along with a corresponding transmission loss plot for thicknesses of 0.50 mm and 1.00 mm. Figure 4.12 (a) shows the normalized local sensitivity to changes in surface mass density. The transmission loss is shown in Figure 4.12 (b) for surface mass densities of 0.2 kg/m^2 and 3.2 kg/m^2. The transmission loss is not overly sensitive to small changes in thickness or surface mass density. This is the case for even low values of both thickness and surface mass density.

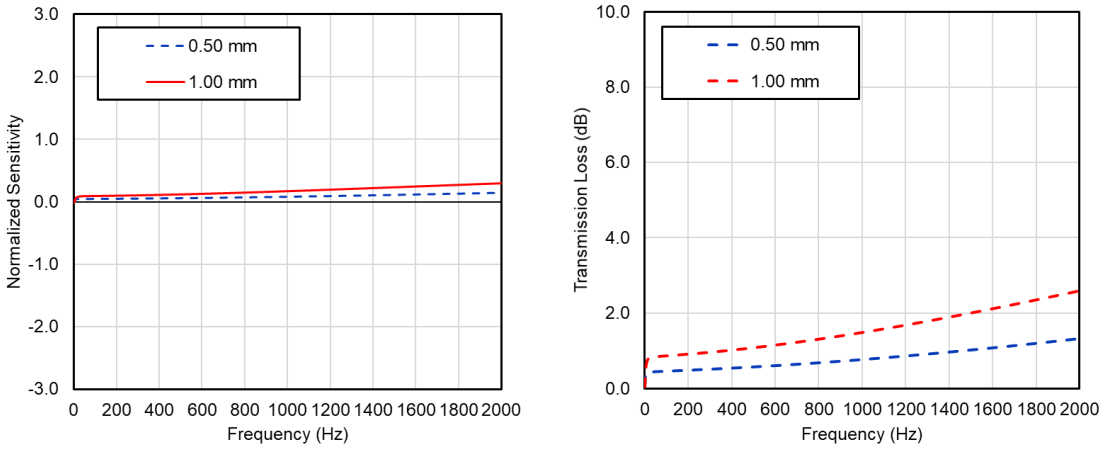

(a) (b)

Figure 4.11 (a) Normalized local sensitivity to thickness, (b) transmission loss.

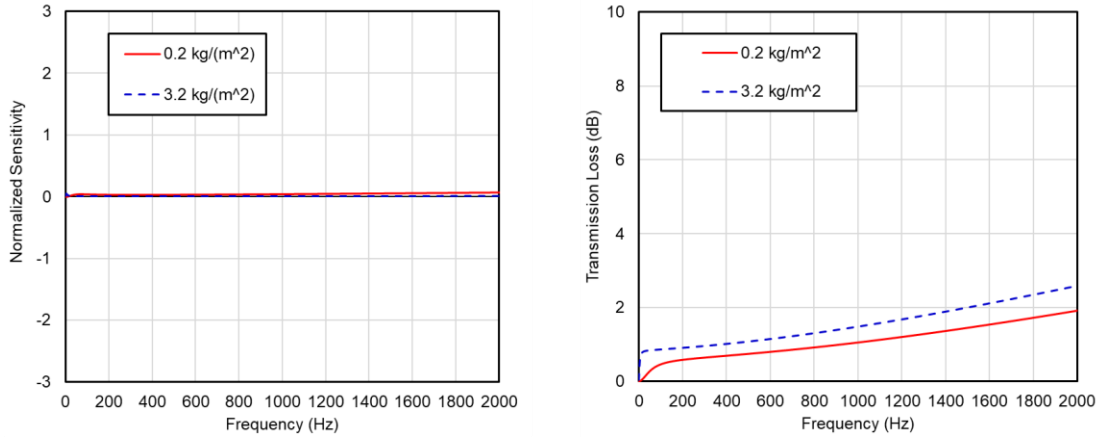

(a) (b)

Figure 4.12 (a) Normalized local sensitivity to surface mass density, (b) transmission loss.

It can be concluded that the transmission loss is very sensitive to changes in the hole diameter and perforation rate. Moreover, transmission loss is likely to be greatly in error if the perforation rate is estimated from the hole diameter.

4.5 Impedance Tube Test Cases for Single Layer Fabrics

The four samples tested are shown in Figure 4.13. The first two fabrics (A and B) are impermeable aside from the small perforations. They are glass fabrics that are laminated with a vinyl film on both sides. A hot needle process is then used to make the perforations. The other two fabrics (C and D) are woven. The tested samples are mounted in rings that are sized to the outer diameter of two separate impedance tubes. The impedance tube diameters are 34.9 mm and 98.4 mm respectively. By comparing the results using a smaller and larger tube, the effect of the sample holder on the measurement can be established. The cavity depth behind the fabric was set to 10 cm regardless of the impedance tube used and the frequency step for the measurements is 4 Hz. The sound absorption is measured according to ISO 10534-2 (1998).

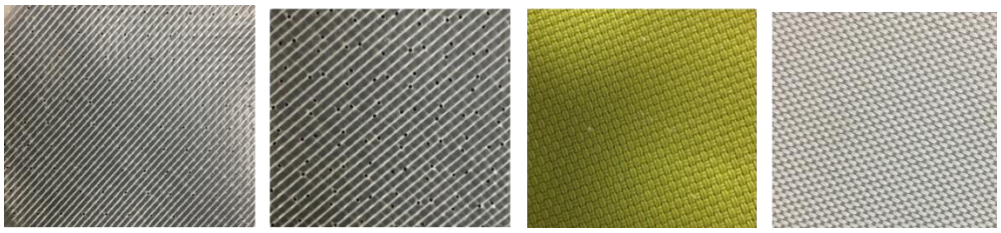

Figure 4.13 Single layer fabrics A, B, C, and D.

The sound absorption results between 200 and 1000 Hz were used for the 98.4 mm diameter sample and between 200 and 3000 Hz for the 34.9 mm diameter sample. A curve fit was then used to determine the effective parameters for each fabric. Tests were performed without and with the fabric mass accounted for. The curve fits are compared to direct measurement of the sound absorption in Figure 4.14 and Figure 4.15 for the 34.9 mm and 98.4 mm impedance tubes, respectively.

Observe that the curve fits compare well with the sound absorption at most frequencies. From Figure 4.15, note that differences do arise when the sound absorption is low where it is likely that damping mechanisms other than viscous friction in the perforations contribute more to the sound absorption. Moreover, observe that an adequate curve fit can be determined whether the mass effect is included or not. This does not mean that the effect of mass is unimportant. Rather, it means that the effect of mass can be incorporated into the effective hole diameter and perforation rate so that the curve fit is acceptable at most frequencies.

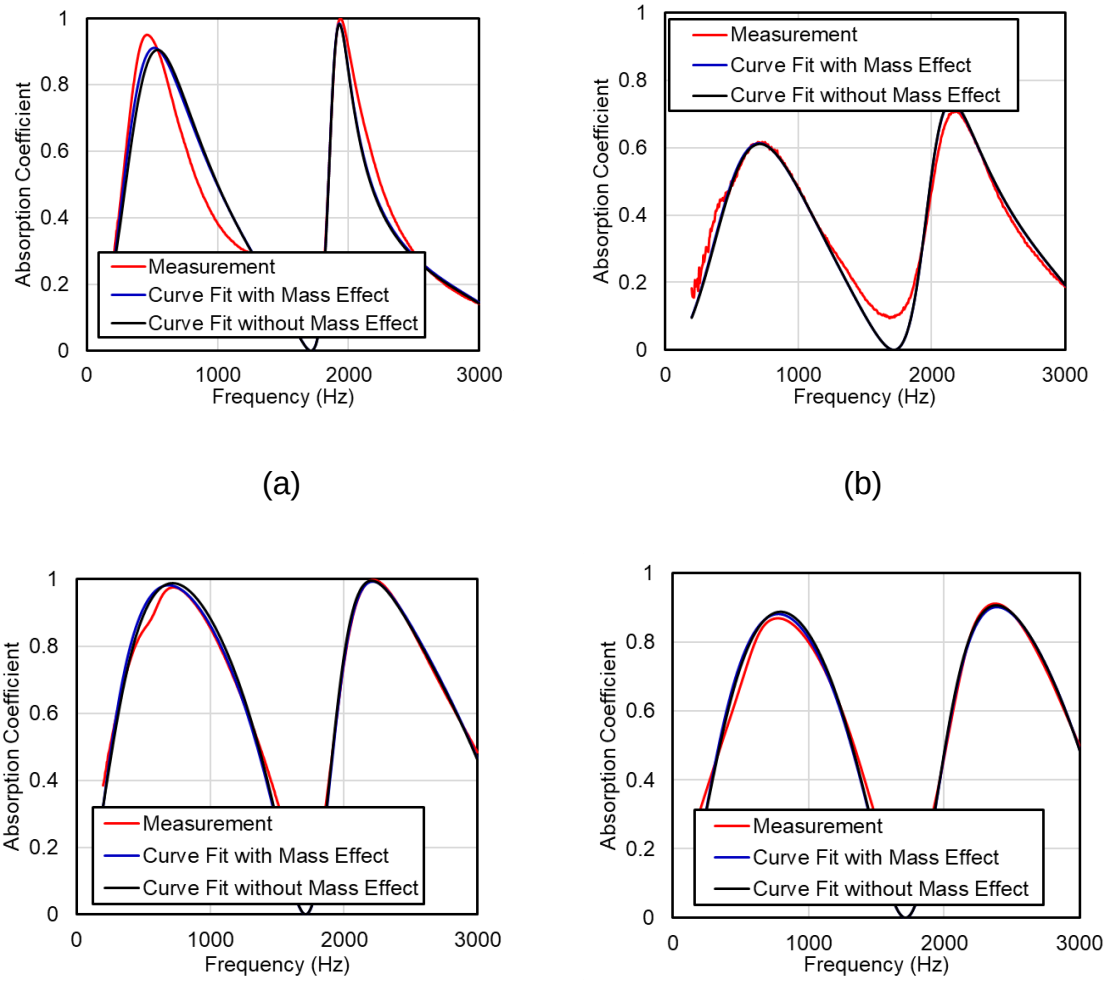

Figure 4.14 Comparison of curve fit and direct measurement of sound absorption in the 34.9 mm impedance tube.

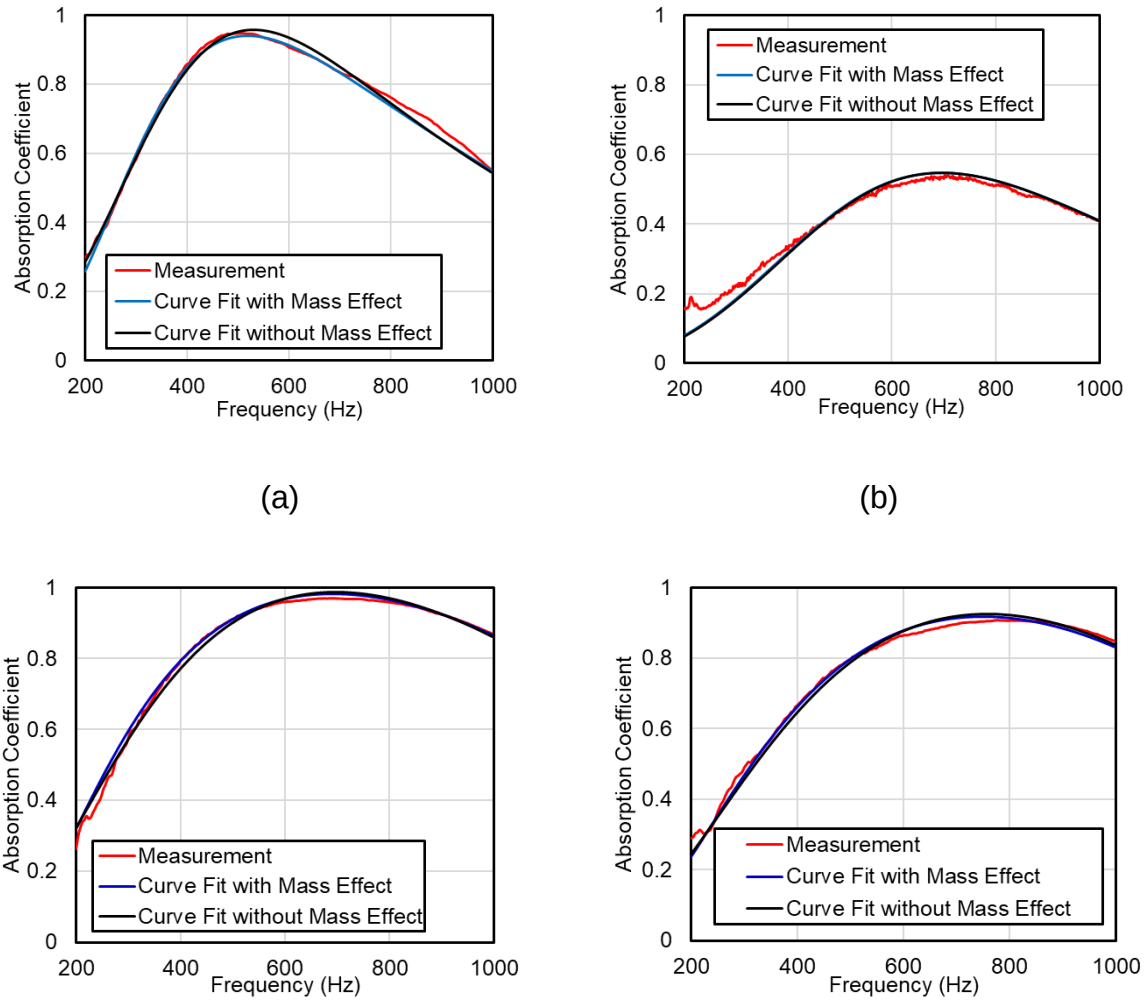

Figure 4.15 Comparison of curve fit and direct measurement of sound absorption in the 98.4 mm impedance tube, (a) Fabric A, (b) Fabric B, (c) Fabric C, (d) Fabric D.

One way to gage whether the effective parameters are reasonable is to then use them to predict the sound absorption with the backing cavity depth changed. The sound absorption for smaller cavity depths of 4 cm and 7.5 cm were measured. The predicted sound absorption using the effective parameters is compared in Figure 4.16 (a) and (b) for Fabrics A and C, respectively. The effective parameters

were determined using the 98.4 mm diameter impedance tube. It can be observed that predictions are acceptable over the entire frequency range. One advantage of using the effective parameters is that the measurement noise at the low frequencies is removed.

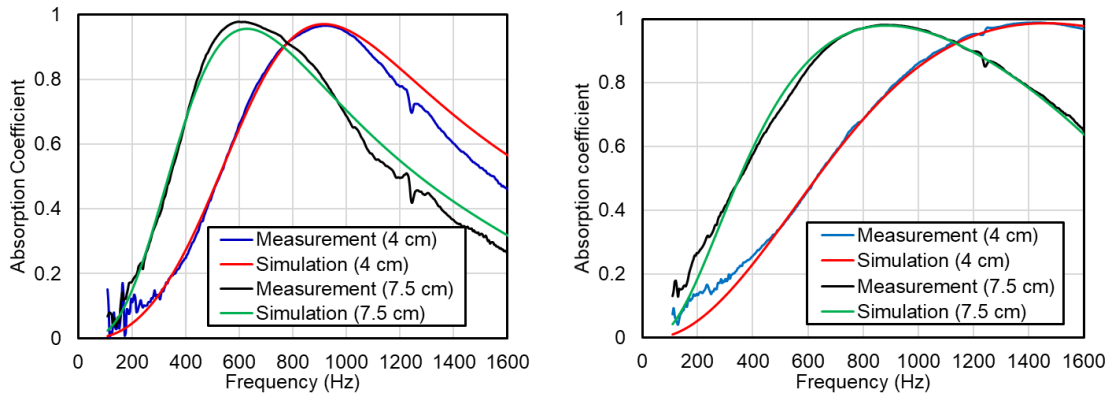

(a) (b)

Figure 4.16 Comparison of prediction using effective parameters and direct measurement of sound absorption for Fabric A and Fabric C in the 98.4 mm impedance tube.

Results were very similar if the mass effect was not included when determining the effective parameters. Table 4.2 and

Table 4.3 compare the effective parameters determined using the 98.4 mm and 34.9 mm impedance tubes with and without the mass effect included, respectively. Though results are similar for both impedance tubes, the differences between the effective parameters are not negligible since the equations are sensitive to the effective hole diameter which are generally below 0.4 mm.

Table 4.2 Effective parameters comparison between 98.4 mm and 34.9 mm diameter impedance tubes if mass effect is included.

	Thickness (mm)	Effective Hole Diameter (mm)		Effective Perforation Rate (%)		Surface Mass Density (kg/m^2)
		98.4 mm Tube	34.9 mm Tube	98.4 mm Tube	34.9 mm Tube	
Fabric A	0.33	0.26	0.29	0.84	0.79	0.38
Fabric B	0.33	0.38	0.32	2.30	2.45	0.38
Fabric C	0.70	0.15	0.15	5.29	5.54	0.59
Fabric D	0.70	0.14	0.12	8.85	12.78	0.45

Table 4.3 Effective parameters comparison between 98.4 mm and 34.9 mm diameter impedance tubes if mass effect is not included.

	Thickness (mm)	Effective Hole Diameter (mm)		Effective Perforation Rate (%)	
		98.4 mm Tube	34.9 mm Tube	98.4 mm Tube	34.9 mm Tube
Fabric A	0.33	0.32	0.36	0.96	1.05
Fabric B	0.33	0.42	0.34	2.55	2.70
Fabric C	0.70	0.17	0.15	4.38	5.29
Fabric D	0.70	0.15	0.13	7.41	12.12

The fitted results from the larger 98.4 mm diameter impedance tube can then be used to predict the sound absorption over a larger frequency range and

compared to direct measurement in the 34.9 mm tube. Figure 4.17 (a) and Figure 4.17 (b) compare the fitted predictions to direct measurement in the 34.9 mm tube for Fabrics C and D. As would be expected, the sound absorption predictions using the curve fit from the 98.4 mm compare well to the directly measured sound absorption.

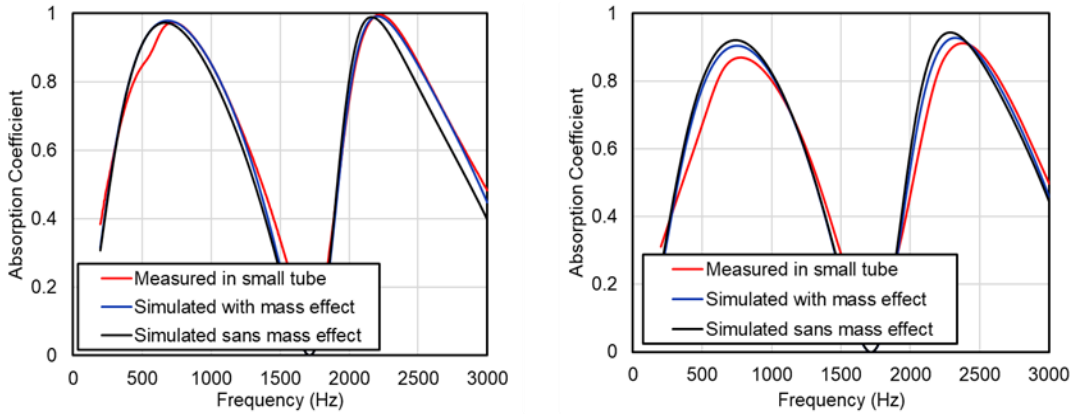

(a) (b)

Figure 4.17 Comparison of prediction using effective parameters and direct measurement of sound absorption for Fabric C and Fabric D in the 34.9 mm impedance tube.

One other important check is to compare the real and imaginary parts of the transfer impedance. The transfer impedance is more fundamental than the sound absorption and is used in most analysis models. The fitted real and imaginary parts of the transfer impedance are compared to direct measurement in Figure 4.18. The fitted values of the transfer impedance compare favorably with direct measurement regardless of whether the fabric mass is included in the curve fit or not. To our knowledge, the transfer impedance has not been compared to direct measurement in prior fabric studies. Though the results are not conclusive, the results suggest

that the effect of mass can be excluded in the curve fit. This conclusion is counter to what Pieren and Heutschi (2015) concluded. However, they neglected the imaginary part of the transfer impedance in Equation (4.2).

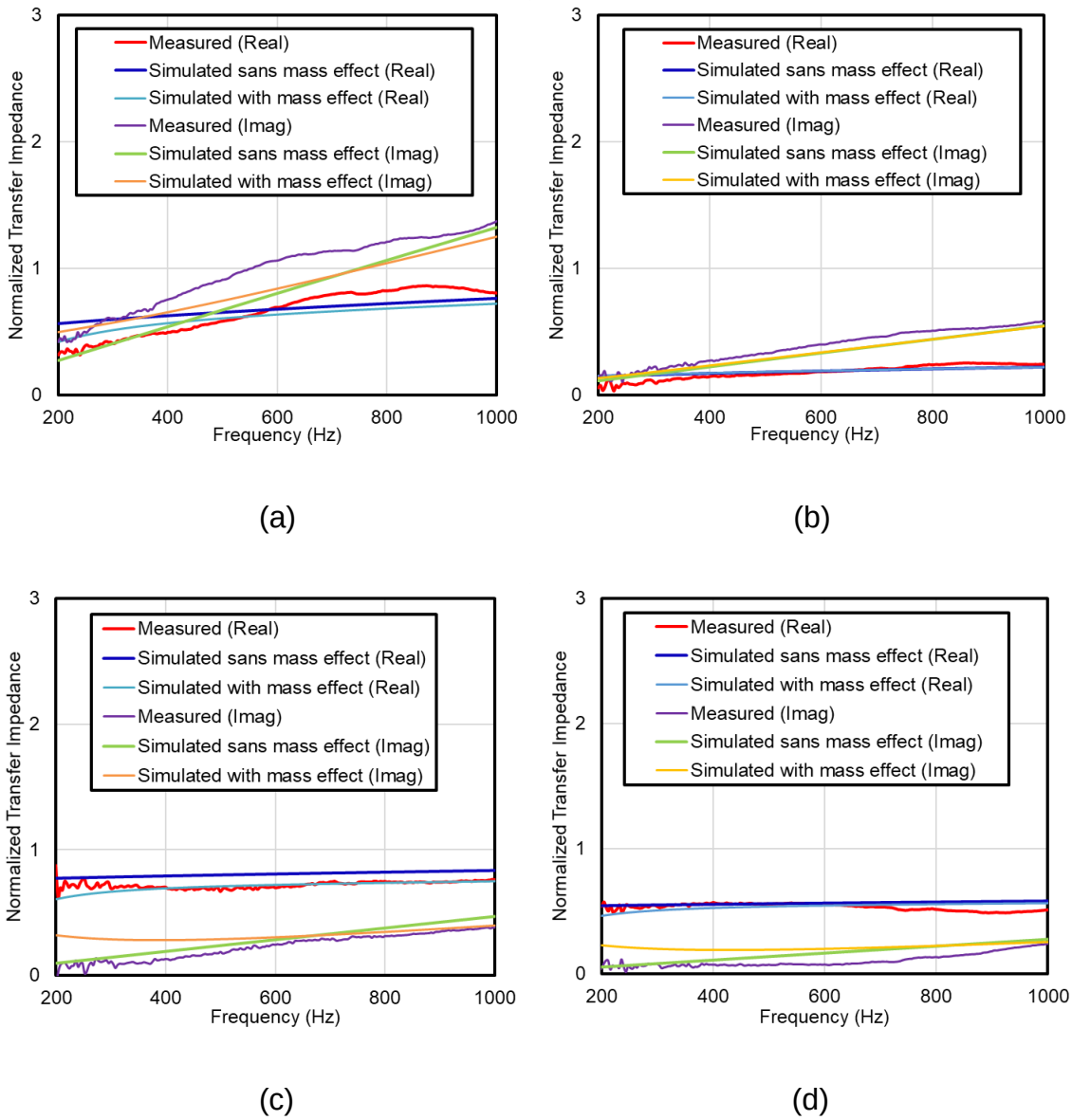

Figure 4.18 Comparison of fitted and direct measurement of the real and imaginary parts of transfer impedance, (a) Fabric A, (b) Fabric B, (c) Fabric C, (d) Fabric D.

4.6 Uses of the Effective Parameters

Once the effective parameters are determined, they can be used to predict the sound absorption 1) at different cavity depths and 2) to expand the frequency range from the measured sound absorption data. Both uses were illustrated in the prior section. In addition, the effective parameters can be used to determine the sound absorption of multi-layered absorbers as well as the transmission loss of single or multiple layer fabric treatments.

The sound absorption of double layer fabrics with a 2.5 cm air gap and 7.5 cm cavity depth was predicted using the determined effective parameters. Predictions are compared to direct measurement in Figure 4.19 (a) for Fabrics A and C and Figure 4.19 (b) for Fabrics B and C placed in tandem with each other. Observe that predictions compare well with direct measurement. The effective parameters were measured with the 98.4 mm diameter impedance tube.

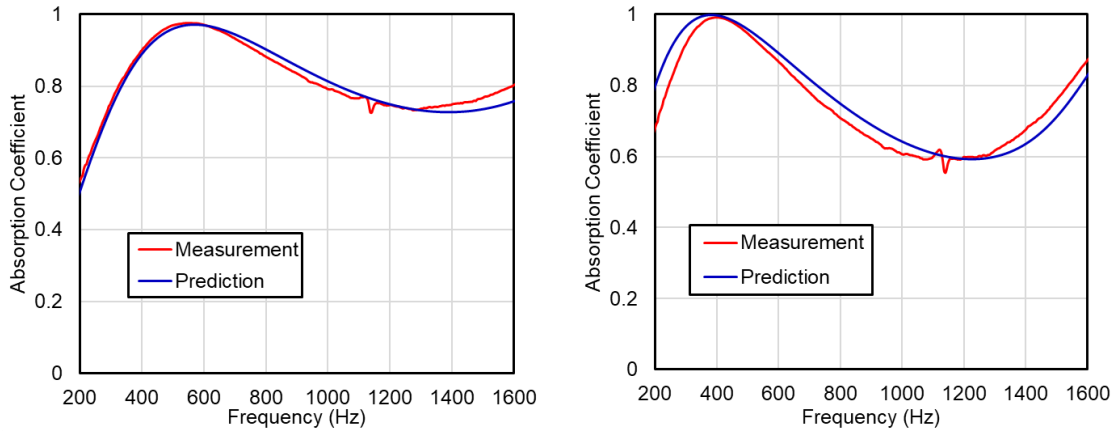

(a) (b)

Figure 4.19 Comparison of predicted and direct measurement of the sound absorption for double layers, (a) Fabric A and C, (b) Fabric B and C.

The effective parameters are then used to determine the transmission loss for a single layer (Fabric C) and double layer (Fabrics A and C). Observe that the transmission loss is relatively low (below 5 dB at most frequencies). There are discrepancies in the results at the very low frequencies, which is likely a consequence of the transmission loss being low. However, bear in mind that the plotted range is only 10 dB and that predictions are within 1 dB of direct measurement above 400 Hz. This is acceptable agreement for engineering purpose.

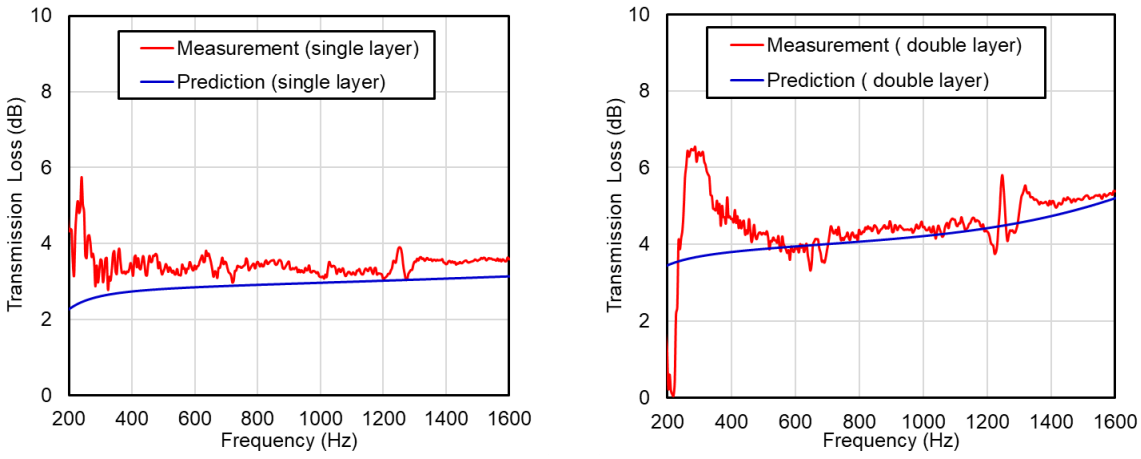

(a) (b)

Figure 4.20 Comparison of predicted and direct measurement of transmission loss, (a) Fabric C, (b) Fabric A and C.

4.7 Application of Acoustic Fabrics in an Enclosure

To complete the investigation, acoustic fabrics were used to improve the performance of an enclosure. The fabrics absorber treatments were placed on one side of a sealed enclosure. The dimensions of the enclosure are $0.75 \times 0.60 \times 0.60$ m^3. The fabric was spread across a 0.40×0.40 m^2 portal with a backing cavity

depth of 50 mm. A loudspeaker was placed on one side of the enclosure. The sound pressure level was determined at 6 microphone positions on a plane 12.7 cm away from the fabric, as indicated in Figure 4.21. The sound pressure level measurements were averaged, and an insertion loss was defined as the difference in the sound pressure level without treatment compared to with treatment. Figure 4.22 compares the insertion loss of a single layer fabric (Fabric D). Observe that the acoustic fabric treatment is effective at frequencies above 500 Hz.

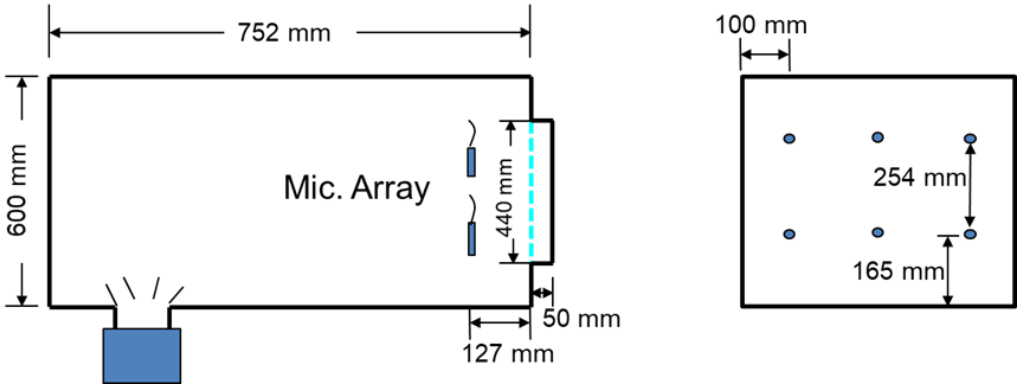

Figure 4.21 Schematic of enclosures setup.

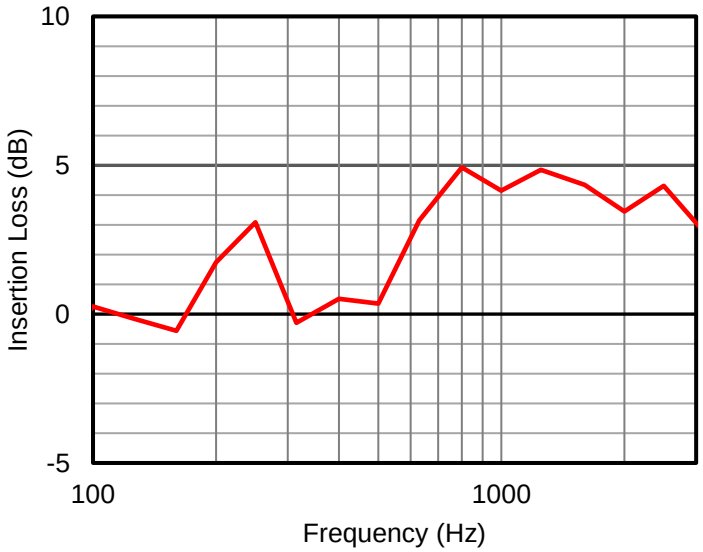

Figure 4.22 Insertion loss due to acoustic fabric installed in sealed enclosure.

The same enclosure was then used for similar case where the wall behind the fabric was removed. Insertion loss is defined as the difference of sound power level without treatment and with treatment. Three cases were considered including a 1) single layer fabric, 2) double layer of fabric with 50 mm separation, and 3) 0.5 inch foam. The sound power through the opening was measured using a sound intensity scan.

Insertion loss results are compared in Figure 4.23 for the single layer and double layer fabric. Note that both the single and double layer fabric treatments are effective above 200 Hz. The attenuation for the double layer fabric is approximately 5 dB over a broad range of frequencies.

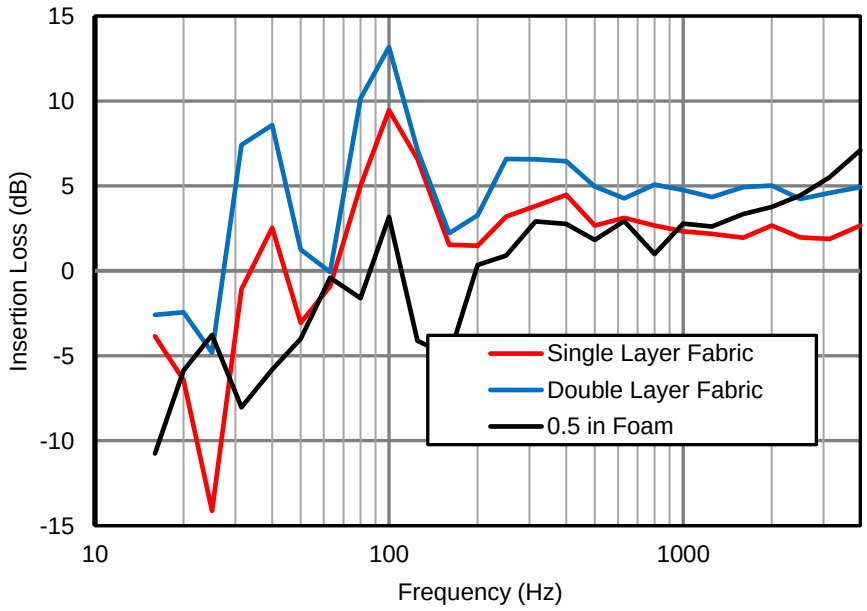

Figure 4.23 Comparison of insertion loss of single layer fabrics, double layer fabrics and 0.5 inch foam.

These attenuation results are encouraging and suggest that acoustic fabrics could be used in some enclosure applications so long as they meet the fire requirements.

4.8 Summary

The sound absorption coefficient and transmission loss of different sound absorbing fabrics are measured and it is shown that the fabric may be modeled using the well-known equations for microperforated panels. Normal incident sound absorption can be measured with a given depth, and then an effective hole diameter and perforation rate can be determined via a least squares curve fit. A sensitivity study is performed, and it can be concluded that determination of effective parameters via curve fit is especially advantageous if perforation diameter, perforation rate, or thickness is small. The results of the sensitivity study are also relevant to many current commercial microperforated sound absorbers. The study suggests that fabric mass should be included in the calculations. Moreover, it is demonstrated that it is more correct to include both the real and imaginary parts of the fabric transfer impedance which has not always been included in prior research. Once the effective parameters are obtained, they can then be used to predict the sound absorptive performance for different cavity depths as well as the transmission loss through a single layer and two layers of fabric. Fabric is also installed in a partial enclosure and the effectiveness of the sound absorptive fabric is demonstrated.

Chapter 5 3D PRINTED SOUND ABSORBERS

5.1 Introduction

Fibers and foams are primarily used in industrial applications due to their effectiveness and low cost. The primary mechanism for attenuation is viscous friction except at very low frequencies where damping effects are dominant. As a rule, fibers and foams are effective at medium to high frequencies but performance is limited at very low frequencies unless thickness is increased. Commercial absorbers often incorporate multiple layers or covers (i.e., mylar or foil). Doing so increases price, but durability is improved, and performance is enhanced in targeted frequency bands.

Though traditional absorbers are suitable for many applications, alternative sound absorbers are gaining more traction. These include microperforated panel (MPP) absorbers (Maa, 1975; Herrin et al., 2011, 2017) and acoustic metamaterials (Li et al., 2018; Yang et al., 2010; Ma et al., 2014). MPP absorbers, which dissipate noise because of viscous resistance in the small perforations, are currently used in many industrial applications including vehicle interiors and engine compartments (Herrin et al., 2011). Acoustic metamaterials, on the other hand, are a topic of current research interest and commercial application is minimal. Most extant metamaterials have been comprised of either multiple acoustic (Li et al., 2018) or mechanical resonators (Yang et al., 2010; Ma et al., 2014; Leblanc et al., 2017). Li et al. (2018), for example, cascaded Helmholtz resonators of varying volume, and Yang et al. (2010) embedded masses in membranes.

3D printing has been used to develop both MPP absorbers and acoustic metamaterials but may also be used to develop materials that fall into neither category. Liu et al. (2017) 3D printed MPP absorbers and Lepak et al. (2018) printed arrays of small reeds that functioned as a collection of small cross-sectional area quarter wave tubes. Leblanc and Lavie (2017) printed membrane absorbers with an aim to maximize low frequency panel transmission loss at targeted frequencies. Though not tailored for sound absorptive purposes, it is likely that the membranes developed or similar structures could be used as sound absorbers.

In perhaps the most interesting application, Jonza et al. (2017) developed a broadband sound absorbing panel with interconnected honeycomb cells. By selectively removing partitions between cells, cavities of varying length were creatively tuned to specific frequencies. The absorber had the additional virtues of being lightweight and thin. The material was first fabricated using 3D printing but is now being manufactured using more traditional means.

Most of the ideas noted are not new. In especially prescient research from over 40 years ago, Wirt (1975) proposed a) banks of reeds or reactive absorbers of varying length, b) suggested placement of resistive layers in front of the reed collection, c) added Helmholtz resonators behind the reeds, and d) even considered horn shaped banks of reactive absorbers. Many of Wirt's ideas still wait to be implemented.

The current work shows some early attempts at the University of Kentucky to develop sound absorbers using 3D printing. The ideas are intended to explore the large design space of sound absorbers that may be 3D printed. The primary

qualifications of the sound absorbers considered is that they are a) difficult to fabricate by other means, b) display features that are suited to 3D printed materials, and c) may be measured in a standard impedance tube.

5.2 Methodology

All sound absorbers were printed using a Gigabot 3+ XL 3D printer using polylactic acid (PLA). Printing times were on the order of 6 hours per sample. The infill percentage was 90%. After the sample was printed, the sound absorption was measured in a 9.9 cm diameter impedance tube using the ASTM E1050 (1998) standard. 3D printed parts are faceted and small leaks around a sample are unavoidable. Leaks will affect the sound absorption of the sample and so an effort was made to seal all leaks using plumber's putty. This was especially necessary around the periphery of the sample.

Acoustic finite element models were developed for several configurations and solved using MSC Actran (2016). The geometry was created using PTC Creo (2020) and then meshed using Altair HyperMesh (2017). The acoustic domain was meshed using linear tetrahedral elements. The maximum frequency considered is 2000 Hz which roughly corresponds to the impedance tube cutoff. The element size selected corresponded to 10 elements per acoustic wavelength. A small amount of sound absorption was added to the air by specifying the speed of sound to be complex. The speed of sound was specified as $343 \pm 6j$ m/s.

5.3 Helmholtz Resonator Type Absorbers

Several Helmholtz resonator absorbers were designed, prototyped, and tested. The resonance frequency for a Helmholtz resonator is well known (Bies et al., 2018) and can be expressed as

$$\omega_0 = c\sqrt{\frac{S}{l_e V}} \tag{5.1}$$

where c is the speed of sound (343 m/s for air), S and l_e are the cross-sectional area and effective length of the connecting neck, and V is the volume of the cavity. A larger neck cross-sectional area (S) insures that the resonator will be more robust attenuating sound over a wider frequency band, and it is, thus, preferable to increase the effective length (l_e) or cavity volume (V) to lower the resonance frequency.

The first sample considered, identified as Rapid Prototyped Helmholtz Resonator 1 (RPHR1), is a simple case that could be easily manufactured by other means. The sample is shown in Figure 5.1 and the accompanying drawing of the absorber is shown in Figure 5.2. The photograph in Figure 5.1 shows the inside of the sound absorber with a panel removed. As Figure 5.2 shows, there are similar panels in front of and behind the sample so that the sample can be oriented in either direction. The panels are 0.25 cm thick. There are two cylindrical partitions (0.25 cm thick) behind the panel that serve to divide up the backing cavity into 3 separate volumes and provide structural support for the front panel. The cavity volumes are indicated in Figure 5.2 by different colors and are 31 cm^3 (green), 105 cm^3 (orange), and 217 cm^3 (blue) respectively. Referring to both Figure 5.1 and

Figure 5.2, three 0.51 cm diameter openings in the panel communicate to the respective volumes behind. Hence, the absorber can be thought of as 3 separate Helmholtz resonators in parallel. For measurements, the sample is sealed around the periphery of the front panel and care was taken seal the back of the sample to avoid communication between volumes.

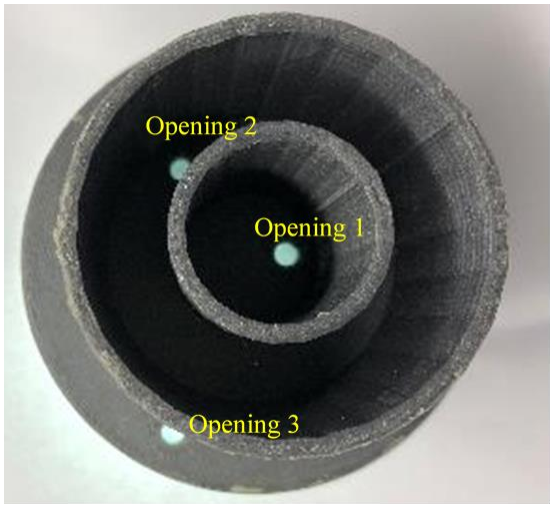

Figure 5.1 3D printed RPHR1.

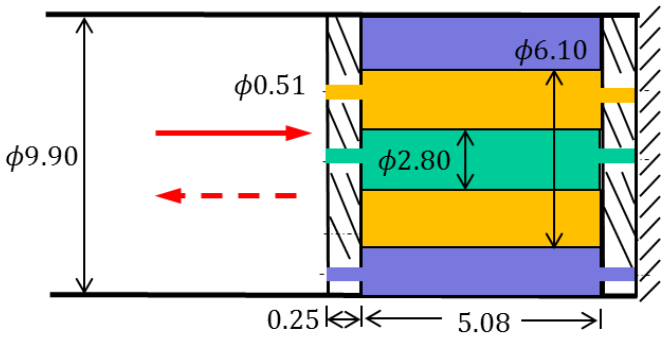

Figure 5.2 Schematic of RPHR1. (unit cm)

The measured and FEM simulated sound absorption of the sample is plotted versus frequency in Figure 5.3. As anticipated, there are three frequency bands of high sound absorption which correspond to the Helmholtz frequencies at

185 Hz, 270 Hz and 510 Hz. The partitions act as stiffeners for the front panel so no strong panel resonances are evident.

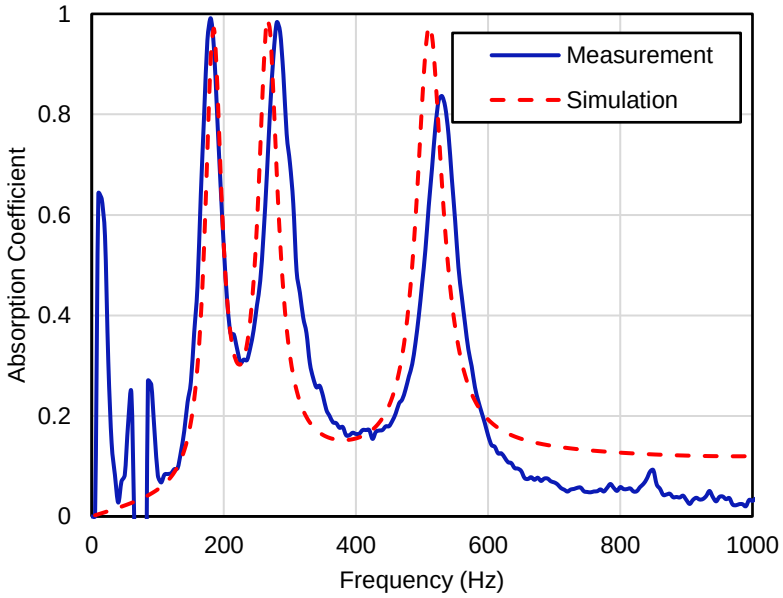

Figure 5.3 Comparison of measured and simulated absorption coefficient of RPHR1.

RPHR2, shown in Figure 5.4, is a similar configuration. The front panel is identical to that used in RPHR1, but the two cylindrical partitions are removed. A cylindrical cylinder was also printed which conforms to the outer diameter of the impedance tube. Figure 5.5 shows a dimensioned drawing of the absorber.

The sound absorption is plotted versus frequency in Figure 5.6. The frequency of highest sound absorption is 260 Hz. Interestingly, note the presence of a second resonance at approximately 750 Hz and that this resonance remains even if all holes are blocked. This resonance is due to the first panel mode. The panel resonance frequency (ω_p) can be estimated using the expression

$$\omega_0 = \left(\frac{C_1}{r}\right)^2 \sqrt{\frac{D}{m_s}} \tag{5.2}$$

where $C_1 = 3.196$, r is the radius of the panel, m_s is the surface mass density (in kg/m^2), and D is the bending rigidity (Nilsson et al., 2015). Bending rigidity is $D = Eh^3/12(1-\nu^2)$ where E is the elastic modulus ranging from 2.0 GPa to 3.5 GPa for PLA, h is the panel thickness and ν is the Poisson's ratio. Using Equation (5.2) the panel resonance is estimated to be between 560 and 750 Hz. The air stiffness behind the panel is not included and would increase the predicted resonant frequency.

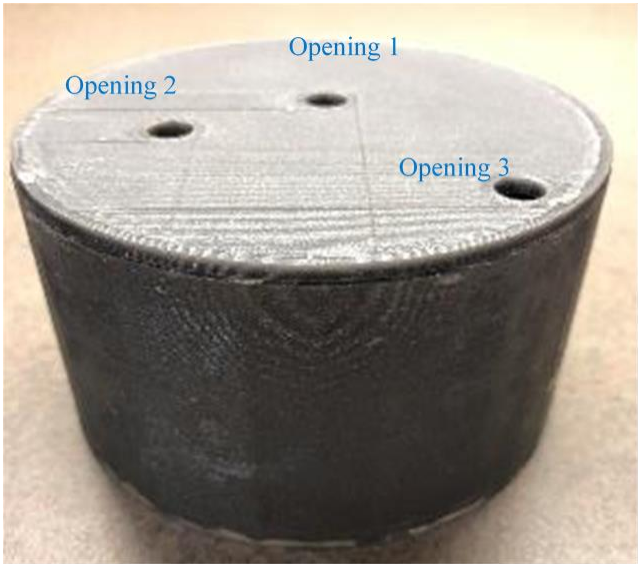

Figure 5.4 3D printed RPHR2.

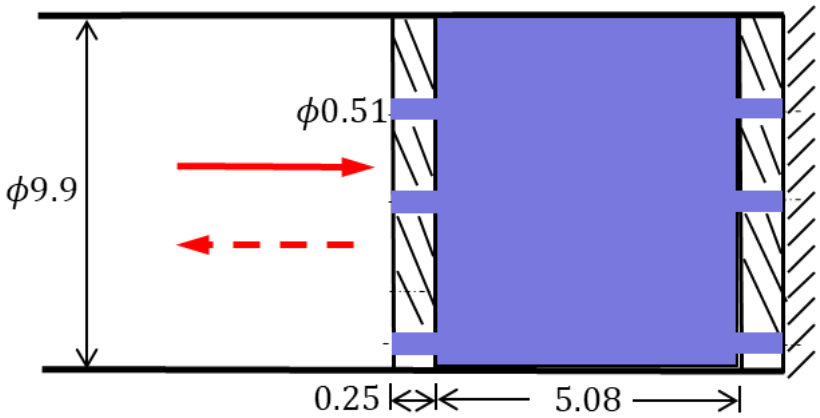

Figure 5.5 Schematic of RPHR2. (unit cm)

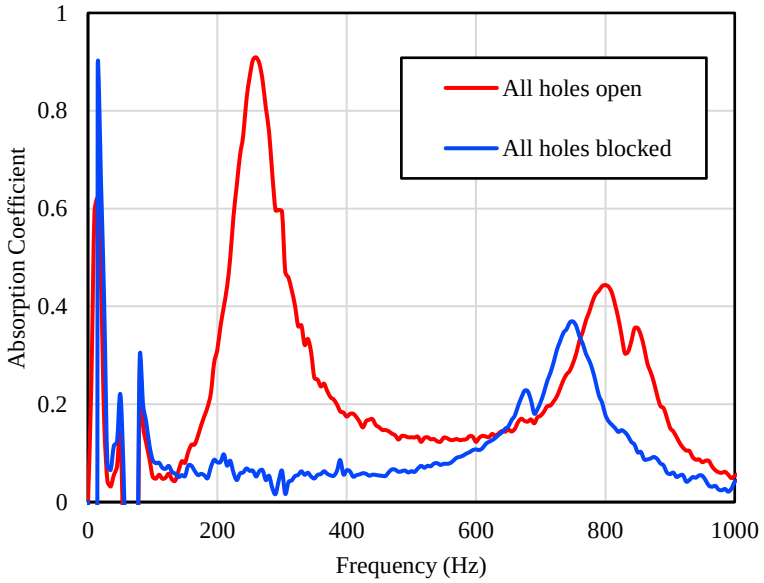

Figure 5.6 Absorption coefficient of RPHR2.

RPHR3, shown in Figure 5.7, utilizes 4 spiral wound necks which extend from the front surface of the sound absorber to a ledge 0.76 cm from the rear of the absorber. The four necks open into a hollowed-out volume in the center of the sound absorber. Figure 5.8 shows two other views of the absorber and Figure 5.9 shows a drawing of just one of the extended necks. The neck is approximately 12.2 cm long and has a cross sectional area of 1.9 cm^2. The volume of the

Helmholtz resonator is 190.7 cm^3. The intent of this configuration is to both a) maximize the neck length of the Helmholtz resonator which will lower the resonant frequency and b) maximize the neck area which should improve the effectiveness of the sound absorber.

Figure 5.7 3D printed RPHR3.

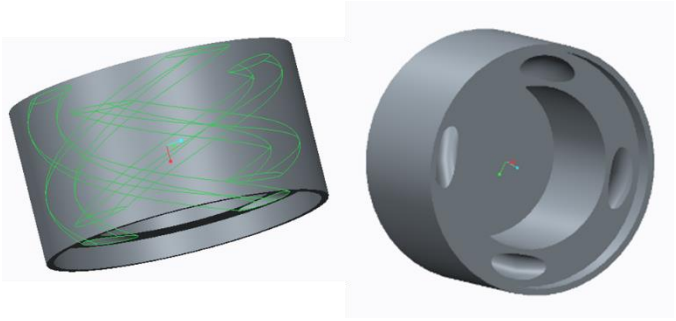

Figure 5.8 Two views of the RPHR3 CAD geometry.

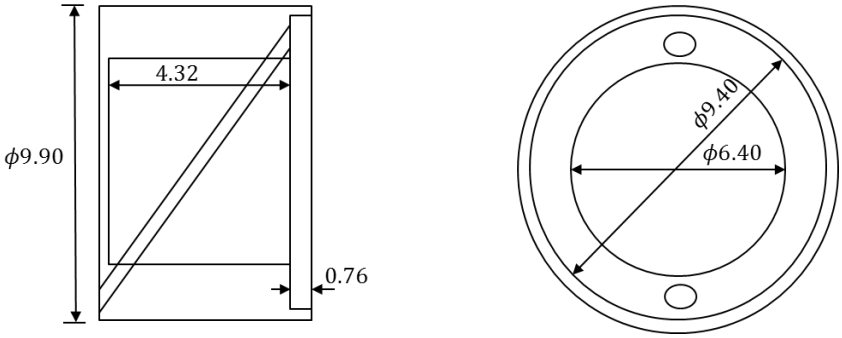

Figure 5.9 Left side and front views of one neck. (unit cm)

This configuration would be difficult to manufacture by a means other than 3D printing. The sound absorption is shown in Figure 5.10 and the Helmholtz frequency is at 180 Hz. Measurement and finite element simulation predict this resonance. In addition, a second resonance can be seen at approximately 1500 Hz. At this frequency, the length of the neck is approximately 1/2 acoustic wavelength.

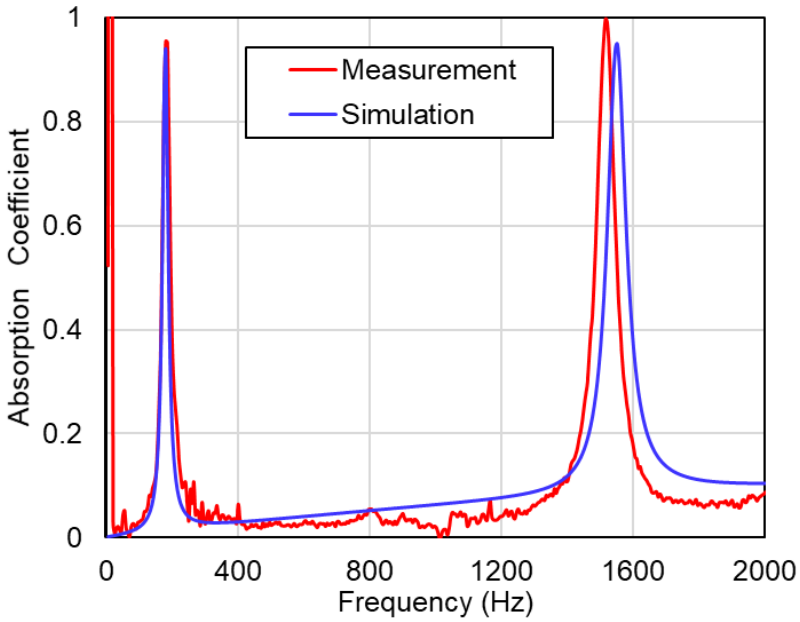

Figure 5.10 Comparison of measured and simulated absorption coefficient of RPHR3.

5.4 Resistive and Reactive Sound Absorbers

5.4.1 RPRR1 and RPRR2

The next set of sound absorbers designed and printed capitalized on both resistive and reactive strategies. Rapid Prototyped Resistive Reactive 1 (RPRR1) is pictured in Figure 5.11 with an accompanying drawing in Figure 5.12. A square 4 cm × 4 cm array of square passageways similar to micro-perforations are designed into the panel facing the sound source. The panel is 1 cm thick and is much thicker than most commercial MPP absorbers. Passageways are thus much longer which augments the dissipation. Passageways of both 1 mm × 1 mm and 2 mm × 2 mm were printed. A cylindrical partition is included behind the panel which breaks the backing volume into two parts. The inner volume, behind the aforementioned passageways, is 148 cm^3 and the surrounding volume is 217 cm^3. A single 5 mm diameter circular opening connects to this surrounding volume producing a more traditional Helmholtz resonator.

The sound absorption is shown in Figure 5.13 for both 1 mm × 1 mm and 2 mm × 2 mm passageways. For the 1 mm × 1 mm passageways, there is a peak in the sound absorption at 125 Hz produced by the Helmholtz resonator. In addition, there is a broadband attenuation region centered at roughly 620 Hz. If the passageway cross-sectional dimension is increased to 2 mm × 2 mm, the broadband frequency region of high sound absorption is centered at approximately 850 Hz. These attenuation bands correspond to Helmholtz resonance frequencies, but the frequency band is broadened due to the friction in the relatively long perforations. This effect is similar to what is seen in MPP absorbers.

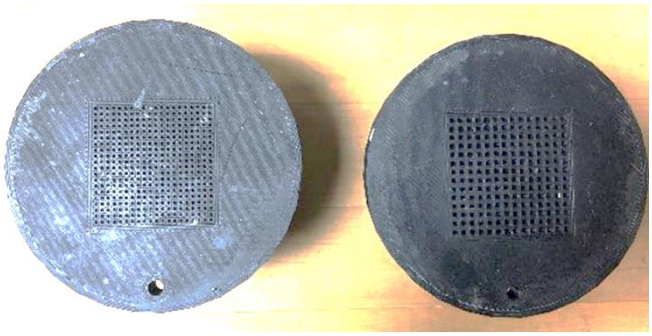

Figure 5.11 3D printed RPRR1.

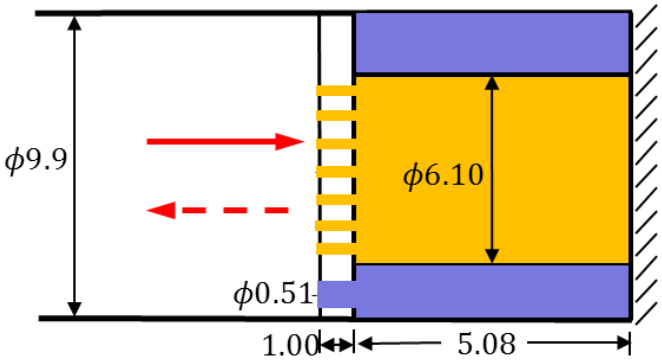

Figure 5.12 Schematic of RPRR1. (unit cm)

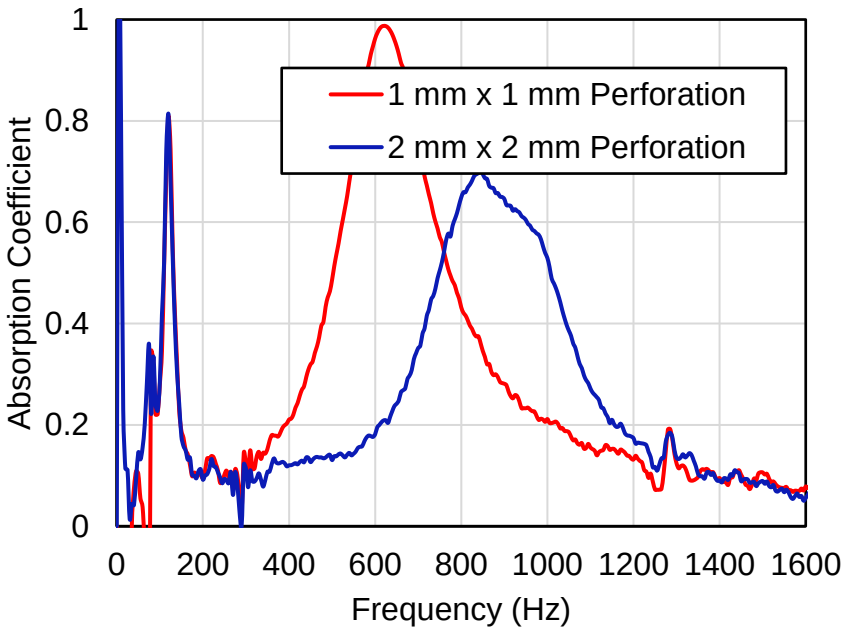

Figure 5.13 Absorption coefficient of RPRR1.

The absorber was also simulated using the MSC Actran (2016) software. Figure 5.14 compares the simulation to direct measurement for RPRR1 and the agreement is satisfactory throughout the frequency range.

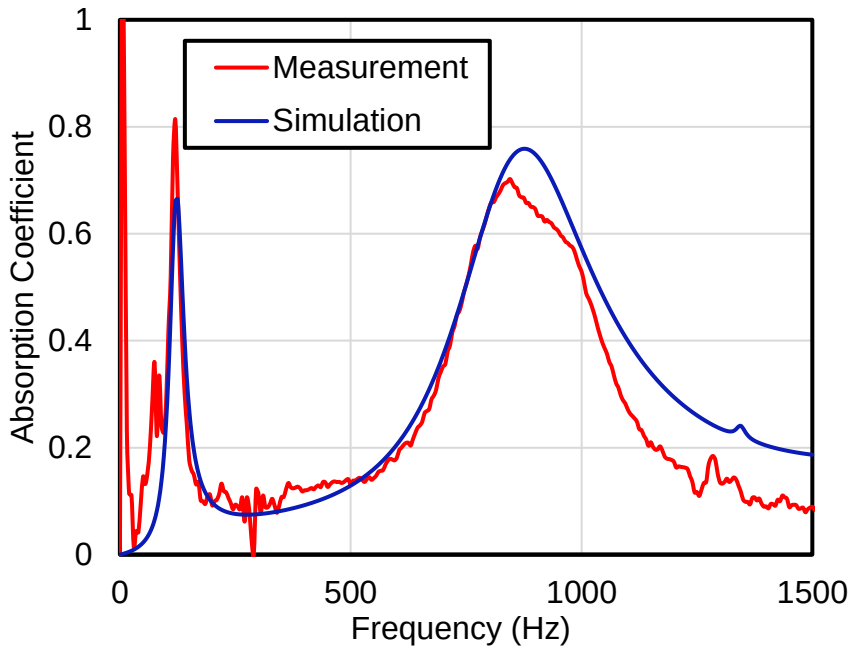

Figure 5.14 Comparison of measured and simulated absorption coefficient of RPRR1.

RPRR2 further explores the potential for varying the lengths of the passageways and is pictured in Figure 5.15. The passageway array is 6 cm × 6 cm and is divided up into four equal sections; each section having different passageway lengths. These four sections 1, 2, 3, and 4 are indicated in Figure 5.15 (b) and correspond to passageway lengths of 0.25 cm, 1.3 cm, 2.5 cm and 3.8 cm respectively. Passageways are 2 mm × 2 mm in cross-section and the distance between passageways is 3 mm. Passageways open into a cavity of volume 236 cm^3.

(a) (b)

Figure 5.15 3D printed RPRR2. (a) front view, (b) back view.

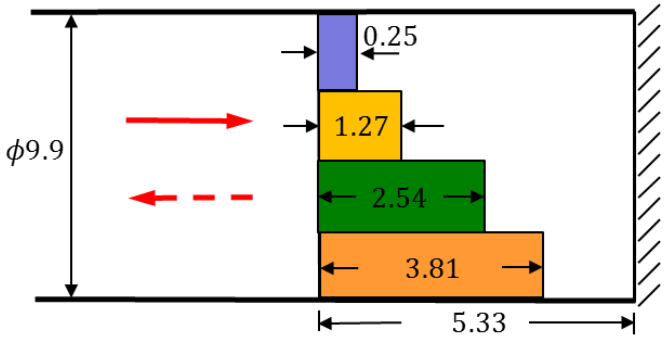

Figure 5.16 Schematic of RPRR2. (unit cm).

The RPRR2 can be tuned by blocking sets of passageways. Figure 5.17 compares the measured sound absorption with all sections open, Sections 1 and 2 closed, and Sections 3 and 4 closed. Putty was used to close the sections. Longer length passageways are more effective at lower frequencies. Hence, blocking Sections 1 and 2 produces a wide band of good sound absorption centered at 500 Hz whereas the absorbing band is centered at 715 Hz if sections 3 and 4 are blocked. It is anticipated that similar strategies can be used to produce the wideband sound absorption at low frequencies that is often desired.

The RPRR2 was also simulated using the FEM software MSC Actran. For the simulation, no channels were blocked. Measurement and simulation are

compared with each other in Figure 5.18. Agreement is good except at the very low frequencies where measurements are likely to be inaccurate due to insufficient source power.

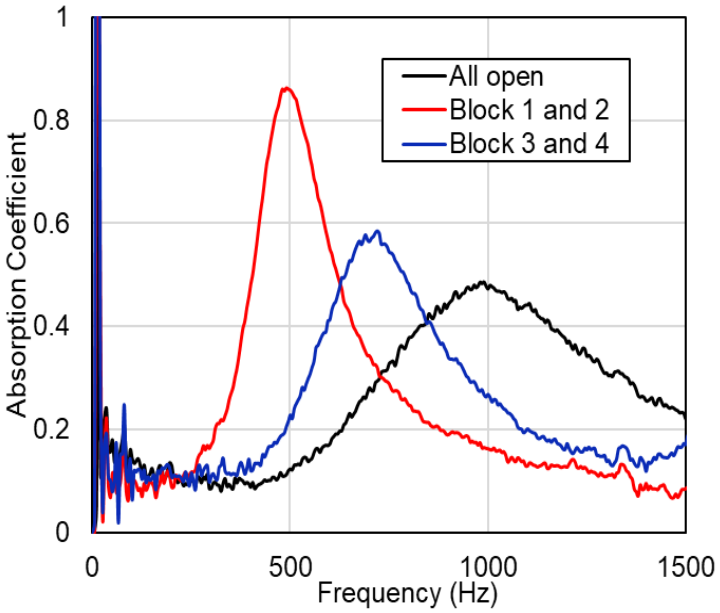

Figure 5.17 Absorption coefficient of RPRR2.

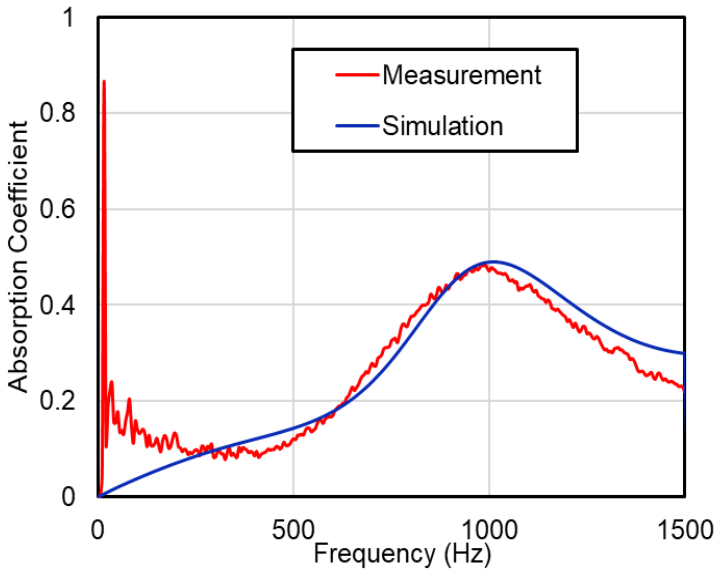

Figure 5.18 Comparison of measured and simulated absorption coefficient of RPRR2.

5.4.2 Channels and Helmholtz Resonators

The second set of sound absorbers designed and printed capitalized on both channels and horn strategies. The Rapid Prototype Channels and Horn (RPChHrn) configuration is pictured in Figure 5.19 with an accompanying drawing in Figure 5.20. A circular array of square passageways similar to micro-perforations are designed into the panel facing the sound source. The panel is 1.5 cm thick and is much thicker than most commercial MPP absorbers and is also thicker than design RPRR1. Passageways are thus much longer which augments the dissipation. Passageways are 2 mm X 2 mm in cross-sectional area. The center part of the panel facing the sound source is the inlet of the horn. A cylindrical partition is included behind the panel which breaks the backing volume into two parts. The inner volume, behind the aforementioned passageways is 171 cm^3 and the surrounding volume is 214 cm^3. A single 1.5 cm diameter circular opening connects to the center volume.

(a)

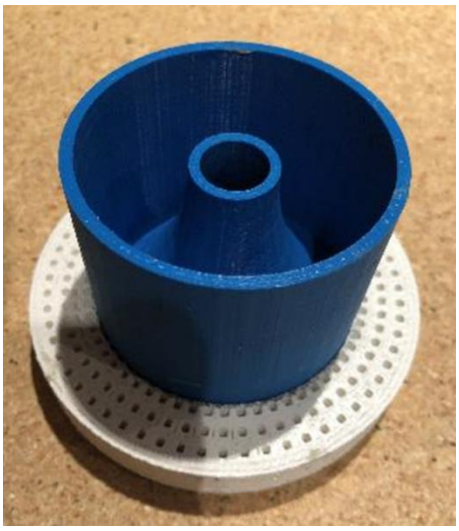

(b)

(c)

Figure 5.19 3D printed RPChHrn. (a) front view, (b) back view, (c) side view.

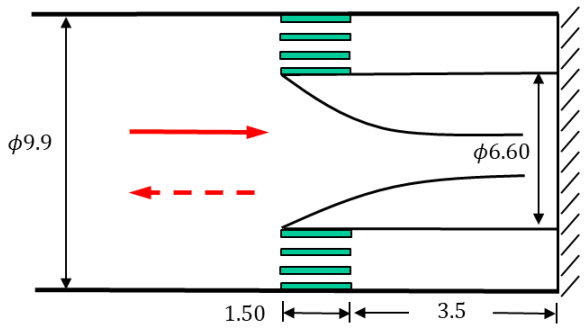

Figure 5.20 Schematic of RPChHrn. (unit cm)

The sound absorption is shown in Figure 5.24 for 2 mm × 2 mm passageways. There is a peak in the sound absorption at 415 Hz produced by the horn. In addition, there is a broadband attenuation region centered at roughly 940 Hz. Similar to designs RPRR1 and RPRR2. The frequency band is broadened due to the friction in the relatively long perforations. If the perforation panel is shifted to the left or right from the original location, the broadband frequency region of high sound absorption will change accordingly.

In this research, the perforated section on the periphery is shifted to three locations with backing cavity depths of 2 cm, 3.5 cm and 4.5 cm as shown in Figure 5.21. The absorber was also simulated using a plane wave approach. The absorber was broken up into elements as shown in Figure 5.22. RPChHrn was also simulated using MSC Actran as discussed earlier. The Actran FEM model is shown in Figure 5.23.

The measured sound absorption is shown in Figure 5.24 for the three different perforated section placements. The low frequency resonance at approximately 400 Hz is due to the cone and does not change as a result of the perforated section placement. The higher frequency resonances are broadband

and depend on the cavity depth behind the perforated section. Observe that the resonance shifts to lower frequencies as the cavity depth increases.

In addition, plane wave and FEM simulation results are compared for RPChHrn Configuration A. Notice that the agreement is excellent for the low frequency resonance but there are deviations at higher frequencies. This is likely due to a gap (or gaps) between the sample and the impedance tube. From Equation (5.1), observe that the resonance frequency will shift to higher frequencies if the neck cross-sectional area increases.

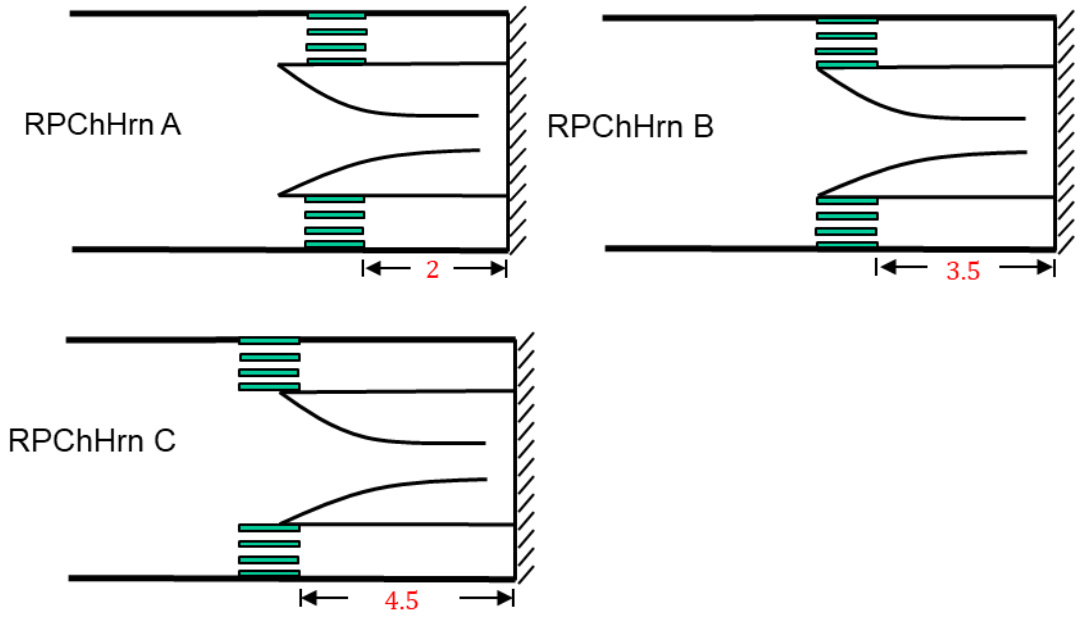

Figure 5.21 Schematic of RPChHrn A, B and C. (unit cm)

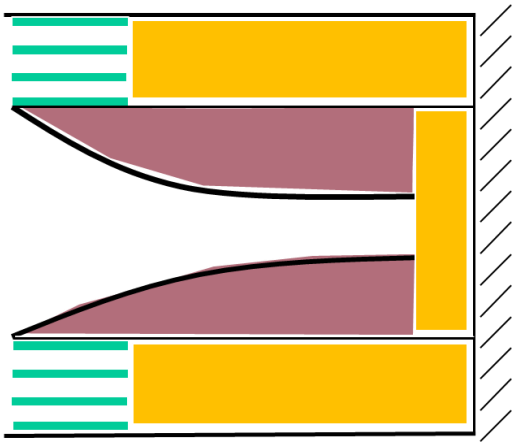

Figure 5.22 Plane wave model of RPChHrn.

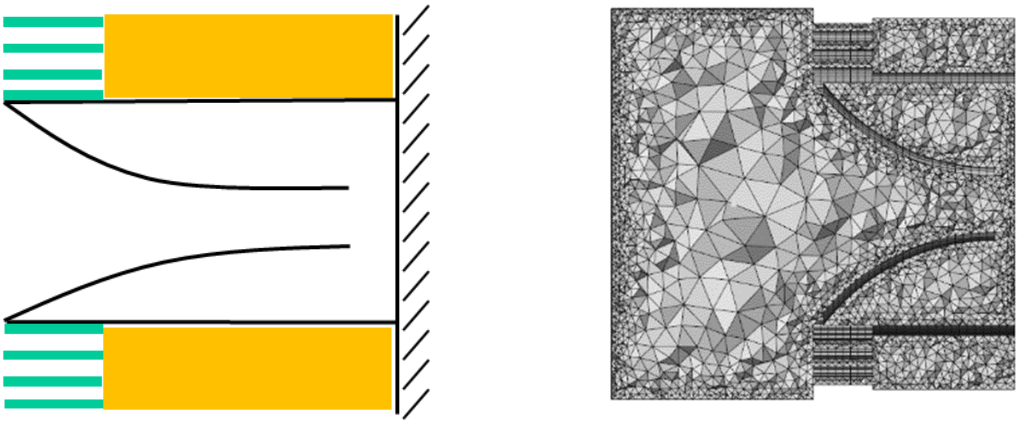

Figure 5.23 Actran model of RPChHrn.

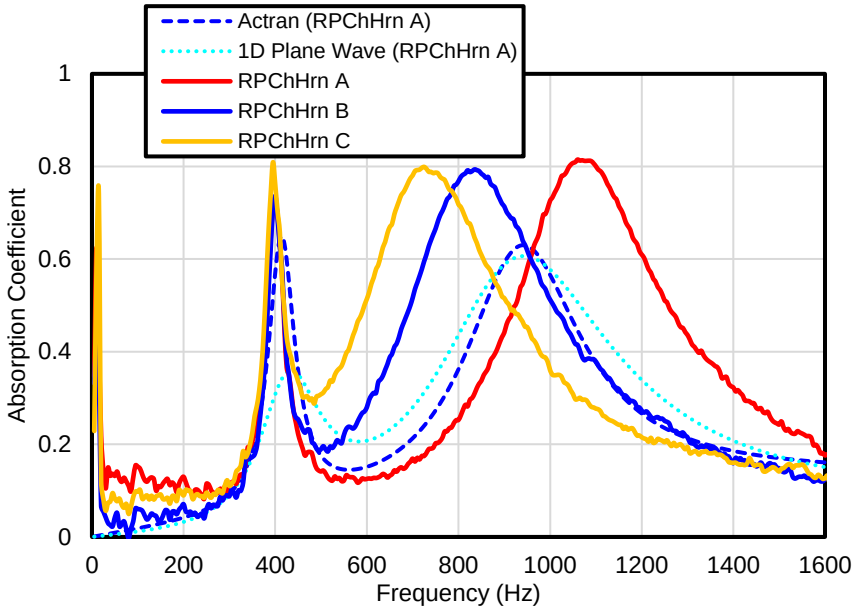

Figure 5.24 Sound absorption coefficient of RPChHrn.

Another variation of these ideas is shown in Figure 5.25 (a) with the accompanying diagram in Figure 5.25 (b). There are two sets of channels. The channels are all square in cross-section. The channels on the periphery are 3 cm in length and the inner set of channels are 1 cm in length. The backing cavity depth 2 cm in length for the channels on the periphery. The backing cavity depth for the inner channels is variable.

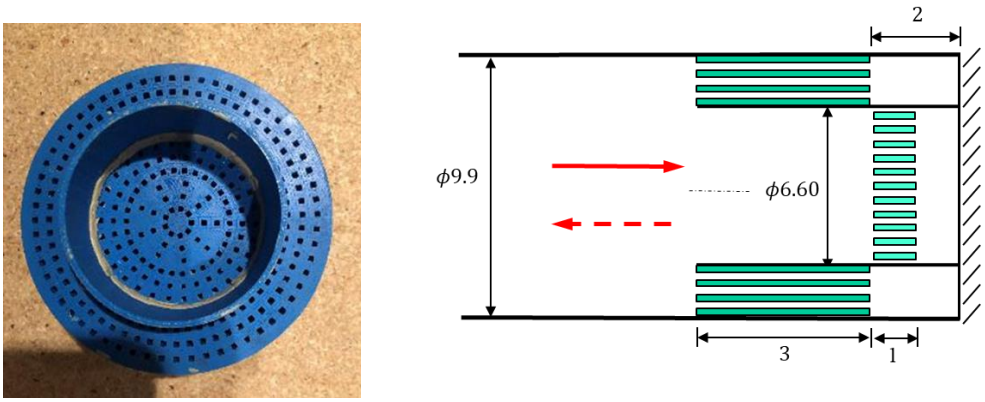

(a) (b)

Figure 5.25 (a) 3D printed RPChX2, (b) Schematic of RPChX2. (unit cm)

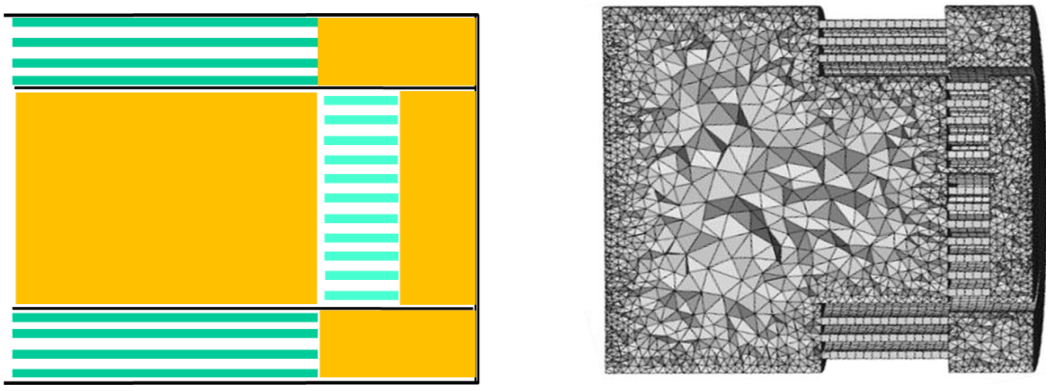

Figure 5.26 Plane wave model and finite element analysis model of RPChX2.

Two configurations are shown in Figure 5.27 with 1 cm and 2 cm backing cavity depths. The RPChX2 Configuration A was also simulated using both plane wave and MSC Actran simulation. Sound absorption results are shown in Figure 5.28. The first resonance at approximately 850 Hz is governed by the peripheral channels and is at approximately the same frequency for both Configurations A and B. The backing cavity depth for the inner circular panel determines the second resonance frequency. Observe that the resonance frequency is at approximately

1200 Hz for Configuration A and 100 Hz for Configuration B. Notice also that simulation results compare favorably with measurement for Configuration A.

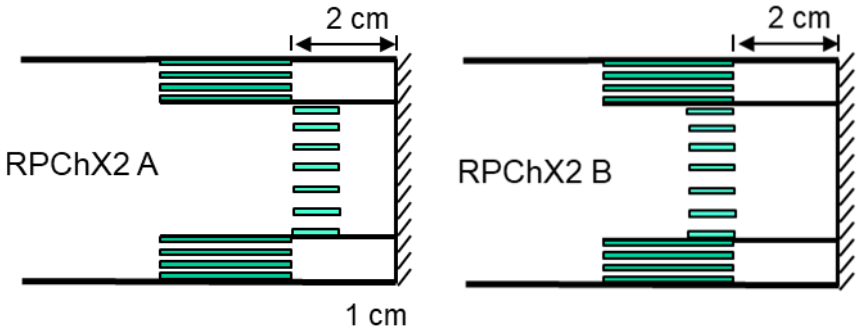

Figure 5.27 Schematic of RPChX2 A and B. (unit cm)

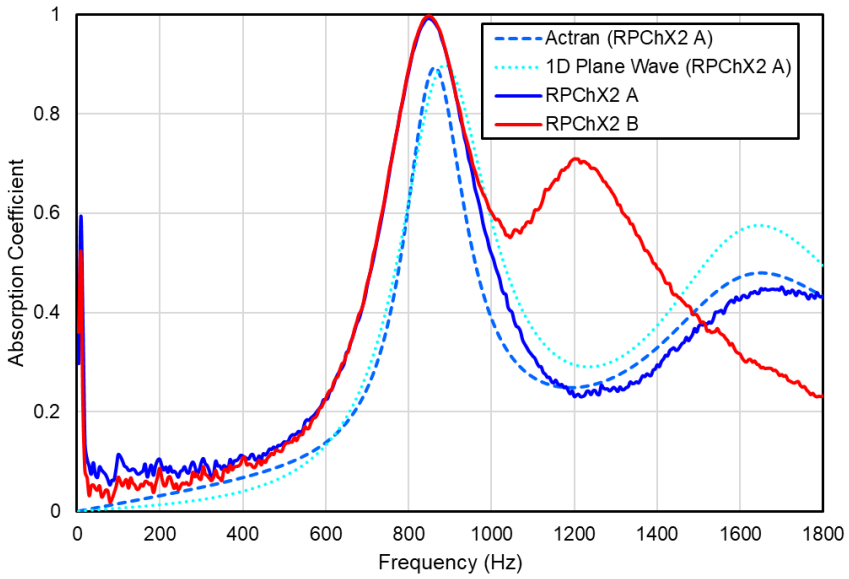

Figure 5.28 Sound absorption coefficient of RPChX2 A and B.

A third configuration, RPChX2 Configuration C is considered where the peripheral perforations are shifted to the left increasing the backing cavity depth from 2 cm to 3.5 cm. Figure 5.29 is a schematic comparing Configurations A and C. Measured sound absorption results are shown Figure 5.30. Notice that increasing the cavity depth lowers the frequency of the first resonance.

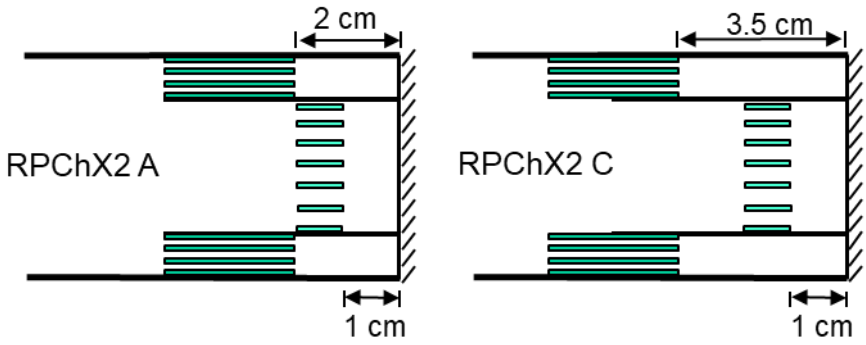

Figure 5.29 Schematic of RPChX2 A and C. (unit cm)

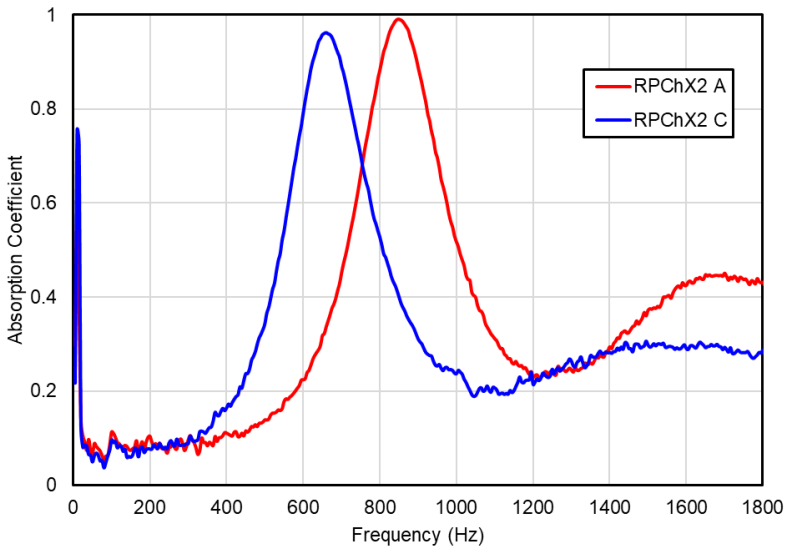

Figure 5.30 Sound absorption coefficient of RPChX2 A and C.

5.5 Summary

The objective of this research was to explore the design space of sound absorbers that may be 3D printed. An effort was made to consider several designs that would be difficult to produce by another means. Several sound absorbers were designed, 3D printed, and tested. Helmholtz resonator designs were examined including a case with a spiral wound neck where neck length is maximized which

correspondingly shifts the resonance to lower frequencies. Other absorbers developed were both resistive and reactive and demonstrated the potential to develop broadband sound absorbers with outstanding low frequency performance.

Chapter 6 CONCLUSIONS AND FUTURE WORK

The overall objective of this research was to investigate novel absorbers that can function as alternatives to traditional absorbers like fibers and foams. While inexpensive, fibers and foams are undesirable in many applications due to durability and potential safety concerns. The alternative absorbers considered include microperforated panel absorbers, thin acoustic fabrics, and additive manufactured absorbers. The documented work in this thesis is exploratory.

6.1 Micro-perforated Panel Sound Absorbers

The primary advantages of microperforated panel (MPP) absorbers are that they are fiber free, durable, easy to clean, and easily tuned for different frequencies. They function by converting sound energy to heat due to high acoustic particle velocity in the sub-millimeter size perforations. By spacing the MPP absorber strategically from a solid backing, the sound absorption can be tuned to a desired frequency band.

The sound absorption of an MPP absorber was enhanced by dividing up the backing cavity using partitioning schemes. The primary objectives of the partitioning were to improve attenuation at low frequencies and over a wider frequency range. Partitioning schemes included a) varying the channel depth by wrapping one channel around another, b) adding Helmholtz resonators behind the MPP, c) tapered channels, and d) using a double leaf MPP. Each configuration was modeled using plane wave simulation. Samples were developed and tested in an impedance tube. Most importantly, the diffuse field sound absorption was

also investigated using a small-scale reverberation room. The results demonstrated that the sound absorption was improved at the lower frequencies and that broadband frequency attenuation was achieved.

MPP sound absorbers appear to be promising in areas where fiberglass and foam cannot be used, such as health facilities or high temperature applications. The discussed special backing cavity designs shaped the sound absorption coefficient over the frequency range while minimizing the space occupied. With this advantage, MPP sound absorbers are promising in many applications such as office locations and hospital heating, ventilation, and air conditioning systems.

6.2 Acoustical Fabrics

Recently, there has been interest in woven fabrics especially for architectural applications. Fabrics are easy to install and can be any color. They are also deployable and can be easily stowed if not in use. For acoustic purposes, fabrics need to have high acoustic resistance which corresponds to high flow resistance. The sound absorptive mechanism is dissipative and hence high acoustic particle velocity in the fabric is desirable to maximize effectiveness. Hence, these absorbers function in a manner identical to MPP absorbers and can be modeled in similar ways.

In this study, the sound absorption coefficient and transmission loss of different sound absorbing fabrics are measured and it is shown that the fabric may be modeled using the well-known equations for MPP absorbers. It is shown that the normal incident sound absorption can be measured with a given depth, and then an effective perforation diameter and porosity can be determined via a least

squares curve fit. The effective parameters can then be used to predict the sound absorptive performance for different cavity depths as well as the transmission loss through a single layer or multiple layers of fabric.

As part of this work, a sensitivity analysis was performed to better understand how the sound absorption is modified due to changes or variations in hole diameter, perforation rate, thickness, and fabric mass. The results of this sensitivity analysis are pertinent to both fabrics and MPP absorbers. It was found that the sound absorption is especially dependent on the hole diameter and perforation rate. Thickness and mass were less important unless panels were correspondingly very thin or very lightweight.

6.3 3D Printed Sound Absorbers

Additive manufacturing is slowly changing how components are developed and manufactured. As the technology develops over time, it is anticipated that industry will 3D print sound absorbers in production. Configurations may be considered that would be difficult to manufacture in another way. For exploratory purposes, several designs were 3D printed and positioned in an impedance tube for testing. Though the absorbers developed are based on well-established strategies, the absorbers considered are either difficult to manufacture by another means or take advantage of the unique features of 3D printed parts.

The samples measured include long channels, lightweight panels, and Helmholtz resonators with spiral wound necks. These are all ideas that resemble those used for enhancing MPP absorption considered earlier in this thesis. Long channels perform similarly to perforations. By lengthening the channels, the cross-

sectional dimensions of the channel can be larger but there is still sufficient friction to attenuate sound due to the extended surface area. One advantage of additive manufacturing is that the absorber is light weight. A thin panel placed in front of void in the material produces a coupled structural acoustic mode where the thin panel behaves similar to a mass and the panel and air in the void combine to form a spring. These modes can be tuned to improve low frequency acoustic performance. Helmholtz resonators function in a similar manner. A channel is connected to a larger cavity. The air in the channel functions as a mass and the air in the cavity acts as a spring. Though Helmholtz resonators are easily manufactured using standard manufacturing techniques, the lower frequency range can be extended via additive manufacturing by printing a spiral wound neck that could not be manufactured by conventional means. Each of these concepts were investigated using both analysis and measurement and the performance was improved.

References

Actran 15.0 User's Guide, Actran VI, MSC Software Company (2014).

Actran 17.0 User's Guide, Actran VI, MSC Software Company (2016).

Alexandru Pirjan and Dana-Mihaela, The impact of 3D printing technology on the society and economy, Journal of information systems & operations management. Vol. 7 No. 2, 360-370, December 2013.

Allam, S. and Åbom, M. A New Type of Muffler Based on Microperforated Tubes, ASME Journal of Vibration and Acoustics, Vol. 133, 2013.

Allam, S., Guo, Y., and Åbom, M., "Acoustical Study of Micro-Perforated Plates for Vehicle Applications", SAE Noise and Vibration Conference, Paper No. 2009-01-2037, St. Charles, IL, (2009).

Allard, JF, Atalla, N. Propagation of sound in porous media: modelling sound absorbing materials. Chichester: Wiley; 2009.

Altair Hypermesh, https://altairhyperworks.com/product/HyperMesh (2017).

Aso K and Kinoshita R. Absorption of sound wave by fabrics, Part 3: Flow resistance. Textile Machinery Society of Japan 1964; 10(5): 236–241.

ASTM C384-04, Standard test method for impedance and absorption of acoustical materials by impedance tube method, 2016.

ASTM C423, Standard test method for sound absorption and sound absorption coefficients by the reverberation room method, (2009).

ASTM C522-09, Standard Test Method for Airflow Resistance of Acoustical Materials, American Society for Testing and Materials, 2009.

ASTM E2611-09, Standard test method for measurement of normal incidence sound transmission of acoustical materials based on transfer matrix method, (2009).

ASTM E1050-98, Standard test method for impedance and absorption of acoustical materials using a tube, two microphones and a digital frequency analysis system. (1998).

Atalla N, Sgard F., "Modeling of perforated plates and screens using rigid frame porous models", J Sound Vib 2007; 303(1–2):195–208.

Bies, D. A., Hansen, C. H., and Howard, C. Q., Engineering Noise Control, 5th edition, CRC Press. (2017).

Boden, H., and Abom, M., (1986). "Influence of Errors on the Two-microphone Method for Measuring Acoustic Properties in Ducts", Journal of the Acoustical Society of America, Vol. 79, pp. 541-549.

Cobo P, Cuesta M, Siguero M. Comparison of models describing double layer microperforated absorbers. Noise Control Eng J 2009; 57(1):10–5.

Cox, T. and D'Antonio, P., Acoustic Absorbers and Diffusers: Theory, Design and Application, 3rd Edition, CRC Press, Boca Raton, FL (2017).

Creo Parametric 2.0, Creo Elements/Direct Drafting User's Guide: Fluent User Interface, PTC Inc., (2020).

Croker, M.J. Handbook of noise and vibration control, John Wiley & Sons, (2007).

Dias, T. and Monaragala, R. (2006). Sound absorption in knitted structures for interior noise reduction in automobiles. Measurement Science &Technology, 17, 2499–2505. doi:10.1088/0957-0233/17/9/018.

Dias, T., Monaragala, R., Needham, P., & Lay, E. Analysis of sound absorption of tuck spacer fabrics to reduce automotive noise. Measurement Science & Technology, 18, 2657–2666. doi:10.1088/0957-0233/18/8/042, (2007a).

Dias, T., Monaragala, R., & Lay, E. Analysis of thick spacer fabrics to reduce automobile interior noise. Measurement Science & Technology, 18, 1979–1991. doi:10.1088/0957-0233/18/7/026, (2007b).

Herrin, D. W., Hua, X., and Liu,J., "Microperforated Panel Design: A Tutorial", 21st International Congress on Sound and Vibration, Beijing, China, July 13-17 (2014).

Herrin, D. W., Liu, J., and Seybert, A. F. , "Properties and Applications of Microperforated Panels," Sound and Vibration, Vol. 45, No. 7, pp. 6-9 (July 2011).

Herrin, D. W., Liu, W., Hua, X., and Liu, J., "A Guide to the Application of Microperforated Panel Absorbers," Sound and Vibration, Vol. 51, No. 12, pp. 12-20 (December 2017).

Herrin, D.W., Tao, Z., Carter, A.E., Liu, J., Seybert, A. F., "Using numerical methods to analyze multicomponent HVAC systems." ASHRAE Transactions, vol. 113, no. 1, 2007.

Horoshenkov KV, Khan A, Bécot FX, Jaouen L, Sgard F, Renault A, Amirouche N, Pompoli F, Prodi N, Bonfiglio P, Pispola G, Asdrubali F, Hübelt J, Atalla N, Amédin CK, Lauriks W, Boeckx L, J. Acoust. Soc. Am., 122, 345-353, 2007.

Hua, X., Herrin, D. W., and Jackson, P., Enhancing the Performance of Microperforated Panel Absorbers by Designing Custom Backings, SAE International Journal of Passenger Cars - Mechanical Systems, 2013; Vol. 6, No. 2.

Hua, X., Herrin, D. W., and Jackson, P., Varying Backing Cavity Depths to Achieve Broadband Absorption using Micro-Perforated Panels, Noise-Con, Denver, CO, 2013.

Huang, W., Schwan, L., Romero-Garcia, V., Genevaux, J.-M. & Groby, J. -P., 3D-printed sound absorbing metafluid inspired by cereal straws, Nature, (2019) 9:8496, https://doi.org/10.1038/s41598-019-44891-z 1.

ISO 10534-2, Acoustics-Determination of sound absorption coefficient and impedance in impedance tubes - Part 2: Transfer-function method, 1998.

Jackson, P., Design and Construction of a Small Reverberation Chamber, SAE Technical Paper 2003-01-1679.

Jeong, C.H., Chang, J.H., Reproducibility of the random incidence absorption coefficient Converted from the Sabine absorption Coefficient, Acta Acust., 101, 99-112, 2015.

Laly Zacharie, Atalla Noureddine, Meslioui Sid-Ali, Bikri El Khalid, Sensitivity analysis of micro-perforated panel absorber models at high sound pressure levels, Applied Acoustics, 156 (2019) 7-20.

Leblanc, A. and Lavie, A., Three-Dimensional-Printed Membrane-Type Acoustic Metamaterial for Low Frequency and Sound Attenuation. J. Acoust. Soc. Am. 141 (6), EL538 (2017).

Lepak, W. B., Sterner, M. S. and Slaboch, P. E., Acoustic Performance of Additively Manufactured Reeds as an Absorber, Inter-Noise 2018, Chicago (2018).

Lercher Peter, Environmental noise and health: An integrated research perspective. Environment International, Vol. 22, No. 1, pp. 117-129, 1996.

Li, Chenxi, Cazzolato, Ben., and Zander, Anthony., "Acoustic impedance of micro perforated membranes: velocity continuity condition at the perforation boundary", J. Acoust. Soc. Am. 139(1), 2016.

Li, J., Shen, C., Diaz-Rubio, A., Tretyakov, A. S. and Cummer, S. A., Systematic Design and Experimental Demonstration of Bianisotropic Metasurfaces for Scattering-Free Manipulation of Acoustic Wavefronts, Nature Communications, 9:1342 (2018).

Liu, J. and Herrin, D. W., "Enhancing Micro-Perforated Panel Attenuation by Partitioning the Adjoining Cavity," Applied Acoustics, Vol. 71, pp. 120-127 (2010).

Liu, J., Hua, X., and Herrin, D. W., "Estimation of Effective Parameters for Microperforated Panel Absorbers and Applications", Applied Acoustics, 75, pp. 86-93 (2014).

Liu, W., Herrin, D. W., "Determination of effective parameters of acoustic fabrics including applications", Internoise 2018.

Liu, W. and Herrin, D., "Early Research on Additively Manufactured Sound Absorbers", SAE Technical Paper, doi:10.4271/2019-01-1576, 2019.

Liu, W., Herrin, D. W., Bianchini, E., "Diffuse Field Sound Absorption of Microperforated Panels with Special Backings", SAE International, doi:10.4271/2017-01-1876, 2017.

Liu, Z., Zhan, J., Fard, M., and Davy, J., Acoustic Measurement of a 3D Printed Micro-Perforated Panel Combined with a Porous Material. Applied Acoustics, 121, pp. 25–32 (2017).

Jonza, J. M., Herdtle, T., Kalish, J., Gerdes, R., and Yoo, T., Acoustically Absorbing Lightweight Thermoplastic Honeycomb panels, Int. J. Veh. Dyn., Stab., and NVH, Volume 1, Issue 2 (2017).

Kang J and Funchs HV. “Predicting the absorption of open weave texiles and mocre-perforated membranes backed by an air space”, J Sound Vib, 220:905-920 (1999).

Keefe, D. H., Acoustic Wave Propagation in Cylindrical Ducts: Transmission Line Parameter Approximations for Isothermal and Nonisothermal Boundary Conditions, Journal of the Acoustical Society of America, Vol. 75, No. 1, pp. 58-62 (1984).

Ma, G., Yang, M., Xiao, S., Yang, Z., and Sheng, P., “Acoustic metasurface with hybrid resonances,” Nat. Mater. 13, 873–878 (2014).

Maa, D. Y., Theory and design of microperforated-panel sound-absorbing construction, Scientia Sinica XVIII, 1975; pp. 55-71.

Maa, D. Y., Potential of microperforated panel absorber [J]. J. Acoust. Soc. Am. 104 (5): 2861-2866 (1998).

Maa, D. Y., “Theory of Micro Slit Absorbers,” Acta Acustica, 2000-06.

Malcolm J. Crocker, (2007). Handbook of noise and vibration control, John Wiley and Sons, INC.

Mechel F.P., Mertens P.M. and Schilz W.A., “Research on sound propagation in sound absorbent ducts with superimposed air streams”, AMRLTR-65-53, (1965).

Mechel F.P. Schallabsorber – band III: Anwendungen. Stuttgart: S. Hirzel, 1998.

Mechel F.P., Ver IL, Sound absorbing materials and sound absorbers. New York: Noise and Vibration Control Engineering, John Wiley & Sons, (1992).

Mohanty, A. R., Fatima, S., Noise Control Using Green Materials, Sound and Vibration, 49 (2), pp. 13-15, (2015).

Munjal, M.L., Acoustics of Ducts and Mufflers, 2nd Edition, John Wiley & Sons, Ltd., West Sussex, United Kingdom, 2014.

Na YJ, Lancaster J, Casali J and Cho G. Sound absorption coefficients of micro-fiber fabrics by reverberation room method. Textile Res J 2007; 77(5): 330–335.

Nilsson, A. and Liu, B., Vibro-Acoustics, Volume 1, 2nd edition, Science Press, Beijing and Springer-Verlag Berlin Heidelberg, (2015).

OSHA, 2020, https://www.osha.gov/SLTC/noisehearingconservation/.

Park, S-H, Acoustic properties of micro-perforated panel absorbers backed by Helmholtz resonators for the improvement of low-frequency sound absorption, Journal of Sound and Vibration 2013, Vol. 332, pp. 4895–4911.

Pieren, R., “Sound absorption modeling of thin woven fabrics backed by an air cavity”, Textile Research Journal, 82(9) 864–874 (2012).

Pieren, R., and Heutschi, K., “Predicting sound absorption coefficients of lightweight multilayer curtains using the equivalent circuit method”, Applied Acoustics, 92, 27-41 (2015).

Robert J. Bernhard, Henry R. Hall, and James D. Jones. Adaptive-passive noise control. Proceeding of Inter-Noise 92, pages 427-430, 1992.

Ruiz, H., Cobo, P., Dupont, T., Martin, B., and Leclaire, P., "Acoustic properties of plates with unevenly distributed macroperforations backed by woven meshes", Journal of the Acoustical Society of America, 132(5), 3138-3147 (2012).

Sakagami, K., Morimoto, M. and Koike, W., A numerical study of double-leaf microperforated panel Absorbers, Applied Acoustics, 2006; Vol. 67, pp. 609-619.

Sakagami, K., Yairi, M. and Morimoto, M., Multiple-leaf sound absorbers with microperforated panels: an overview, Acoustics Australia, 2010; Vol. 38, No. 2, pp. 76-81.

Sakagami K, Kiyama M, Morimoto M and Takahashi D. "Detailed analysis of the acoustic properties of a permeable membrane", Applied Acoustics 1998; 54; 93-111.

Saltelli, A., Ratto, M., Andres, T., Campolongo, F., Cariboni, J., Gatelli, D., Saisana, M., Tarantola, S., Global Sensitivity Analysis: The primer. John Wiley & Sons; 2008.

Schultz, T., Sheplak, M., Cattafesta, L., "Uncertainty Analysis of the Two microphone Method", Journal of Sound and Vibration, Vol. 304, pp. 91-109. (2007).

Sezgin, E., and Haluk, K., "Investigation of Industrial Tea-Leaf-Fiber Waste Material for its Sound Absorption Properties," Applied Acoustics, 70, 215-220, (2009).

Shoshani, Y. and Rosenhouse G, "Noise absorption by woven fabrics", Applied Acoustics 30(4), pp. 321–333 (1990).

Sobol I. M. Global sensitivity indices for nonlinear mathematical models and their Monte Carlo estimates, Mathematics and Computers in Simulation, 2001; 55(1-3): 271-80.

Soltani P and Zerrebini M. The analysis of acoustical characteristics and sound absorption coefficient of woven fabrics. Text Res J 2012; 82: 875–882.

Soltani P and Zarrebini M. Acoustic performance of woven fabrics in relation to structural parameters and air permeability. J Text Inst 2013; 104: 1011–1016.

Song, B. H. and Bolton, J. S., "A transfer matrix approach for estimating the characteristic impedance and wave number of limp and rigid porous materials," Journal of the Acoustical Society of America, Vol. 107, pp. 1131–1152, (2000).

Stephen A Stansfeld, Mark P Matheson, Noise pollution: Non-auditory effects on health, British Medical Bulletin, Vol. 68, pp. 243-257, 2003.

Tang, Xiaoning, Jeongand Cheol-Ho, Yan Xiong, "Prediction of sound absorption based on specific airflow resistance and air permeability of textiles", J. Acoust. Soc. Am. 144, EL100 (2018).

Tao, Z., Zhang, B., Herrin, D. and Seybert, A., Prediction of sound-absorbing performance of micro-perforated panels using the transfer matrix method, SAE technical paper 2005-01-2282, 2005.

Ver, Istvan L. and Beranek, Leo L., Noise and vibration control engineering principles and applications, second edition, John wiley and sons, INC. (2006).

Wirt, L.S., Sound-Absorptive Materials to Meet Special Requirements, Journal of the Acoustical Society of America, 1975; 57(1), pp. 126-143.

Wu, T. W, Cheng, C. Y. R., and Tao, Z., "Boundary element analysis of packed silencers with protective cloth and embedded thin surfaces", Journal of Sound and Vibration, Vol. 261, No. 1, pp. 1–15 (2003).

Yang, Z., Dai, H. M., Chan, N. H., Ma, G. C. and Sheng, P., Acoustic Metamaterial Panels for Sound Attenuation in the 50-1000 Hz Regime, Appl. Phys. Lett. 96, 041906 (2010).

Yoo, T., The Modeling of Sound Absorption by Flexible Micro-perforated Panels, Doctoral Dissertation, Purdue University, 2008.

Zhang, Z. M. and Gu, X. T., The Theoretical and Application Study On A Double Layer Microperforated Sound Absorption Structure, Journal of Sound and Vibration, Vol. 215, No. 3, pp. 399-405, (1998).

Zou, J., Shen, Y., Yang, J., Qiu, X., A note on the prediction method of reverberation absorption coefficient of double layer micro-perforated membrane. Appl Acoust 2006; 67(2):106–11.

Zulkifli, R. and Nor, M.J.M., "Noise Control Using Coconut Coir Fiber Sound Absorber with Porous Layer Backing and Perforated Panel," American Journal of Applied Sciences, 7, 260-264, (2010).

VITA

Weiyun Liu was born in Shandong, China. She received her Bachelor's Degree of Science in Mechanical Engineering from China University of Petroleum (Huadong), China in 2010.

In August 2011, she enrolled in the Department of Mechanical Engineering, University of Kentucky. She received her Master's Degree in Computational Fluid Dynamics in 2014. Subsequently, she enrolled in the Ph. D program in vibration and acoustics at University of Kentucky. During her study at University of Kentucky, she published 2 journal articles, 1 magazine article and 4 conference proceeding articles. Additionally, she has 1 journal article submitted. In the year of 2018, she received the Hallberg Foundation award from INCE-USA.

Weiyun Liu